

# Reconstruction of the SNO+ Experiment

Jie Hu

A Dissertation  
Presented to the Faculty  
of University of Alberta  
in Candidacy for the Degree  
of Doctor of Philosophy

Recommended for Acceptance  
by the Department of  
Department of Physics

January, 2020

© Copyright 2020 by Jie Hu.

All rights reserved.

# **Abstract**

## **0.1 Abstract**

A neutrino is one of the elementary particles we currently know and is included in the Standard Model (SM). However, some properties of neutrinos can not be described by the SM, which shows clues of the new physics beyond the Standard Model.

SNO+ experiment is planned to explore one of the unknown properties of neutrinos: whether the neutrinos are Majorana particles or Dirac particles.

# Acknowledgements

# Contents

<b>Abstract</b>	<b>iii</b>
0.1 Abstract . . . . .	iii
<b>Acknowledgements</b>	<b>iv</b>
<b>Contents</b>	<b>v</b>
<b>List of Figures</b>	<b>viii</b>
<b>List of Tables</b>	<b>xii</b>
<b>1 Introduction</b>	<b>1</b>
1.1 Studies on Solar Neutrinos: History and Current Status . . . . .	1
<b>2 Neutrino physics</b>	<b>2</b>
2.0.1 Discovery of Neutrino . . . . .	2
2.0.2 Solar Neutrino . . . . .	3
2.0.3 Early Solar Neutrino Experiments . . . . .	4
2.0.4 Atmospheric Neutrino . . . . .	4
2.1 Neutrino Flavor Transformation . . . . .	5
2.1.1 Vacuum Oscillation . . . . .	6
2.1.2 Matter Effect . . . . .	9
2.1.3 Reactor-solar Experiments . . . . .	11

2.2	Solar Neutrinos . . . . .	11
2.3	Majorana Neutrino . . . . .	11
2.3.1	Status of Double Beta Decay Experiments . . . . .	13
<b>3</b>	<b>The SNO+ Experiment</b>	<b>16</b>
3.1	Overview . . . . .	16
3.2	SNO+ Physics Phases . . . . .	17
3.3	Detection Medium . . . . .	19
3.3.1	Cherenkov Radiation . . . . .	19
3.3.2	Scintillation from Organic Scintillator . . . . .	20
3.3.3	Liquid Scintillator for SNO+ . . . . .	23
3.4	Optics . . . . .	25
3.5	Trigger and Readout of the SNO+ Detector . . . . .	25
3.6	Calibration . . . . .	28
3.7	Monte Carlo Simulation and the RAT Software . . . . .	29
<b>4</b>	<b>Event Reconstruction</b>	<b>31</b>
4.1	An Overview for the Reconstruction Algorithms in SNO+ . . . . .	31
4.2	Multi-path Vertex Reconstruction Algorithm for SNO+ . . . . .	31
4.3	MPW Position and Direction Reconstructions . . . . .	34
4.3.1	Vertex Reconstruction . . . . .	34
4.3.2	Direction Reconstruction . . . . .	36
4.4	Effective Group Velocity . . . . .	36
4.4.1	Fitter Pull and Drive Correction . . . . .	38
4.4.2	Multi-path Fitter Structure . . . . .	42
4.5	Vertex and Direction Reconstruction for Water-based Wavelength-shifter . .	45
4.6	Vertex Reconstruction for Partial-fill and Scintillator Phases . . . . .	49
4.7	Energy Reconstruction . . . . .	58
4.8	Machine Learning Algorithm . . . . .	59

4.9	PMT Selectors for the Fitter . . . . .	59
<b>5</b>	<b>SNO+ Water Phase Analysis</b>	<b>62</b>
5.1	Classifiers . . . . .	62
5.2	$^{16}\text{N}$ Calibration Scans in the Water Phase . . . . .	63
<b>6</b>	<b>Towards the SNO+ Future Phases</b>	<b>70</b>
6.1	Partial-fill Phase Analysis . . . . .	70
6.1.1	Sky-shine Classifier . . . . .	70
6.1.2	Different PPO Concentrations during the Filling . . . . .	74
6.1.3	Bi-Po Analysis . . . . .	77
6.1.4	Partial-fill Phase Calibration . . . . .	77
6.1.5	Extract Cherenkov Signals in Partial-fill Phase . . . . .	79
6.2	Relative Light Yield Measurements of the Te-loaded Liquid Scintillators . .	82
6.2.1	Measurement Setup and Data Acquisition . . . . .	82
<b>7</b>	<b>Conclusions</b>	<b>91</b>
<b>A</b>	<b>Details for the MultiPath Fitter</b>	<b>92</b>
A.1	Create a Random Vertex . . . . .	92
A.2	Levenberg-Marquardt (MRQ) Method for Minimization[1] . . . . .	92
<b>References</b>		<b>96</b>

# List of Figures

2.1	Solar neutrino energy spectrum ( $E_\nu$ vs. flux) for the solar model BS05(OP)[?].	4
2.2	Feynman diagrams for $2\nu\beta\beta$ (left) and $0\nu\beta\beta$ (right).	12
3.1	The SNO+ detector labelled with main structures, figure modified from [2].	17
3.2	A Jablonski diagram for the organic scintillator, modified from [3, 4].	21
4.1	Diagrams of position (left) and direction (right) reconstruction in SNO+ water phase.	34
4.2	PMT response time as the timing pdf for vertex reconstruction.	35
4.3	PMT angular distribution as the angular response pdf for direction reconstruction.	35
4.4	Refractive index vs wavelength. These values are based on the measurements from laserball calibration scans in the SNO+ water phase[5].	37
4.5	A cartoon shows effects of tuning the effective group velocity. In this case, the effective group velocity is faster than expected, the fitted position is dragged back along the direction to increase the time of flight.	38
4.6	$^{16}\text{N}$ central run.	39
4.7	A cartoon shows fitter pull effect, modified from Fig. C.2 in [6] and Fig. 2,3,4 in [7].	40
4.8	A diagram illustrates the drive correction.	40
4.9	Drive correction parameter $p_0, p_1$ vs energy.	41

4.10 Radial biases of simulated electron events before and after the drive correction, as a function of energy. . . . .	42
4.11 Position distributions of triggered PMTs (in zenith and azimuth angles) for 5 MeV electrons travelling along $+x$ direction in the pure water (left) and the water plus 0.1 ppm PPO (right). . . . .	46
4.12 The energies of simulated electrons as a function of mean nhits. The values in the 0.1 ppm PPO (solid line with inverted triangle) are compared with the water (dashed line with star). . . . .	46
4.13 The timing pdf for the wbWLS. . . . .	47
4.14 Fit position projected on x axis. The WLS fitter reconstructed $x$ positions of the 5 MeV electron events in the wbWLS (red) are compared to the ones in the water (blue). . . . .	48
4.15 Light path calculation for the MP Partial Fitter. The light path intersects with the neck cylinder surface, the AV sphere as well as the water-scintillator interface. The total length of the path in the scintillator region (scintillator path, $sp$ ), $d_{sp}$ is evaluated by intersection calculations. . . . .	49
4.16 Line-sphere intersections. (a): the light ray intersects the sphere with 2 points; (b): the light ray intersects the sphere with 1 point; (c) and (d): the light ray never passes through the sphere. . . . .	51
4.17 Layouts for the scintillator light paths inside the AV sphere. . . . .	53
4.18 Layouts of the scintillator light paths inside the neck cylinder. . . . .	54
4.19 The timing pdfs used by the MP Partial Fitter. Blue: the timing pdf used by the MP Water Fitter; red: the scintillator timing pdf. . . . .	54
4.20 Distributions of fit position bias projected on x axis ( $x_{fit} - x_{MC}$ ). . . . .	56
4.21 Fit results: $\rho_{fit} = \sqrt{x_{fit}^2 + y_{fit}^2}$ vs. $z_{fit}$ . . . . .	56
4.22 Timing profiles for liquid scintillators in different SNO+ phases. . . . .	58
4.23 Group the PMTs by dividing the PMT sphere with latitudes and longitudes.	61
5.1 $^{16}\text{N}$ main decay scheme, modified from [8]. . . . .	64

5.2	$^{16}\text{N}$ calibration source geometry. Left: a detailed diagram of $^{16}\text{N}$ source geometry, modified from [9, 10]; middle: source geometry implemented in RAT, modified from [11]; right: a picture of the $^{16}\text{N}$ source, taken from [12].	64
5.3	Spatial distributions of $^{16}\text{N}$ first $\gamma$ -rays interaction position projected on x axis, obtained from RAT simulations. The double-peak structure is due to the wall of the stainless steel container of the $^{16}\text{N}$ source. . . . .	65
5.4	Likelihood surface of an $^{16}\text{N}$ event projected on X-Y, Y-Z, X-Z planes. A clear global maxima is reached for the fitted vertex. . . . .	67
5.5	Likelihood surface of an $^{16}\text{N}$ event projected on x, y, z, t axes. . . . .	68
5.6	Derivatives of logLikelihood of an $^{16}\text{N}$ event projected on x, y, z, t axes. The analytical derivatives (blue) are overlaid with numerical derivatives (red). They are well-matched. . . . .	69
6.1	An illustration for the Sky-shine classifier, modified from [13]. . . . .	71
6.2	MC (left) and fitted positions (right) of $^{208}\text{Tl}$ simulations. . . . .	72
6.3	MC positions vs. skyShine values for simulated $^{208}\text{Tl}$ events. . . . .	73
6.4	MC positions after Sky-shine cuts ( $skyShine < 1.7$ and $skyShine < 1.5$ ) for simulated $^{208}\text{Tl}$ events. It shows that most of the events with small $skyShine$ values are located in the neck region while very few events in the FV region can be mis-tagged. . . . .	73
6.5	Fit biases vs. skyShine values for simulated $^{208}\text{Tl}$ events. . . . .	74
6.6	Fit biases vs. skyShine values for simulated $^{208}\text{Tl}$ events. . . . .	75
6.7	Radial resolutions with different skyShine cuts. . . . .	75
6.8	A flow chart for Bi-Po tagging. . . . .	78
6.9	Distributions of $\cos\theta_{PMT}$ after the prompt time cut for various $e^-$ energies simulations. . . . .	79
6.10	PMT hit patterns after the prompt time cut and NHit cut. . . . .	80
6.11	$^{16}\text{N}$ source calibration in external water during the partial-fill phase. . . . .	81

6.12 Test sample (left) and setup (right). Left: The samples were filled into scintillation vials. The dimensions are shown in the picture. Right: two PMTs are aligned to face to the scintillation vial from each side. . . . .	83
6.13 A diagram shows the light yield measurement setup. See the text for details.	84
6.14 A typical waveform triggered by scintillation photons from $^{137}\text{Cs}$ $\gamma$ -rays interaction with LAB-PPO sample. . . . .	87
6.15 Measured LAB-PPO energy spectrum with and without coincidence cut on the ADC channel 0. A threshold for counting is set by comparing the two spectrum. . . . .	87
6.16 2D energy spectrum of the counting measurements of LAB-PPO (a), TeSOP (b), and TeDDA (c) samples, projected the 2D plots into one channel (d). The single photo-electron (p.e.) peak is mainly caused by backgrounds while the multiple p.e. peak is from scintillation photons. . . . .	88

# List of Tables

2.1	. . . . .	3
2.2	Oscillation neutrino experiments. . . . .	8
4.1	A comparison of quantitative estimates for the angular resolution between the SNO heavy water, SNO+ wbWLS and the SNO+ pure water cases. . .	48
4.2	Reconstructed position biases and resolutions for simulated events in partial fill. . . . .	55
4.3	. . . . .	57
5.1	Position resolution parameters for the MP Water Fitter. . . . .	66
6.1	time constants and amplitudes measured by Oxford group [14]. . . . .	76
6.2	Relative light yield measured by [14]. . . . .	76
6.3	Tuned effective group velocities for different PPO concentrations. . . . .	76
6.4	Fit speeds and biases for various PPO concentrations. . . . .	77
6.5	Fit speeds and biases for various PPO concentrations. . . . .	77
6.6	Number of photons calculated by Charge weighted photon number method.	90

# Chapter 1

## Introduction

Neutrinos are one of the elementary particles we currently know and are included in the Standard Model (SM). However, some properties of neutrinos can not be described by the SM, which shows clues of the new physics beyond the SM.

SNO+ is a multi-purpose neutrino experiment

SNO+ experiment is planned to explore one of the unknown properties of neutrinos: whether the neutrinos are Majorana particles or Dirac particles.

In this thesis, a position and time reconstruction algorithm is developed for SNO+ physics phases.

calibration

solar neutrino and backgrounds analysis

the SNO+ water phase and partial scintillator fill phase.

### 1.1 Studies on Solar Neutrinos: History and Current Status

## Chapter 2

# Neutrino physics

### 2.0.1 Discovery of Neutrino

The existence of neutrinos was first put forward by Wolfgang Pauli in the 1930s to solve the contradictions observed in beta decay experiments. It was shown definitively by James Chadwick in 1914 that the electrons emitted in beta decay did not have a discrete set of energies but instead had a continuous spectrum[15]. This means that the energy, momentum and angular momentum (spin) were not conserved between the nucleus and electron. To solve this problem, Wolfgang Pauli introduced a charge-neutral, spin-1/2 and nearly massless new particle. The sum of the energies of the new particle, the nucleus and electron is constant, which solved the problem.

In 1934, Bethe and Peierls suggested direct neutrino detection via a neutrino-induced interaction, called the inverse beta decay (IBD):  $\bar{\nu}_e + p \rightarrow e^+ + n$ . Their calculation showed that the IBD cross section was of the order of  $10^{-44} \text{ cm}^2$ . Such a small cross section indicates that the neutrino is difficult to detect[16].

In 1956, Fred Reines and Clyde Cowan made the first discovery of the neutrino (specifically, it was electron antineutrinos  $\bar{\nu}_e$ ) by using a nuclear reactor as an intense neutrino source with neutrino fluxes on the order of  $10^{12} - 10^{13}$  neutrinos/second/cm<sup>2</sup>. The active volume of their detector was two tanks filled with water in which cadmium chloride ( $\text{CdCl}_2$ ) was dissolved. The water tanks were surrounded by liquid scintillator layers coupled with

photomultiplier tubes (PMT) to detect emitted photons. The incoming antineutrinos interacted with the water via IBD. The produced positrons quickly annihilated with  $e^-$  and gave  $\gamma$  signals while the produced neutrons went through the neutron capture process:  $n + {}^{108}\text{Cd} \rightarrow {}^{109}\text{Cd}^* \rightarrow {}^{109}\text{Cd} + \gamma$  and gave delayed  $\gamma$  signals. A coincidence of these two characteristic signals provided a distinctive signature for the neutrino reaction. They measured the cross-section as  $6.3 \times 10^{-44} \text{ cm}^2$ , which was consistent with Bethe's calculation[17].

### 2.0.2 Solar Neutrino

In the 1930s, Hans Bethe et al. explained the origin of the Sun's energy as a series of nuclear reactions[18].

Based on the available physics and experimental data, the Standard Solar Model (SSM) is a modern accepted theory for the evolution of the Sun. The energy in the Sun is mainly produced by two classes of reactions: the proton-proton (pp) chain and the Carbon-Nitrogen-Oxygen (CNO) cycle. The result of the two reactions is:  $4p + 2e^- \rightarrow {}^4\text{He} + 2\nu_e + Q$ , where the released energy,  $Q$  is 26.73 MeV. The  $\nu_e$  produced in the Sun (the solar neutrinos) can be detected on the Earth[19].

Due to the branching ratios and unterminated chains in the pp chain and CNO cycle, the solar neutrinos come from different reactions, as shown in Table 2.1. The solar neutrinos detected on the Earth are named after the specific fusion process[20]. They have different fluxes and energies, as shown in Fig. 2.1[21].

Table 2.1: Solar neutrinos from reactions in pp chain (a) and CNO cycle (b).

(a) pp chain		(b) CNO cycle	
solar $\nu_e$	reaction	solar $\nu_e$	reaction
pp	$p + p \rightarrow {}^2\text{H} + e^+ + \nu_e$	CNO	${}^{13}\text{N} \rightarrow {}^{13}\text{C} + e^+ + \nu_e$
pep	$p + e^- + p \rightarrow {}^2\text{H} + \nu_e$		${}^{15}\text{O} \rightarrow {}^{15}\text{N} + e^+ + \nu_e$
hep	${}^3\text{He} + p \rightarrow {}^4\text{He} + e^+ + \nu_e$		${}^{17}\text{F} \rightarrow {}^{17}\text{O} + e^+ + \nu_e$
${}^7\text{Be}$	${}^7\text{Be} + e^- \rightarrow {}^7\text{Li} + \nu_e$		
${}^8\text{B}$	${}^8\text{B} \rightarrow {}^8\text{Be}^* + e^+ + \nu_e$		

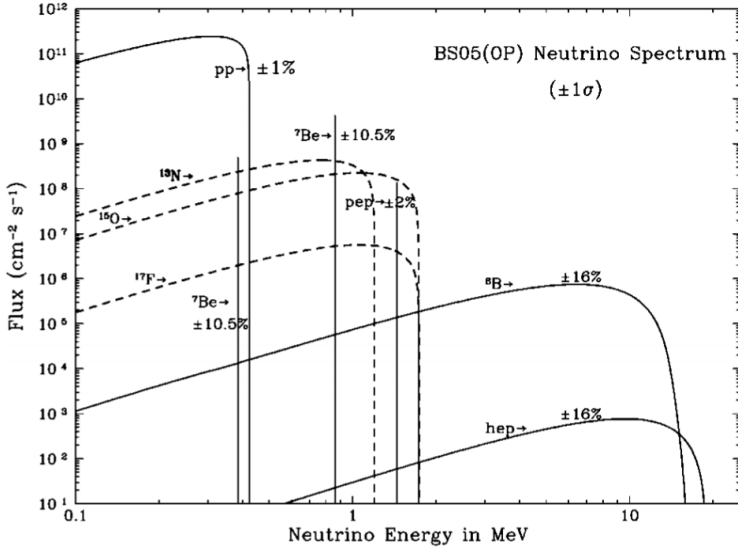


Figure 2.1: Solar neutrino energy spectrum ( $E_\nu$  vs. flux) for the solar model BS05(OP)[?].

### 2.0.3 Early Solar Neutrino Experiments

In 1964, John Bahcall and Raymond Davis proposed the first experiment to detect solar neutrinos[?, ?]. Raymond Davis designed an experiment that used a  $380 \text{ m}^3$  tank filled with Perchloroethylene ( $\text{C}_2\text{Cl}_4$ ), a dry-cleaning fluid rich in chlorine. Solar neutrinos were expected to change  $^{37}\text{Cl}$  to  $^{37}\text{Ar}$  via the endothermic reaction  $\nu_e + ^{37}\text{Cl} \rightarrow ^{37}\text{Ar} + e^-$  and the produced  $^{37}\text{Ar}$  were extracted and counted. The neutrino energy threshold ( $E_{thresh}$ ) of the experiment was 0.814 MeV, which allowed a measurement mostly of the  $^8\text{B}$  neutrino flux but also including some lower energy neutrinos[?]. Their first results, announced in 1968, showed that only about one-third of the predicted radioactive argon atoms were measured. This raised a problem of missing solar neutrinos.

### 2.0.4 Atmospheric Neutrino

Cosmic rays from outer space continuously interact with nuclei in the atmosphere and produce secondary particles. Atmospheric neutrinos come from decay products of the hadrons in the secondaries. The dominant processes of atmospheric  $\nu_e$  and  $\nu_\mu$  production is  $\pi^+ \rightarrow \mu^+ + \nu_\mu$  followed by  $\mu^+ \rightarrow e^+ + \bar{\nu}_\mu + \nu_e$ . In the 1980s, the Kamiokande experiment in

Japan measured atmospheric neutrinos by utilizing a 3-kiloton water-Cherenkov detector. The incoming neutrinos,  $\nu_e$  ( $\nu_\mu$ ) interacted with the water via charged current interactions and electrons (muons) were produced. The electrically charged leptons traversed the water at a speed higher than the speed of light in water and thus emit Cherenkov light, which was recorded by the detector as ring patterns (called Cherenkov rings). The produced electrons caused electro-magnetic showers during their propagation in the water while the produced muons propagated almost in straight lines without producing electro-magnetic showers. Then the  $\nu_\mu$  (the  $\mu$ -like events) were separated from the  $\nu_e$  (the  $e$ -like events) by the fact that the  $\mu$ -like events created sharper Cherenkov rings than the  $e$ -like events. Kamiokande measured the ratio of fluxes  $\Phi(\nu_\mu + \bar{\nu}_\mu)/\Phi(\nu_e + \bar{\nu}_e)$ . The fluxes of atmospheric neutrinos are well understood and the ratio  $\nu_\mu/\nu_e$  is expected to be  $\sim 2$  at low energies  $\leq 1$  GeV. In 1988, they found a deficit of measured  $\mu$ -like events compared to the prediction. This was later confirmed by IMB in 1992[22] and Soudan-2 in 1997[23] and called “atmospheric neutrino anomaly”[24].

## 2.1 Neutrino Flavor Transformation

Neutrino flavor transformation is a quantum mechanical interference phenomenon[25]. It was first discovered in 1998, based on the analysis of atmospheric neutrino fluxes measured by the Super-Kamiokande (SuperK) experiment to solve the “atmospheric neutrino anomaly” mentioned in the last section[26]. It is the first direct evidence showing that neutrinos have finite masses and the Standard Model is incomplete.

Based on current knowledge, neutrinos only interact via the weak force and gravity. A neutrino  $\nu_\alpha$  is generated with a definite flavor from weak interaction and is related to a charged lepton with a given flavor: the electron ( $e$ ), the muon ( $\mu$ ) or the tauon ( $\tau$ ) and thus  $\alpha = e, \mu, \tau$ .

### 2.1.1 Vacuum Oscillation

For neutrino flavor oscillation experiments, neutrinos are detected in certain flavor eigenstates via weak interaction. A neutrino flavor state vector can be taken as a linear superposition of the mass eigenstates. For three-flavor neutrino mixing, we have[27]:

$$|\nu_f\rangle = \sum_{i=1}^3 U_{fi}^* |\nu_i\rangle, \quad (2.1)$$

where  $f = e, \mu, \tau$  and  $k = 1, 2, 3$ . The unitary PMNS matrix,  $U_{PMNS}$ , can be parametrized as:

$$U_{PMNS} = \begin{bmatrix} 1 & 0 & 0 \\ 0 & \cos \theta_{23} & \sin \theta_{23} \\ 0 & -\sin \theta_{23} & \cos \theta_{23} \end{bmatrix} \begin{bmatrix} \cos \theta_{13} & 0 & e^{-i\delta_{CP}} \sin \theta_{13} \\ 0 & 1 & 0 \\ e^{-i\delta_{CP}} \sin \theta_{13} & 0 & \cos \theta_{13} \end{bmatrix} \begin{bmatrix} \cos \theta_{12} & \sin \theta_{12} & 0 \\ -\sin \theta_{12} & \cos \theta_{12} & 0 \\ 0 & 0 & 1 \end{bmatrix}. \quad (2.2)$$

In the PMNS matrix, we have four parameters: the three mixing angles  $\theta_{12}$ ,  $\theta_{13}$ ,  $\theta_{23}$  and the charge-parity (CP) violation parameter of lepton sector,  $\delta_{CP}$ . The unknown value of  $\delta_{CP}$  is related to leptogenesis, the hypothetical physical process that produced an asymmetry between leptons and antileptons in the very early universe[28].

Now discuss the vacuum flavor oscillation: in the lab frame, assume a neutrino is generated at time  $t_0 = 0$  from a source with a certain flavor state  $|\nu_\alpha\rangle$ . It then propagates in vacuum with a speed close to the speed of light (ultra-relativistic) for a distance  $L$  and is finally detected at time  $t$  in a detector. The flavor eigenstate evolves in space-time is  $|\nu_\alpha\rangle = \sum_{i=1}^3 U_{\alpha i}^* |\nu_i, p_i\rangle$ , where  $p_i$  is the 4-momentum of  $\nu_i$ . The momentum is assumed to be along the direction from the source to the detector and only in one dimension. Via the Schrödinger equation, the amplitude for the flavor eigenstate  $|\nu_\beta\rangle$  in the detector at  $(L, T)$  is (use the natural units:  $\hbar = c = 1$ ) [29]:

$$\mathcal{A}(\nu_\alpha \rightarrow \nu_\beta; L, E) = \sum_i U_{\alpha i}^* e^{-iE_i t + i p_i L} \langle \nu_\beta | \nu_i, p_i \rangle = \sum_i U_{\alpha i}^* U_{\beta i} e^{-iE_i t + i p_i L}, \quad (2.3)$$

Then the probability of  $\nu_\alpha$  at time  $t_0 = 0$  transforms into a  $\nu_\beta$  at time  $t$  is:

$$\begin{aligned} P(\nu_\alpha \rightarrow \nu_\beta; L, E) &= | \langle \mathcal{A}(\nu_\alpha \rightarrow \nu_\beta; L, E) | \mathcal{A}(\nu_\alpha \rightarrow \nu_\beta; L, E) \rangle |^2 = \\ &(U_{\alpha 1}^* U_{\beta 1} e^{-iE_1 t + ip_1 L} + U_{\alpha 2}^* U_{\beta 2} e^{-iE_2 t + ip_2 L} + \dots) (U_{\alpha 1} U_{\beta 1}^* e^{+iE_1 t - ip_1 L} + U_{\alpha 2} U_{\beta 2}^* e^{+iE_2 t - ip_2 L} + \dots) = \\ &\sum_i |U_{\alpha i}|^2 |U_{\beta i}|^2 + \sum_{i>j} (U_{\alpha i}^* U_{\beta i} U_{\alpha j} U_{\beta j}^*) \exp\{-i(E_i - E_j)t + i(p_i - p_j)L\} + (i \leftrightarrow j), \end{aligned} \quad (2.4)$$

where  $(i \leftrightarrow j)$  stands for the term exchanging index  $i, j$ .

For the second term in 2.4: in the ultra-relativistic case,  $p_i \simeq p_j \equiv p \simeq E \gg m$ , where  $E$  is the average energy. Then  $E_i = \sqrt{p_i^2 + m_i^2} \simeq p + \frac{m_i^2}{2E}$  and thus  $E_i - E_j \simeq \frac{m_i^2 - m_j^2}{2E} \equiv \frac{\Delta m_{ij}^2}{2E}$  [27, 29]. Here  $\Delta m_{ij}^2$  is a set of parameters called mass square difference, popping out in the flavor transition probability. Also,  $L \simeq ct = t$  ( $c \equiv 1$ ). In addition,  $U_{\alpha i}^* U_{\beta i} U_{\alpha j} U_{\beta j}^* = |U_{\alpha i}^* U_{\beta i} U_{\alpha j} U_{\beta j}^*| \exp\{i\phi_{\alpha\beta;ij}\}$ , where  $\phi_{\alpha\beta;ij} = \text{Arg}(U_{\alpha i}^* U_{\beta i} U_{\alpha j} U_{\beta j}^*)$  and  $\phi_{\alpha\beta;ji} = -\phi_{\alpha\beta;ij}$ . Thus the second term containing exp is simplified to be:  $\exp\{-i\frac{\Delta m_{ij}^2}{2E}L + i\phi_{\alpha\beta;ij}\} + (i \leftrightarrow j) = 2 \cos(\frac{\Delta m_{ij}^2}{2E}L - \phi_{\alpha\beta;ij})$ . Therefore, 2.4 can be written as[29]:

$$P(\nu_\alpha \rightarrow \nu_\beta; L, E) = \sum_i |U_{\alpha i}|^2 |U_{\beta i}|^2 + 2 \sum_{i>j} |U_{\alpha i}^* U_{\beta i} U_{\alpha j} U_{\beta j}^*| \cos\left(\frac{\Delta m_{ij}^2}{2E}L - \phi_{\alpha\beta;ij}\right), \quad (2.5)$$

Further expand the second term in 2.5:

$$\begin{aligned} &|U_{\alpha i}^* U_{\beta i} U_{\alpha j} U_{\beta j}^*| \{ \cos(\phi_{\alpha\beta;ij}) \cos\left(\frac{\Delta m_{ij}^2}{2E}L\right) + \sin(\phi_{\alpha\beta;ij}) \sin\left(\frac{\Delta m_{ij}^2}{2E}L\right) \} = \\ &\Re(U_{\alpha i}^* U_{\beta i} U_{\alpha j} U_{\beta j}^*) (1 - 2 \sin^2 \frac{\Delta m_{ij}^2 L}{4E}) + \Im(U_{\alpha i}^* U_{\beta i} U_{\alpha j} U_{\beta j}^*) \sin \frac{\Delta m_{ij}^2 L}{2E}, \end{aligned} \quad (2.6)$$

Since the mass eigenstates have relation  $\langle \nu_j | \nu_i \rangle = \delta_{ij}$  and the matrix  $U$  is unitary, Maximum oscillation occurs at  $\frac{\Delta m^2}{4E}L \sim \pi$ , which gives an effective length  $L^{osc} = 4\pi E / \Delta m^2$ .

For a set of units commonly used by experiments, a neutrino with energy  $E_\nu$ , after flying for a distance of  $L$ , has an oscillation probability of:

$$P_{\nu_e \rightarrow \nu_\mu} = \sin^2(2\theta) \sin^2 \left( \frac{1.27 \Delta m^2 [eV^2] L [km]}{E_\nu [GeV]} \right). \quad (2.7)$$

The survival probability is defined as:

$$P_{\nu_e \rightarrow \nu_e} = 1 - P_{\nu_e \rightarrow \nu_\mu}. \quad (2.8)$$

$$P_{\alpha\beta} = \delta_{\alpha\beta} - 4 \sum_{i>j} \Re[U_{\beta i} U_{\alpha i}^* U_{\alpha j} U_{\beta j}^*] \sin^2 \frac{\Delta m_{ij}^2 L}{4E} + 2 \sum_{i>j} \Im(U_{\beta i} U_{\alpha i}^* U_{\alpha j} U_{\beta j}^*) \sin \frac{\Delta m_{ij}^2 L}{2E}$$

In addition, there are two squared-mass differences,  $\Delta m_{21}^2 = m_2^2 - m_1^2$  and  $\Delta m_{32}^2 = |m_3^2 - m_2^2|$ . The sign of  $\Delta m_{32}^2$  is unknown and it indicates a mass hierarchy problem of whether neutrino mass is normal hierarchy (NH,  $m_3 > m_2 > m_1$ ) or inverted hierarchy (IH,  $m_3 < m_1 < m_2$ )[27].

Currently, these six parameters have been measured by neutrino oscillation experiments. These experiments can be classified by the neutrino sources they use. They are the solar, the reactor, the atmospheric, the accelerator and the astronomical and cosmological neutrino experiments. Table 2.2 lists the energy scale of the neutrino source as well as the example experiments.

Table 2.2: Oscillation neutrino experiments.

type	source	$E_\nu$	example
solar	the Sun	MeV scale	SNO
reactor	reactor	MeV scale	DayaBay
atmospheric	cosmic-ray	GeV scale	SuperK
accelerator	$\nu$ beam from accelerator	GeV scale	T2K
astronomical	astronomical objects	GeV-EeV scale	IceCube

For the  $\Delta m_{21}^2$  and  $\theta_{12}$ , the combined analysis of the measurements from the reactor experiment KamLAND and SNO gave  $\Delta m_{21}^2 = 7.59_{-0.21}^{+0.21} \times 10^{-5} eV^2$  and  $\tan^2 \theta_{21} = 0.47_{-0.05}^{+0.06}$ [30].

The accelerator neutrino experiments as well as the atmospheric neutrino experiments have measured  $\Delta m_{32}^2$  and  $\theta_{23}$ . The most recent results from SuperK show that in NH,  $\sin^2 \theta_{23} = 0.588_{-0.064}^{+0.031}$  and  $\Delta m_{32}^2 = 2.5_{-0.20}^{+0.13} \times 10^{-3} eV^2$ [31].

In 2012, the reactor neutrino experiment Daya Bay reported the discovery of non-zero  $\theta_{13}$  with a significance of  $5.2\sigma$ . In 2016, Daya Bay reported that  $\sin^2 2\theta_{13} = 0.0841 \pm 0.0027(stat.) \pm 0.0019(syst.)$ . This high-precision result makes  $\sin^2 2\theta_{13}$  the best measured mixing angle[32, 33].

$\delta_{CP}$  is examined by the experiments which measure the difference between neutrino and antineutrino oscillation probabilities  $P(\bar{\nu}_\alpha \rightarrow \bar{\nu}_\beta)$  and  $P(\nu_\alpha \rightarrow \nu_\beta)$ [?]. In 2017, the Tokai-to-Kamioka (T2K) experiment in Japan rejected the hypothesis that neutrinos and antineutrinos oscillate with the same probability at 95% confidence ( $2\sigma$ ) level. This indicates a hint of CP symmetry broken by neutrinos[34]. In 2019, T2K claimed confidence intervals for  $\delta_{CP}$  with three standard deviations ( $3\sigma$ ): [-3.41,-0.03] for NH and [-2.54,-0.32] for IH. This result indicates that the CP violation exists in leptons[35].

The oscillation probability in matter can be written in a concise and exact form as [36]:

$$P(\nu_e \rightarrow \nu_\mu) = A \cos \delta + B \sin \delta + C$$

will also provide the information for the CP- and T-violation by investigating the quantities of:

$$A_{CP} = \frac{P(\nu_\alpha \rightarrow \nu_\beta) - P(\bar{\nu}_\alpha \rightarrow \bar{\nu}_\beta)}{P(\nu_\alpha \rightarrow \nu_\beta) + P(\bar{\nu}_\alpha \rightarrow \bar{\nu}_\beta)}$$

$$A_T = \frac{P(\nu_\alpha \rightarrow \nu_\beta) - P(\bar{\nu}_\beta \rightarrow \bar{\nu}_\alpha)}{P(\nu_\alpha \rightarrow \nu_\beta) + P(\bar{\nu}_\beta \rightarrow \bar{\nu}_\alpha)}$$

### 2.1.2 Matter Effect

The matter effect is caused by neutrinos interacting with ambient electrons and nucleons in matter such as the Sun or the Earth.  $\nu_e$  interacts with electrons via both charged weak current (exchanging  $W$  boson) and neutral weak current ( $Z$  boson) while  $\nu_\mu$  and  $\nu_\tau$  interact only by the neutral current. The  $\nu_e$  energy has an addition term,  $V_{CC} = \sqrt{2}G_F n_e$ , where  $n_e$  is the number density of the electrons in matter and  $G_F$  is the Fermi coupling constant for the weak interaction. This affects the oscillation probabilities for neutrinos propagating in matter compared to vacuum, which is called the Mikheyev-Smirnov-Wolfenstein (MSW) mechanism[37, 38].

In vacuum two-flavor mixing, the Schrödinger equation can be written (in natural units)[39]:

$$i \frac{d}{dt} \begin{bmatrix} \nu_e \\ \nu_\mu \end{bmatrix} = H_0^f \begin{bmatrix} \nu_e \\ \nu_\mu \end{bmatrix}, \quad (2.9)$$

where

$$H_0^f = \frac{1}{2E} \begin{bmatrix} m_1^2 \cos^2 \theta + m_2^2 \sin^2 \theta & (m_2^2 - m_1^2) \sin \theta \cos \theta \\ (m_2^2 - m_1^2) \sin \theta \cos \theta & m_1^2 \sin 2\theta + m_2^2 \cos^2 \theta \end{bmatrix} = \frac{\Delta m_{21}^2}{4E} \begin{bmatrix} -\cos 2\theta & \sin 2\theta \\ \sin 2\theta & \cos 2\theta \end{bmatrix} + \frac{(m_1^2 + m_2^2)}{4E} \begin{bmatrix} 1 & 0 \\ 0 & 1 \end{bmatrix}, \quad (2.10)$$

and  $\Delta m_{21}^2 = (m_2^2 - m_1^2)$ .

To simplify the calculation, we can drop the second unitary term of  $H_0^f$  that is irrelevant to the neutrino flavor transformation. Including the matter effect, we obtain:

$$H_m = \begin{bmatrix} -\frac{\Delta m_{21}^2}{4E} \cos 2\theta + \sqrt{2}G_F n_e & \frac{\Delta m_{21}^2}{4E} \sin 2\theta \\ \frac{\Delta m_{21}^2}{4E} \sin 2\theta & \frac{\Delta m_{21}^2}{4E} \cos 2\theta \end{bmatrix} \quad (2.11)$$

We define a mixing angle in matter,  $\theta_m$  as:

$$\tan 2\theta_m = \frac{\Delta m^2 \sin 2\theta}{\Delta m^2 \cos 2\theta - 2\sqrt{2}EG_F n_e}, \quad (2.12)$$

and define an effective squared-mass difference in matter  $\Delta m_m^2$  as:

$$\Delta m_m^2 = \sqrt{(\Delta m^2 \cos 2\theta - 2\sqrt{2}EG_F n_e)^2 + (\Delta m^2 \sin 2\theta)^2}. \quad (2.13)$$

In analogy with mixing in vacuum, we can write the mixing equation relating the energy eigenstates in matter ( $\nu_{1m}, \nu_{2m}$ ) to the flavor eigenstates with a diagonalized Hamiltonian:

$$\begin{bmatrix} \nu_e \\ \nu_\mu \end{bmatrix} = \begin{bmatrix} \cos \theta_m & \sin \theta_m \\ -\sin \theta_m & \cos \theta_m \end{bmatrix} \begin{bmatrix} \nu_{1m} \\ \nu_{2m} \end{bmatrix}. \quad (2.14)$$

The probability of flavor transformation in matter is:

$$P_{\nu_e \rightarrow \nu_\mu} = \sin^2(2\theta_m) \sin^2 \left( \frac{\Delta m_m^2 L}{4E} \right). \quad (2.15)$$

The denominator in equation (2.12) implies a resonance condition:

$$V(n_e) = \sqrt{2}G_F n_e = \frac{\Delta m^2 \cos 2\theta}{2E}. \quad (2.16)$$

From this condition, for a given  $E$ , there is a resonance density  $n_e^{reson}$  while for a given  $n_e$ , there is a resonance energy  $E^{reson}$ . When the resonance condition is satisfied,  $\theta_m = \frac{\pi}{4}$  and two flavor neutrinos are maximally mixed, even if the vacuum mixing angle  $\theta$  is small. This is called matter enhanced neutrino oscillation[37, 40].

### 2.1.3 Reactor-solar Experiments

## 2.2 Solar Neutrinos

Since neutrinos' extremely low interaction cross-sections, neutrinos produced in the Sun can reach the detectors on the Earth without being interrupted. This enables the solar neutrino to be a probe to the stellar physics.

KamLand

Daya Bay

The Jiangmen Underground Neutrino Observatory (JUNO) is a reactor neutrino experiment located at Kaiping, Jiangmen in Southern China. a large liquid scintillator detector large active mass of 20 kton

the energy resolution (3% at 1 MeV) [41]

## 2.3 Majorana Neutrino

Dirac equation ( $i\gamma^\mu \partial_\mu - m\psi = 0$ , get coupled equations

The interpretation of the  $0\nu\beta\beta$  process is considered as exchanging light Majorana neutrinos. In this case the effective Majorana mass  $\langle m_{ee} \rangle = \sum_{i=1}^3 |U_{ei}|^2 m_i$  ( $i = 1, 2, 3$ ), where  $U_{ei}$  are the elements of the neutrino mixing matrix for the flavor state  $\nu_e$ , and  $m_i$  are the mass eigenvalues of the mass eigenstates (from (2.1)). The observable quantity is the half-life:

$$(T_{1/2}^{0\nu\beta\beta})^{-1} = G_{PS}(Q, Z) |M_{Nuclear}|^2 \langle m_{ee} \rangle^2,$$

Majorana found a representation of the  $\gamma$ -matrices as follow:

$$\gamma_M^0 = \begin{pmatrix} 0 & \sigma^2 \\ \sigma^2 & 0 \end{pmatrix}, \gamma_M^1 = \begin{pmatrix} \sigma^3 & 0 \\ 0 & \sigma^3 \end{pmatrix}, \gamma_M^2 = \begin{pmatrix} -\sigma^2 & 0 \\ 0 & \sigma^2 \end{pmatrix}, \gamma_M^3 = -i \begin{pmatrix} \sigma^1 & 0 \\ 0 & \sigma^1 \end{pmatrix}$$

These matrices themselves are pure imaginary.

$$C^{-1}\gamma_\mu C = -\gamma_\mu^T$$

For heavy radioactive isotopes with nuclei of even neutron number ( $N$ ) and even proton number ( $Z$ ) (called even-even nucleus), beta decay will lead to an odd-odd nucleus which is less stable. For some such isotopes the beta decay is energetically forbidden. In 1935, Maria Goeppert-Mayer pointed out that they can still decay through a double beta decay process:  $(Z, A) \rightarrow (Z + 2, A) + 2e^- + 2\nu_e + Q_{\beta\beta}$ , where the  $Q_{\beta\beta}$  is the released energy. This is called ordinary double beta decay or  $2\nu\beta\beta$ , which is allowed by the Standard Model and with a typical half-life  $T_{1/2} > 10^{19}$  years[?].

If neutrinos are Majorana particles, a process called neutrinoless double beta decay ( $0\nu\beta\beta$ ) will also be expected. The Feynman diagrams of  $2\nu\beta\beta$  and  $0\nu\beta\beta$  are illustrated in Fig. 2.2.

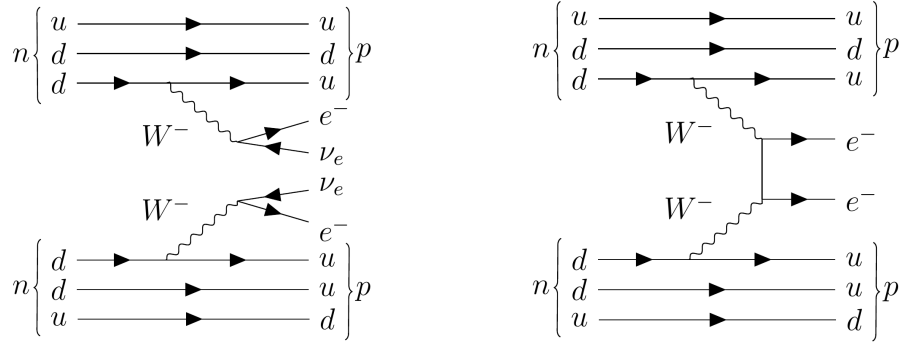


Figure 2.2: Feynman diagrams for  $2\nu\beta\beta$  (left) and  $0\nu\beta\beta$  (right).

The interpretation of the  $0\nu\beta\beta$  process is considered as exchanging light Majorana neutrinos. In this case the effective Majorana mass  $\langle m_{ee} \rangle = \sum_{i=1}^3 |U_{ei}|^2 m_i$  ( $i = 1, 2, 3$ ),  $U_{ei}$  are the elements of the neutrino mixing matrix for the flavor state  $\nu_e$ , and  $m_i$  are the mass eigenvalues of the mass eigenstates (from (2.1)). The observable quantity is the half-life:

$$(T_{1/2}^{0\nu\beta\beta})^{-1} = G_{PS}(Q, Z)|M_{Nuclear}|^2 \langle m_{ee} \rangle^2,$$

where  $G_{PS}$  is the phase space factor and  $|M_{Nuclear}|$  is the nuclear matrix element for the physics process describing the  $0\nu\beta\beta$  decay process[42].

Similar to beta decay, the  $2\nu\beta\beta$  process will cause a continuous spectrum in the detector while the  $0\nu\beta\beta$  process only has two electrons in the final state, which sum up to give a

distinct energy peak. By measuring this exact energy, a detector with high energy resolution is able to search for the  $0\nu\beta\beta$  signal from the  $0\nu\beta\beta$  decay radioactive isotopes. Diverse technologies have been developed during the past decades. The following section lists some of the mainstream experiments.

$$\Psi_R = \begin{bmatrix} \psi_R \\ \psi_R^C \end{bmatrix}, \Psi_L = \begin{bmatrix} \psi_L \\ \psi_L^C \end{bmatrix}, M = \begin{bmatrix} m_L^M & m^D \\ m^D & m_R^M \end{bmatrix}, \quad (2.17)$$

The mass eigenstates:

$$m_{\pm} = \frac{1}{2} [ (m_L^M + m_R^M) \pm \sqrt{(m_L^M - m_R^M)^2 + 4(m^D)^2} ],$$

from (2.3), there are 4 cases for discussion:

- (1) If  $m_L^M = m_R^M = 0$ ,  $m_{1,2} = m^D$ , neutrinos are pure Dirac particles.
- (2) If  $m^D \gg m_{L,R}^M$ ,  $\frac{m^D}{m_{L,R}^M} \rightarrow 0$ ,  $m_{1,2} = \frac{1}{2}m^D \left[ \frac{(m_L^M + m_R^M)}{m^D} + \sqrt{\left(\frac{m_L^M - m_R^M}{m^D}\right)^2 + 4} \right] \approx m^D$ , neutrinos are Pseudo-Dirac-Neutrinos.
- (3) If  $m^D = 0$ ,  $m_1 = m_L^M$ ,  $m_2 = m_R^M$ , neutrinos are pure Majorana particles.
- (4) In the case of the seesaw mechanism, where  $m_R^M \gg m^D$ ,  $m_L^M = 0$ , and for  $(\frac{m^D}{m_R^M})^2 \rightarrow 0$ , use  $(1+x)^\alpha \sim 1 + \alpha x$  (*if*  $x \rightarrow 0$ ), we get:

$$m_1 = m_- = \frac{\frac{1}{2}[(m_R^M)^2 - (m_R^M)^2 - 4(m^D)^2]}{m_R^M(1 + \sqrt{1 + 4(\frac{m^D}{m_R^M})^2})} \approx -\frac{(m^D)^2}{m_R^M},$$

$$m_2 = m_+ = \frac{1}{2}[m_R^M + m_R^M(1 + \frac{1}{2}(\frac{2m^D}{m_R^M})^2)] = m_R^M[1 + (\frac{m^D}{m_R^M})^2] \approx m_R^M.$$

For  $\mathcal{O}(1TeV)$ , the  $\nu$  mass is  $0.1\text{ eV}$

### 2.3.1 Status of Double Beta Decay Experiments

There are 35 isotopes can undergo the double beta decay process, but only a few of them are suitable for the application in direct  $0\nu\beta\beta$  search experiments[19]. From the experimental view, the candidate isotopes are expected to have relatively high natural abundances, high Q-values, be deployed in a large amount with low costs, and are not toxic to the environment

as well. However, in realistic situation there is no isotope fulfills all these properties and the current experiments making trade-offs[43].

The experiments searching for direct signals of  $0\nu\beta\beta$  mainly measure the physics properties of the two emitted electrons, such as their energies, momentum and tracks.

inhomogeneous experiments use external  $\beta\beta$  source while homogeneous experiments use  $\beta\beta$  source as the detection medium, which are mainly referred as calorimeter experiments[44, 45].

$^{136}\text{Xe}$ ,  $^{48}\text{Ca}$ ,  $^{76}\text{Ge}$ ,  $^{130}\text{Te}$

At the time of writing,

$0\nu\beta\beta$  in the range of  $10^{25} - 10^{26}$  year,

The observed number of event in expectation is:

$$N_{event} = \ln 2 \frac{N_A \alpha \cdot \epsilon \cdot m \cdot t}{M_A T_{1/2}^{0\nu}},$$

where  $N_A$  is the Avogadro's number,  $\alpha$  is the abundance of the isotope in the element,  $M$  is the molar mass of the isotope and  $t$  is the measurement time of total exposure.

The GERmanium Detector Array (GERDA) experiment searches for  $0\nu\beta\beta$  of  $^{76}\text{Ge}$ . The experiment uses bare germanium crystals with an enrichment of up to  $\sim 87\%$   $^{76}\text{Ge}$  operated in a radiopure cryogenic liquid argon (LAr)[46]. GERDA Phase I had an exposure of 21.6 kg·yr and Phase-II started with 35.6kg from enriched material in December 2015. With combined data of Phase I and Phase II,

a total exposure of 82.4 kg·yr

In 2017, GERDA reported a 90% confidence level (C.L.) lower limit for the half-life of  $^{76}\text{Ge}$ ,  $T_{1/2}^{0\nu}(^{76}\text{Ge}) > 8.0 \times 10^{25}$  years.

GERDA reported in 2019 a lower limit half-life of  $T_{1/2}^{0\nu}(^{76}\text{Ge}) > 0.9 \times 10^{26}$  years at 90% C.L.[47]. effective  $m_{ee}$  is [104,228] meV.

The Enriched Xenon Observatory (EXO) experiment uses 200-kg liquid Xenon (LXe) time projection chamber (TPC) to search for  $0\nu\beta\beta$  in  $^{136}\text{Xe}$ . In 2011 they observed the half life of double beta decay of  $^{136}\text{Xe}$  to be  $2.11 \times 10^{21}$  years and in 2014 they set a limit on  $T_{1/2}^{0\nu}(^{136}\text{Xe}) > 1.1 \times 10^{25}$  yr[?]. EXO is now upgrading to the next 5-tonne experiment

(nEXO) and is expected to reach an exclusion sensitivity of  $T_{1/2}^{0\nu}(^{136}\text{Xe})$  to about  $10^{28}$  years at 90% C.L.[48].

Also looking into  $^{136}\text{Xe}$ , the KamLAND-Zen (ZEroNeutrino) experiment exploits the existing facilities of KamLAND by setting a 3.08-m-diameter spherical inner balloon filled with 13 tons of Xe-loaded liquid scintillator at the center of the KamLAND detector.

liquid scintillator cocktail of 82% decane and 18% pseudocumene by volume, 2.7 g/L PPO.

photocathode coverage of 34%.

Their 2016 results from a 504 kg·yr exposure obtained a lower limit for the  $0\nu\beta\beta$  decay half-life of  $T_{1/2}^{0\nu}(^{136}\text{Xe}) > 1.07 \times 10^{26}$  yr at 90% C.L. and the corresponding upper limits on the effective Majorana neutrino mass are in the range 61 – 165 meV[?].

The Particle and Astrophysical Xenon Experiment III (PandaX-III) high pressure gas-phase time projection chamber (TPC)

The Cryogenic Underground Observatory for Rare Events (CUORE) experiment searches for  $0\nu\beta\beta$  in  $^{130}\text{Te}$ . CUORE is a ton-scale cryogenic bolometer array that arranges 988 tellurium dioxide ( $\text{TeO}_2$ ) crystals. CUORE reported first results in 2017 after a total  $\text{TeO}_2$  exposure of 86.3 kg·yr. An effective energy resolution of  $(7.7 \pm 0.5)$  keV FWHM and a background count of  $(0.014 \pm 0.002)$  counts/(keVkgyr) in the ROI were achieved in that data exposure. Combined with the early data (the data from the two precursor experiments, Cuoricino and CUORE-0), they placed a lower limit of  $T_{1/2}^{0\nu}(^{130}\text{Te}) > 1.5 \times 10^{25}$  yr at 90% C.L. and  $m_{\beta\beta} < (110 - 520)$  meV[49]. In five years live time, the experiment will give a projected sensitivity of  $9.5 \times 10^{25}$  yr at the 90% C.L. and set an upper limit on the effective Majorana mass in the range 50 – 130 meV[50].

## Chapter 3

# The SNO+ Experiment

### 3.1 Overview

The SNO+ experiment is located at SNOLAB in Vale’s Creighton mine in Sudbury, Ontario, Canada (coordinate:  $46^{\circ}28'19.6''\text{N}$ ,  $81^{\circ}11'12.4''\text{W}$ ). The deep underground facility of the SNOLAB provides an environment with extremely low cosmic ray backgrounds. At sea level, an average cosmic muon ( $\mu$ ) flux rate is about  $1.44 \times 10^7 \mu/\text{m}^2/\text{day}$ [51]. Cosmic muons with high energies ( $\mathcal{O}(\text{GeV})$ ) can induce spallation backgrounds, such as fast neutrons and lasting isotopes, which are harmful to the low background counting experiments[52]. The SNOLAB has a  $2092 \pm 6$  m flat overburden of rock, which is  $5890 \pm 94$  water equivalent meter (m.w.e). This rock overburden ensures that cosmic muon ( $\mu$ ) flux rate is as low as  $0.286 \pm 0.009 \mu/\text{m}^2/\text{day}$ , which means that every hour only about 1  $\mu$  passes through the SNO+ detector.

The SNO+ detector is the successor of the SNO experiment. The detector makes use of the SNO structure and has done a few upgrades. As shown in Fig. 3.1, the detector consists of an acrylic vessel (AV) sphere of 12 m in diameter and 5.5 cm in thickness. The AV sphere is concentric within a stainless steel photomultiplier(PMT) support structure (PSUP), which is a geodesic dome with an average radius of 8.4 m. The Hamamatsu 8-inch R1408 PMTs are mounted on the PSUP. 9394 PMTs are looking inward to the AV,

giving a 50% effective coverage, while 90 PMTs are looking outward, serving as muon vetos. These two structures are housed in a rock cavity filled with 7000 tonnes of ultrapure water (UPW) to provide both buoyancy for the vessel and radiation shielding of the surrounding backgrounds, such as the cosmic rays and isotope decays from the rock.

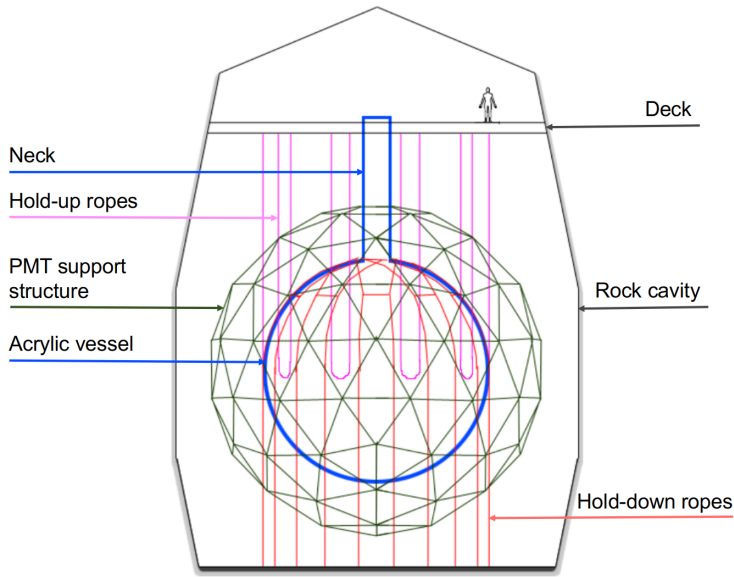


Figure 3.1: The SNO+ detector labelled with main structures, figure modified from [2].

## 3.2 SNO+ Physics Phases

The SNO+ experiment is designed for multi-purpose measurements of neutrino physics. The detector has been running since December 2016. There are three physics phases of the experiment[53]:

### 1. Water phase

The AV was filled with about 905 tonnes of ultra pure water (UPW). The detector collected water physics data from May 2017 to July 2019.

The main physics goal in this phase is to search for the invisible nucleon decay, which violates baryon number and is a prediction of Grand Unified Theory (GUT). In the invisible decay mode, a proton or a bound neutron decays away without releasing charged particles,

compared to the “visible” decay channels of  $p \rightarrow e\pi$  and  $p \rightarrow \nu K$  which has been searched and set limits by the SuperK experiment. In the SNO+ water detector,  $^{16}\text{O}$  may decay into  $^{15}\text{O}^*$  (bound neutron invisible decay) or  $^{15}\text{N}^*$  (proton invisible decay) excited state. The  $^{15}\text{O}^*$  has 44% chance to deexcite to produce 6.18 MeV  $\gamma$  ray and 2% chance to produce 7.03 MeV  $\gamma$ ; while  $^{15}\text{N}^*$  has 41% to release 6.32 MeV  $\gamma$  and 7.01, 7.03 and 9.93 MeV  $\gamma$  with chances of 2%, 2% and 3% respectively. The experiment has searched for these  $\gamma$  signals and sets world-leading limits of  $\mathcal{O}(10^{29})$  years for both the proton and neutron invisible decay lifetime at 90% Bayesian credibility level[54]. Meanwhile, the solar neutrinos were measured with very low backgrounds compared to the other water Cherenkov detectors.

and neutron captures in water are also studied.

During the water phase, different types of calibration runs have been taken. The detector timing and energy response, systematics and backgrounds are studied. Multiple physics analyses of solar neutrinos, reactor antineutrinos and nucleon decay are going on. The external backgrounds are also measured, which will be the same as the following two phases.

## 2. Scintillator phase

The AV will be filled with 780 tonnes of liquid scintillator, which is a mixture of linear alkylbenzene (LAB) as a solvent and 2 g/L of 2,5-diphenyloxazole (PPO) as a fluor.

In this phase, the main physics goal is to measure low energy solar neutrinos: the CNO, pep and low energy  $^8\text{B}$  neutrinos. The pep neutrinos are mono-energetic, with  $E_\nu = 1.442$  MeV and their flux is well predicted by the Standard Solar Model. A measurement of the pep neutrinos will give more information of the matter effects in neutrino oscillations[?].

The solar metallicity is the abundance of elements heavier than  $^4\text{He}$  (called “metal” elements in the context of astronomy). It is poorly constrained and the predictions from different solar models disagree with each other. A measurement of the CNO neutrinos can give the abundance of  $^{12}\text{C}$ ,  $^{13}\text{N}$  and  $^{15}\text{O}$  and can thus resolve the metallicity problem[?].

Geoneutrino, reactor antineutrino and supernova neutrino detections are additional goals.

A six-month period of scintillator filling and six to twelve months of data-taking are

expected for this phase. During the filling, it is planned to operate the partially filled detector at a water level about 4.4 m for about two weeks. This partial filled transition phase is mainly aimed to understand the in-situ backgrounds of scintillator.

### 3. Tellurium loading phase

In this final phase, 0.5% natural Tellurium (Te) by mass (with 1.3 kilotonnes of  $^{130}\text{Te}$ ) will be loaded into the scintillator. Higher loading concentrations would be possible for a further loading plan[55]. The main purpose of this phase is to search for the  $0\nu\beta\beta$  signals in  $^{130}\text{Te}$ .

## 3.3 Detection Medium

In the SNO+ detector, charged particles are expected to interact with the detection medium and create Cherenkov lights and scintillation lights.

### 3.3.1 Cherenkov Radiation

For any charged particle travelling in a transparent medium at an ultrarelativistic speed (a speed greater than the local phase speed of light in the medium), an electromagnetic radiation, called Cherenkov radiation, can be emitted from the coherent response of the medium under the action of the field of the moving particle[56, 57].

Suppose a charged particle moves in a transparent, isotropic and non-magnetic medium and creates an electromagnetic wave. The electromagnetic wave propagates with a wave number  $k = n \cdot \omega/c$ , where  $c$  is the speed of light in vacuum,  $n$  is the real-valued refractive index and  $\omega$  is the frequency. If the particle travels uniformly along x axis with a velocity of  $v$ , the x-component of the wave vector is  $k_x = \omega/v$ . For a freely propagating wave,  $k > k_x$ , therefore  $v > v_p = c/n(\omega)$ , where  $v_p$  is the phase velocity in the medium. Under this condition that the speed of the charged particle is greater than the  $v_p$ , the Cherenkov radiation is emitted with a frequency of  $\omega$ [57].

The Cherenkov angle,  $\theta_c$  is the angle between the direction of the particle and the direction of Cherenkov emission and it is well-defined by  $\cos \theta_c(\omega) = \frac{c}{n(\omega)v}$ . The radiation

is distributed over a surface of a cone with the half-opening angle  $\theta_c$ .

Consider the condition  $v > v_p = c/n(\omega)$ , for the case of  $e^-$  travelling in a water detector, if neglecting the dependency on  $\omega$ ,  $n_{water} \simeq 1.33$  [27], then  $\theta_c \simeq 41.25^\circ$  and  $v_p \simeq 2.254 \times 10^8 \text{ m/s}$ , which corresponds to a kinetic energy  $E_k = (\gamma - 1)mc^2 = 0.264 \text{ MeV}$  for  $e^-$ , where  $\gamma = 1/\sqrt{1 - v_p^2/c^2}$ . This is the lowest kinetic energy to create Cherenkov radiation, which is referred to the Cherenkov threshold ( $E_{thresh}$ ). In the case that the LAB-PPO liquid scintillator is the medium,  $n \simeq 1.50$ [58],  $\theta_c \simeq 48.19^\circ$  and for  $e^-$ ,  $E_{thresh} \simeq 0.175 \text{ MeV}$ .

For a particle with a charge of  $ze$ , the number of photons produced by Cherenkov radiation per unit path length and per unit frequency of the photons is given by[59]:

$$\frac{d^2N}{d\omega dx} = \frac{\alpha^2(ze)^2}{c} \sin^2 \theta_c = \frac{z^2\alpha}{c} \left(1 - \frac{1}{\beta^2 n^2(\omega)}\right),$$

where  $\alpha$  is the fine structure constant.

Translate the frequency into the wavelength ( $\lambda = 2\pi\omega$ ) and integrate over the wavelength, we have the number of photons and  $x$  is along the particle track[59]:

$$\frac{dN}{dx} = 2\pi(ze)^2 \alpha \sin \theta_c \int_{\lambda_1}^{\lambda_2} \frac{d\lambda}{\lambda^2},$$

For optical photons with wavelengths ranging from 350 to 550 nm (typical PMT detection sensitive range), the above formula can be calculate into[59]:

$$\frac{dN}{dx} = 476(ze)^2 \sin^2 \theta_c \text{ photons/cm.}$$

For the Cherenkov radiation caused by  $e^-$  in a water detector,  $dN/dx \simeq 207 \text{ photons/cm}$ ; while in the LAB-PPO case:  $dN/dx \simeq 264 \text{ photons/cm}$ . In a realistic measurement, the detection efficiency and the coverage of photon sensors are also required to be taken into account.

### 3.3.2 Scintillation from Organic Scintillator

Besides the Cherenkov photons described in the last section, the majority lights emitted from organic scintillator are scintillation photons.

The organic liquid scintillator can convert the kinetic energy of charged particles into scintillation photons with wavelengths in the sensitive detection region of PMTs. They are aromatic hydrocarbon compounds with benzene-ring structures. When ionizing radiation happens in the scintillator, the free valence electrons of the molecules are excited and transit to occupy the  $\pi$ -molecular orbitals with the benzene rings. These highly delocalized electrons are called  $\pi$ -electrons, which can occupy a series of energy levels. A Jablonski diagram, invented by Polish physicist Aleksander Jabłoński, is generally used to describe molecular absorbance and emission of light. In Fig. 3.2, the Jablonski diagram illustrates the  $\pi$ -electronic energy levels of an organic scintillator molecule[4, 59].

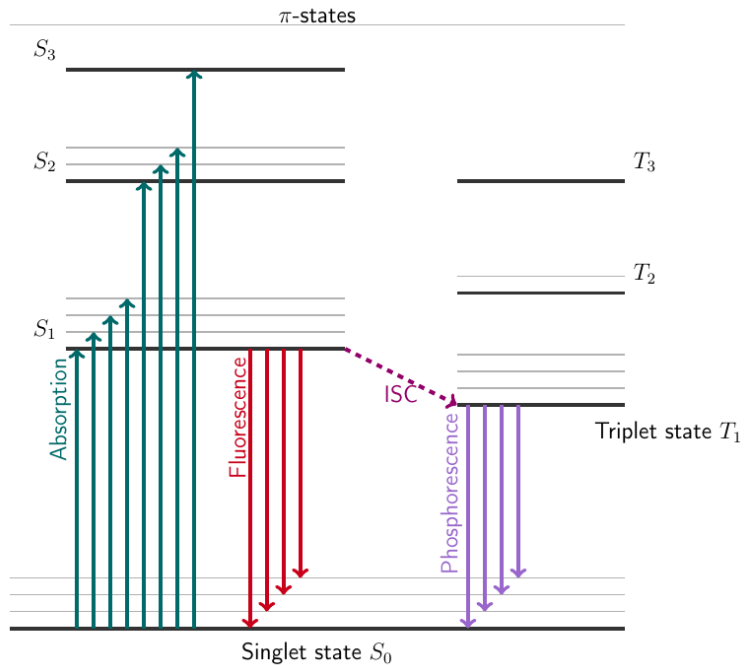


Figure 3.2: A Jablonski diagram for the organic scintillator, modified from [3, 4].

In the diagram,  $S_{0,1,2,3,\dots}$  are the energy levels of the spin-0 singlet states, where  $S_0$  is the ground state and  $S^* = S_{1,2,3,\dots}$  are the excited singlet states. Above the ground state  $S_0$ , there are also a set of spin-1 triplet states  $T_{1,2,3,\dots}$ , where  $T_1$  is the lowest triplet state. These electron energy levels are labelled with thick black lines. The energy spacing between these levels are  $\mathcal{O}(eV)$ . In each levels, there are also fine structure levels which corresponds

to excited vibration modes of the molecule (labelled with gray lines and can be marked as  $S_{10}, S_{11}, \dots, S_{20}, S_{21}, \dots$ ). The energy spacing between these fine levels are  $\mathcal{O}(0.15 \text{ eV})$ [59, 4].

The ionization radiation transfers the energy to the molecules and excites the electron levels as well as the vibrational levels, labelled as the absorption lines (in green). The decays between the excited singlet states (not to the ground state) are almost immediate ( $\leq 10 \text{ ps}$ ) without the emission of light. This process is called internal degradation. The decays from the excited singlet state  $S_1$  (as well as the vibrational states  $S_{10}, S_{11}, S_{12}, \dots$ ) to the ground state (as well as the vibration states  $S_{01}, S_{02}, \dots$ ) happen promptly ( $\mathcal{O}(ns)$ ) and emit lights (labelled as red lines). This process is called fluorescence which contributes the prompt component of the emission of scintillation light. The probability of  $S_1$  decays into the vibrational states  $S_1 \rightarrow S_{01}, S_{02}, \dots$  among the ground state is more than  $S_1 \rightarrow S_0$ . Since the absorbed energy of  $S_0 \rightarrow S_1$  is larger than the emitted energy of  $S_1 \rightarrow S_{01}, S_{02}, \dots$ , the scintillators have very little self-absorption of the fluorescence and are transparent to their own radiation. The effect of Stokes shift, which refers to the overlap between the optical absorption and emission spectra, is small for the organic scintillator[59, 4].

The transitions between the singlet and triplet states are highly forbidden due to the electron spin-flip is involved[60, 61]. There also exists a relatively rare process called inter-system crossing (ISC), which converts excited singlet states into triplet states. Besides this, 75% of triplet states can be produced by ionization-recombination[60, 62].

For the de-excitation, the similar processes of internal degradation occur among  $T_{2,3,\dots} \rightarrow T_1$ .  $T_1$  is a relatively stable state and the lifetime of the molecule in the triplet state is in  $\mathcal{O}(10^{-4} - 10 \text{ s})$ [63].  $T_1 \rightarrow S_0$  is highly forbidden. However, the  $T_1$  state can go through an indirect decay process by interacting with another excited  $T_1$  molecule and forms an excited singlet state:



The  $S^*$  will de-excite and emit delayed scintillation light. The process for emitting this delayed scintillation light is called delayed fluorescence or phosphorescence[59]. This process contributes to the delayed component of scintillation light.

For a typical scintillator detector, the time scale of detector response is  $\mathcal{O}(1\text{--}100\text{ ns})$ . In this time region, the emission of the scintillation light contains the primary fluorescence from the de-excitation of the singlet states (prompt component) and the delayed fluorescence from the de-excitation of the indirect triplet states (delayed component)[62]. The time profile of the scintillation light emission is a mixture of prompt and delayed components.

Different charged particles can cause different ionization density when they deposit energies to the scintillator molecules. The ionization density affects the relative population of the excited singlet and triplet states. Compared to an  $e^-$ , an  $\alpha$  particle can cause a high ionization density, which produces higher ratio of triplet states. Therefore, the time profile for the  $\alpha$  particle has more delayed component or longer tails than the  $e^-$ . This enables the organic scintillator to distinguish  $\alpha$  with  $e^-$  or other lighter charged particles[62, 64].

an empirical formula, called follows Birk's law[65, 3], describes the photon yield along unit distance by the incident particle:

$$\frac{dY}{dx} = A \frac{dE/dx}{1 + k_B \cdot dE/dx},$$

where  $A$  is a normalization constant,  $k_B$  is the Birks' constant of the scintillator, which in practice is obtained by fitting the formula to the measured data.

### 3.3.3 Liquid Scintillator for SNO+

The SNO+ collaboration has been developing liquid scintillator

Linear Alkyl Benzene (LAB)

is provided by CEPSA Química Bécancour Inc. Organic liquid scintillators The advantages of LAB are:

As mentioned in 3.1,

- It has very low levels of natural radioactive contaminants such as U, Th and K.
- High light yield and attenuation length.
- It has fast timing response different timing spectrum for  $\alpha$  and  $\beta$  events, which enables an  $\alpha - \beta$  discrimination.

- High flash point and low toxicity for lab safety.
- appropriate density for mechanical stability
- Good stability and chemically compatible with detector materials, mainly the AV.
- Low cost.

An additional wavelength shifter, 2,5-diphenyloxazole (PPO) is usually added and dissolved into the LAB [66]. This wavelength shifter is used as a fluor and it can shift the wavelengths of the scintillation photons to a range of 300-550 nm, which is the sensitive range of the PMT detection. A 2 g/L PPO concentration in LAB is optimized by SNO+[53]. The absolute light yield of the LAB-PPO liquid scintillator has been well-measured from large particle physics experiments [cite dayabay, borexino] as well as bench-top measurements [cite dayabayBench, novikov, tanner]. The absolute light yield of LAB+2g/L PPO liquid scintillator determined by SNO+ is 11900 photons/MeV [cite lightyield].

#### Te-loaded liquid scintillator (TeLS)

To load the tellurium into the liquid scintillator, a compound is made by condensation reactions between telluric acid (TeA) and 1,2-butanediol (BD), with N,N-dimethyldodecylamine (DDA) being used as a stabilization agent.

A tertiary amine (N,N-Dimethyldodecylamine, DDA) was added during the reaction to stabilize TeBD complexes and avoid any phase separation.

Tellurium-loaded 65% of the pure, unloaded scintillator  
 water-based wavelength shifter  
 timing profile, the intensity of scintillation light as a function of time  
 the prompt fluorescence intensity at a time  $t$  excitation be  $I = I_0 e^{-\frac{t}{\tau}}$   
 singlet and triplet states ionization density depend  $\alpha$ -particle high ionization density  
 quenching,

2 g/L PPO gives an absolute light yield of 11900 photons/MeV.  
 for the partial-fill phase, 0.5 g/L PPO gives Measurements in 0.5 g/L showed a light yield of 52% of 2 g/L, 6190 photons/MeV[67, 68].

### 3.4 Optics

Optical parameters

Winston cone

timing

attenuation

scattering

laser pulse diffuser, it can run with different wavelengths: 337, 365, 385, 420, 450 and 500 nm. The laserball

The acrylic of the AV is UV-transparent

### 3.5 Trigger and Readout of the SNO+ Detector

As mentioned in 3.1, the Hamamatsu 8-inch R1408 PMTs, as photon sensors, are the basic detection elements for the SNO+ detector.

The photons created from particle interactions in the detector propagate to the PMT sphere and may hit a certain PMT and strike on its photo-cathode, which is a thin caesium bialkali film coated on the inner surface of PMT glass. The photocathode then produces a photo-electron through photoelectric effect. The photocathode is set at ground voltage while the anode is at a high voltage ranging from +1700 to +2100 V [69, 62]. This forms electric fields inside the PMT. The photo-electron is accelerated and focused by the electric field in the PMT and goes through the volume which is under vacuum until it reaches the region of a series of secondary emission electrodes, called dynodes. The nine dynode strings are constructed in a Venetian blind configuration in R1408 PMT [69, 59]. When the photo-electron transfers its energy to the materials in dynodes, a number of secondary electrons escape and form a measurable current which is collected by the a custom-made operating circuit (PMT base) at the anode [70].

19 crates  $\times$  16 Front End Cards (FEC)  $\times$  32 channels = 9728 electronics channels.

The PMT hit time of

Once the global trigger signal is issued, the integrated charges and time from an event are stored in each channel.

[71, 72]

Each crate processes  $16 \times 32 = 512$  PMTs. 9605 channels are actually used and among them, 32 channels are reserved for calibration devices and labelled as FEC Diagnose (FECD) channels

During the experiment running, the maintenance of the electronics is always ongoing.

crate controller card (XL3)

analog master trigger system (MTC/A+) ("+" means an upgrade to SNO MTC/A)

digital master trigger system (MTC/D)

the analog waveforms are summed on the MTC/A+ card, then they are digitized

CAEN v1720 digitizer

TUBii trigger utility board pulsers and delays

DAQ

nearline provides a real-time analysis of the data quality,

trigger system PMT Interface Card (PMTIC) Front End Card (FEC)

NHit20 (N20), NHit100 (N100) trigger pulses.

MTC/A has 3 discriminators: LOW, MED and HI.

Global Trigger (GT) the timing and charge from the fired PMT is digitized and stored.

Nhit means the number of live hit PMTs in the detector for a given event.

dark noise rate is estimated to be 1 kHz.

For the SNO+ detector specifically, each PMT that triggers sends multiple trigger pulses down the electronics chain, which then performs higher logic. These include both a 93 ns long square pulse (N100) and a 48 ns square pulse (N20)

These widths are chosen to match the characteristic travel times of photons across the detector. More specifically, the N100 width is chosen such that a set of photons from a Cherenkov cone will result in overlayed PMT pulses. The shorter N20 width limits this overlaying of PMT pulses to events originating from the centre of the detector. If the total

height of either of these summed pulses passes a set threshold value, a global trigger (GT) is issued. This global trigger defines an “event” within the detector and results in all the associated information being saved. Multiple different trigger thresholds can be set. For example: N100Lo, N100Med, N100Hi are triggers based on the N100 pulses, where each has a different threshold value set. So it is possible, and likely, that an event within the detector passes several of these trigger thresholds. Additionally, the detector can trigger from the charge in the PMTs directly. The voltage pulses from all of the PMTs are summed together (ESUM). If this combined voltage trace drops below a threshold value (for example, ESUMHi, ESUMLo), this can also issue a GT to the detector. Figure 3.4 shows the event display of a typical muon event in the detector. Each individual PMT that triggered for that event is highlighted at its position on the support structure. A muon event is characterized by the large number of triggered PMTs. As with nearly all muons that pass through the detector, it is traveling in a downward direction. This is seen in Figure 3.4 as the excess of PMT charge (i.e. photons) in the bottom of the detector. As all atmospheric muons traveling upwards would be attenuated by the Earth, the small flux of upward-going muons are the result of neutrino interactions in the rock surrounding the detector [56]. Figure 3.5 shows a more typical event. The circular pattern seen is produced by the projection of the Cherenkov light cone onto the PMTs. With 24 triggered PMTs, this event is considered a high-energy event within the detector. The size of the pattern indicates that this event took place closer to the PMTs traveling in an outward direction, specifically in the water between the acrylic sphere and the PMTs.

will cause an electrical signal in the form of a voltage drop. If this is larger than a threshold value, the electronics of that PMT sends a trigger pulse.

The SNO+ electronics system includes trigger and readout systems, which record the time and charge information of PMT signals. The system can measure signals with a nanosecond-level timing resolution and single-photon level charge resolution and handle a rate of several kHz for normal operations.

Charged particles within the SNO+ detector are detected through the light that they

produce. For the water phase of the experiment, the detector measures Cherenkov light using PMTs. A photon incident on a PMT may strike its photocathode and produce a photoelectron. This photoelectron, after passing through the PMTs dynode chain,

burst from supernova

PMTs are Hamamatsu model R1408.

a single RG59/U type  $75 \Omega$  coaxial cable

cables bundle into groups

connected to the Paddle Cards, PMT Interface Card (PMTIC) [73]

### 3.6 Calibration

Two kinds of calibration sources are used by SNO+: optical sources and radioactive sources. The optical sources are used to calibrate the PMT response and to measure the optical properties of the

The radioactive sources are used to calibrate the energy

reconstruction performances and uncertainties. particle identifications

Calibration sources with known physics parameters: help to understand the detector response to the events and to make accurate measurements Two types of SNO+ calibration sources: optical sources and radioactive sources Optical sources: phototube response, optical properties of the detector media Radioactive source: energy scale, resolution, systematic uncertainties  $^{16}\text{N}$  calibration source is one of the radioactive sources

Americium Beryllium (AmBe) calibration source

Optical calibration *in-situ*

- Timing module for the Embedded LED Light Injection Entity (TELLIE)

light-emitting diode (LED)

time calibration, time response

a precision of  $\mathcal{O}(1 \text{ ns})$

Blinky fibre optics nailed to the PSUP to calibrate stuff.

- 
- 

The  $^{16}\text{N}$  source  $^3\text{H}(p, \gamma)^4\text{He}$  reaction.

the SNO+ Source Manipulator System (SMS) is inherited from the SNO.

A Umbilical Retrieval Mechanism (URM) is used to send the source down to the inner vessel.

The sources are connected to the umbilical.

An umbilical encloses electrical cables, optical fibres and gas lines connected to the source.

A Universal Interface (UI) connecting the URM and the detector, Therefore, sealed environment, which ensures radon gas not leaking into the detector when deploying the source.

In the scintillator and Te-loaded phases, three additional  $\gamma$  sources:  $^{48}\text{Sc}$ ,  $^{137}\text{Cs}$  and  $^{57}\text{Co}$  will be implemented.

$^{46}\text{Sc}$  source

### 3.7 Monte Carlo Simulation and the RAT Software

The SNO+ collaboration has developed a software framework, called the Reactor Analysis Tool (RAT), which integrates a Monte Carlo simulation of the SNO+ detector and event-based analysis tools (for online and offline event analysis) since the beginning of the program. This software was originally developed by Stan Seibert for Braidwood Collaboration for a generic KamLAND like detector. It is also used by the other astroparticle physics experiments, such as DEAP/CLEAN, CLEAR and potentially for Darkside-50[74].

Geant4 Toolkit and incorporates ROOT libraries for data handling and analysis.

The RAT Monte Carlo was originally developed for the Braidwood Collaboration utilising software developed for a generic KamLAND like detector, called Generic Liquid Scintillator GEANT4 simulation (GLG4). It was branched and developed into the specialist

SNO+ version, starting in 2006/2007.

GLG4sim

Braidwood

combines both Monte Carlo simulation of the Braidwood detector with event-based analysis tasks, like reconstruction. The primary goals are:

Make it easy to analyze Monte Carlo-generated events as well as data from disk using the same software with only a few command changes. Even in the proposal R&D phase, where there is no real data, this is still useful for dumping Monte Carlo events to disk to be analyzed by another job. When there is real data, being able to do the analysis with the same code path as was used on Monte Carlo is very reassuring. Allow for a modular, user-controlled analysis of events. This includes allowing the user to selected which analysis tasks to perform (different fitters, pruning unneeded data from the event data structure, etc.). It should also be relatively straightforward for users to introduce their own code into the analysis process. Separate analysis into small tasks which can be developed asynchronously by different people, yet integrated with minimal (or perhaps zero) pain. Integrate into existing GEANT4 and GLG4sim efforts with a minimum of code duplication. As much as possible, RAT should be designed incorporate upgrades of these packages just by relinking. No cut and paste of code (mainly a question with GLG4sim). Design

the detailed processes of data acquisition and trigger systems are [53].

[75]

## Chapter 4

# Event Reconstruction

### 4.1 An Overview for the Reconstruction Algorithms in SNO+

An event happens in the SNO+ detector can produce Cherenkov photons or scintillation photons and these photons propagate through the detector and finally reach the PMTs and are detected.

to determine the vertex (position and time), direction and energy of an event.

The event vertex are evaluated by the timing parameter of the photon propagation.

The

energy of

Multi-site or multi-vertex reconstruction algorithm is being developed.

In this chapter, we do not consider the case of multi-vertex.

### 4.2 Multi-path Vertex Reconstruction Algorithm for SNO+

A Multi-path (MP) reconstruction framework was developed by the University of Alberta group as an additional vertex reconstruction algorithm for SNO+. This framework was first developed by Aksel Hallin to reconstruct and investigate the event vertex for the data taken from an early stage of SNO+ when the detector was partially filled with water at the end of 2014 (partial water fill stage)[76]. This Multi-path partial water fitter was further

developed by David Auty and Kalpana Singh for investigating the wavelength shifter and water events[77, 78, 79, 80]. Jeff Tseng restructured the framework into more flexible and efficient C++ codes and implemented into the RAT software[81].

In this framework, the fitter is able to be adapted for various SNO+ physics phases, including the water phase, the conceptual wavelength shifter (WLS) phase, the partial-fill phase and the scintillator phase (with and without loading tellurium). In the SNO+ water phase, the cavity and the AV are both filled with ultra-pure water. This is a relatively simple geometry since everything inside the PSUP can be simplified as water. Therefore, we start with the MP water fitter (the MPW fitter) to explain the reconstruction concepts.

The MPW fitter fits for position, time and direction of a triggered event in SNO+ water phase. First, the fitter throws a random position built up by random variables which are uniformly distributed inside a sphere with a radius of 10 *meters* (larger than the actual PSUP radius  $r_{PSUP} = 8.39\text{ m}$ ). Meanwhile, a random event time is also generated, following a uniform distribution in a range of 100 to 300 *ns*. The Class Library for High Energy Physics (CLHEP) is used for creating pseudo-random numbers (see the Appendix A.1 for details). The random position and the random time are combined to form a random event vertex, which is set as the trial event vertex.

For a triggered event, photons are produced around the event position and propagate to the PMTs. In a simplified situation neglecting reflection and refraction, these photons propagate along straight line. Connecting the trial event vertex to the triggered PMTs, the fitter evaluates a timing parameter, called the time residual ( $t_{res}$ ), which is defined as:

$$t_{res} = t_{PMT} - t_{transit} - t_{event}, \quad (4.1)$$

where  $t_{PMT}$  is the PMT trigger time recorded by the detector,  $t_{event}$  is the time when an event occurs (event time), and  $t_{transit}$  is the total transit time (or time of flight, *TOF*) taken by a photon travelling from the event position ( $\vec{x}_{event}$ ) to the triggered PMT ( $\vec{x}_{PMT}$ ) and crossing different materials in the detector.

To calculate the  $t_{transit}$ , the fitter uses photons from prompt time window (prompt light) and assumes that photons propagate in straight lines (straight light paths). The simple

straight light path calculation gives  $t_{transit} = |\vec{x}_{event} - \vec{x}_{PMT}|/v_{water}$ . Detailed calculations, such as refraction and reflection when the lights cross different detector materials, absorption and scattering from the materials, as well as the lensing effects caused by the spherical structure of the acrylic vessel, are neglected. We found that without these details, the fitter can still produce decent results that are consistent with the ones using detailed calculations.

For a trial vertex  $(\vec{x}_0, t_0)$ , the fitter calculates a set of  $t_{res}$  values with respect to all the triggered PMTs. These values are fed into a likelihood function:

$$\ln \mathcal{L}(\vec{x}_0, t_0) = \sum_{i=1}^{\text{Nhits}} \ln P(t_{res}^i), \quad (4.2)$$

where  $t_{res}^i$  is the time residual calculated from the  $i^{th}$  triggered PMT and Nhits here stands for the number of total triggered PMTs by an event.

A pre-set 1-dimensional (1D) probability density function (PDF) is used for fitting the model. The pdf was taken from the bench-top timing profile measurement as well as the measured detector response.

$P(t_{res}^i)$  is the probability returned from the PDF for the  $i^{th}$  triggered PMT and a trial event vertex.

The Levenberg-Marquardt method, which is commonly used for fitting the nonlinear model for multiple parameters, is used as an optimizer to find the best fit event parameters (position, time and direction). Appendix A.2 describes this method; A.3 describes the implementation of the method to the MultiPath fitter framework. Also see [82, 1].

As we will see in the following sections, one of the main tasks for the fitter is to calculate the  $t_{transit}$  by evaluating light paths. In the water phase, we consider photons created in an event travelling along straight line paths and the paths are always in water. In the other situations, for example, when the acrylic vessel is filled with the wavelength shifter or scintillator, the light path calculations will be modified.

Fig. 4.1 shows the reconstruction concepts for position and direction.

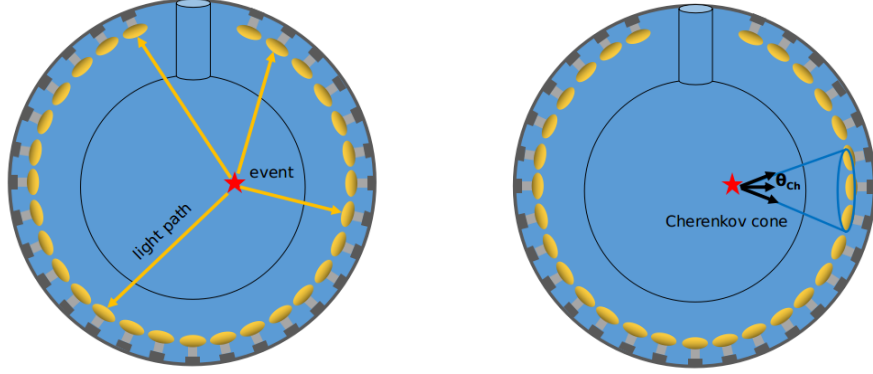


Figure 4.1: Diagrams of position (left) and direction (right) reconstruction in SNO+ water phase.

### 4.3 MPW Position and Direction Reconstructions

#### 4.3.1 Vertex Reconstruction

For the position reconstruction of the MPW fitter, the likelihood function simply calculates the likelihood assuming straight line paths of prompt light from a position vertex  $\vec{X}_0$  (fVertex) and a starting time offset  $t_0$  to each of the hit PMTs.

We define the position difference  $\vec{X}_{\text{diffCh}} = \vec{X}_0 - \vec{X}_{\text{pmt}}$ , then the time of flight for prompt light is  $t_{\text{Ch}} = |\vec{X}_{\text{diffCh}}|/v_g$  and  $L_{\text{Ch}} = L(t_{\text{Ch}})$ .

The derivatives of the likelihood function can be calculated from explicit mathematical forms as:

$$\frac{\partial L}{\partial t_0} = \frac{dL_{\text{Ch}}}{dt_{\text{Ch}}},$$

$$\frac{\partial L}{\partial x} = \frac{\partial L_{\text{Ch}}}{\partial t_{\text{Ch}}} \frac{dt_{\text{Ch}}}{\partial x} = -\frac{dL_{\text{Ch}}}{dt_{\text{Ch}}} \frac{X_{\text{diffCh}}}{|\vec{X}_{\text{diffCh}}| \cdot v_g},$$

$$\frac{\partial L}{\partial y} = -\frac{dL_{\text{Ch}}}{dt_{\text{Ch}}} \frac{Y_{\text{diffCh}}}{|\vec{X}_{\text{diffCh}}| \cdot v_g},$$

$$\frac{\partial L}{\partial z} = -\frac{dL_{\text{Ch}}}{dt_{\text{Ch}}} \frac{Z_{\text{diffCh}}}{|\vec{X}_{\text{diffCh}}| \cdot v_g},$$

where  $\frac{dL_{\text{Ch}}}{dt_{\text{Ch}}}$  can be calculated numerically from the timing pdf.

In the WaterPosition class, it starts with a random  $(\vec{x}_0, t_0)$  as seed and calculates the likelihoods and their derivatives for various paths. These values are sent to the Multi-path Fitter, which is fitting 4 parameters:  $x, y, z, t$  and to maximize the likelihood function through the MRQ method and to find the best-fit positions.

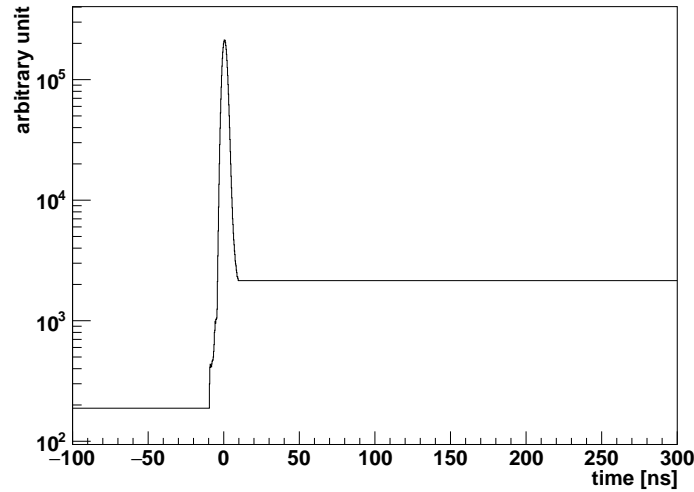


Figure 4.2: PMT response time as the timing pdf for vertex reconstruction.

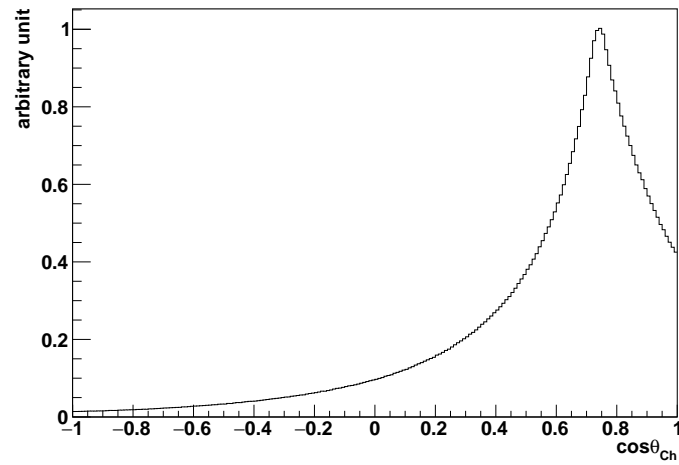


Figure 4.3: PMT angular distribution as the angular response pdf for direction reconstruction.

### 4.3.2 Direction Reconstruction

$\vec{u}_0 = (\cos \phi \sin \theta, \sin \phi \sin \theta, \cos \theta)$  (fDirection), where the  $\theta$  is zenith angle and  $\phi$  the azimuth.  $\cos \theta_{\text{Ch}}$  is the angle between  $\vec{u}_0$  and  $\vec{X}_{\text{diffCh}}$ , which is taken as the fitting parameter of the likelihood function for the direction reconstruction. For the i-th hit PMT,  $\cos \theta_{\text{Ch}}^i = \vec{u}_0 \cdot \frac{\vec{X}_{\text{diffCh}}^i}{|\vec{X}_{\text{diffCh}}^i|}$ , then the likelihood function is:

$$L(\vec{u}_0) = \sum_{i=1}^{\text{Nhits}} L_i(\cos \theta_{\text{Ch}}^i),$$

The derivatives have explicit mathematical forms:

$$\frac{\partial L}{\partial \theta} = \frac{dL_{\text{Ch}}}{d \cos \theta_{\text{Ch}}} \frac{d \cos \theta_{\text{Ch}}}{d \theta} = \frac{dL_{\text{Ch}}}{d \cos \theta_{\text{Ch}}} \frac{d \vec{u}_0}{d \theta} \cdot \frac{\vec{X}_{\text{diffCh}}}{|\vec{X}_{\text{diffCh}}|},$$

where  $d \vec{u}_0 / d \theta = (\cos \phi \cos \theta, \sin \phi \cos \theta, -\sin \theta)$  and

$$\frac{\partial L}{\partial \phi} = \frac{dL_{\text{Ch}}}{d \cos \theta_{\text{Ch}}} \frac{d \cos \theta_{\text{Ch}}}{d \phi} = \frac{dL_{\text{Ch}}}{d \cos \theta_{\text{Ch}}} \frac{d \vec{u}_0}{d \phi} \cdot \frac{\vec{X}_{\text{diffCh}}}{|\vec{X}_{\text{diffCh}}|},$$

where  $d \vec{u}_0 / d \phi = (-\sin \phi \sin \theta, \cos \phi \sin \theta, 0)$ .  $\frac{dL_{\text{Ch}}}{d \cos \theta_{\text{Ch}}}$  can be calculated numerically from the PMT angular response pdf.

In the FitterWaterDirection class, it starts with a random  $(\theta_0, \phi_0)$  as seed and calculates the likelihoods and their derivatives for various paths. These values are sent to the Multi-path Fitter, which is now fitting 2 parameters:  $(\theta, \phi)$  and to maximize the likelihood function through the MRQ method and to find the best-fit directions.

## 4.4 Effective Group Velocity

When photons travel through the detector, their group velocities change with different refractive indices of different detector materials. The group velocities also depend on the wavelengths of the photons as  $v_g = c/n(\lambda)$ . Fig .4.4 shows the measured refractive indices as a function of wavelength, obtained from the measurements of laserball scans in the SNO+ water phase[5]. Furthermore, the group velocities can change when these photons are scattered, absorbed, refracted and reflected. To simplify these complicated situations

for the reconstruction, an averaged value of the group velocity is used in the straight line light path calculation. This fixed group velocity is considered as an effective value.

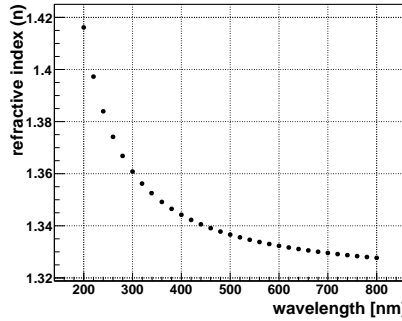


Figure 4.4: Refractive index vs wavelength. These values are based on the measurements from laserball calibration scans in the SNO+ water phase[5].

A reasonable selection of this value is required, since the value can introduce biases in the fitted position. This kind of bias is mainly due to a “complementary” effect of the fitter. As mentioned in section 4.2, the water vertex fitter calculates the  $t_{transit}$  by evaluating the distances from the trial vertex to the triggered PMTs:  $t_{transit} = |\vec{x}_{event} - \vec{x}_{PMT}|/v_{water}$ . If the value of the group velocity  $v_{water}$  is set large (or fast speed), the value of  $t_{transit}$  will decrease, and the corresponding value of  $t_{res}$  will increase according to the definition of  $t_{res}$ (4.1). These calculated  $t_{res}$  value is compared to the time pdf for the fitting. If  $t_{res}$  is larger than the expected value, the fitter will place the trial vertex away from the hit PMTs to increase the  $t_{transit}$  and then decrease the  $t_{res}$ , as illustrated in Fig. 4.5. On the other hand, if  $v_{water}$  is set small (or slow speed),  $t_{transit}$  increases and  $t_{res}$  decreases, and the fitter will place the trial vertex closer towards the hit PMTs. Therefore, an overestimated group velocity (too fast) brings a positive radial bias to the true event position while an underestimated one (too slow) brings a negative radial bias.

In practice, the effective group velocity is tuned by an effective refractive index  $n_{eff}$  (or called *RI* value):  $v_{water} = c/n_{eff}$ . To select a reasonable effective group velocity for the water-phase vertex fitter, my first approach is to test on all the values of the refractive index provided by the SNO+ laserball measurements. The values are listed in Fig. 4.4.

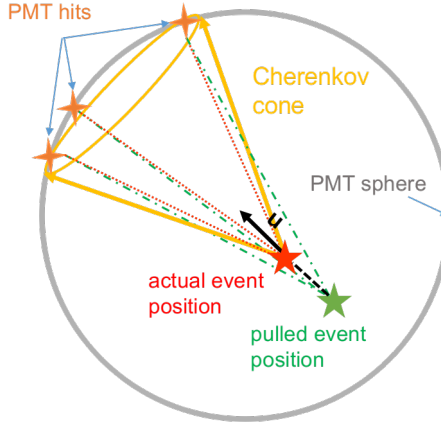


Figure 4.5: A cartoon shows effects of tuning the effective group velocity. In this case, the effective group velocity is faster than expected, the fitted position is dragged back along the direction to increase the time of flight.

I choose the one which gives the smallest radial bias based on MC simulations. For typical 5 MeV  $e^-$  events simulated uniformly inside the AV and isotropic momentum,

As shown in Fig. ??,  $n_{eff} = 1.40$  gives the smallest radial bias and is adopt for the MC case.

Later I turned to a more data-driven approach rather than just tuning from the simulations. This approach is to extract an average group velocity by analyzing the  $^{16}\text{N}$  calibration source data.

as shown in Fig. 4.6.

For a more precise approach, a set of laserball calibration runs which to measure actual group velocities in the SNO+ water detector[83].

For the scintillator and partial-fill phase vertex fitters, I adopt a linear interpolation method described in [84], which will be discussed in section 4.6.

#### 4.4.1 Fitter Pull and Drive Correction

An effect of “fitter pull” in the event vertex reconstruction utilizing the Cherenkov light was observed in the SNO experiment. The distribution of  $(\vec{x}_{fit} - \vec{x}_{mc}) / |\vec{x}_{fit} - \vec{x}_{mc}| \cdot \vec{u}$  shows a large peak at +1, which indicates that the fitted position  $\vec{x}$  is prone to be pulled forward

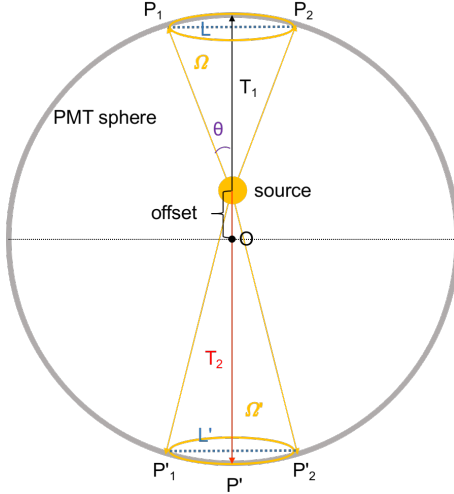


Figure 4.6:  $^{16}\text{N}$  central run.

from the true position systematically along the event direction  $\vec{u}$ [7, 6, 84].

In the SNO+ water detection medium (or the SNO heavy water), Cherenkov photons created by an event trigger most of the PMT hits with early timing and these hits are located within the Cherenkov cone; for the same event, there are also a few triggered PMT hits with later timing. These PMT hits can be caused by the scattered or reflected photons and they are located throughout the detector. For a random PMT hit, it is more probable to be placed outside the Cherenkov cone due to the geometry: consider an event happens at the center of the PSUP, the Cherenkov cone it produced will intersect the PSUP by an area of  $2\pi R_{PSUP}^2(1 - \cos 41^\circ)$ , which occupies about 12% of the total area of the PSUP sphere. Therefore, for a random PMT hit on the PSUP sphere, it has more than 88% of chance to be placed outside the Cherenkov cone.

For these later timing PMT hits, a similar ‘‘complementary’’ effect mentioned in 4.4 can also happen. When the fitter fits with  $t_{res}$ , for the large  $t_{res}$  values caused by the later timing hits, it pulls the trial position away from the later timing hits to increase  $t_{transit}$  and decrease  $t_{res}$ , as illustrated in Fig. 4.7. This effect was also explained as ‘‘straighten out delayed photons’’ by the timing fitter in [7]. Furthermore, the major early hits can also cause small  $t_{res}$  values and thus the fitter pulls the trial position closer towards the early

hits to decrease  $t_{transit}$  and increase  $t_{res}$ . Recall that the early hits are located on or around the Cherenkov cone, therefore an overall effect of this “fitter pull” is that the fitted position will be pulled along the axis of the Cherenkov cone and towards the PSUP sphere. This pull direction is coincident with the event direction.

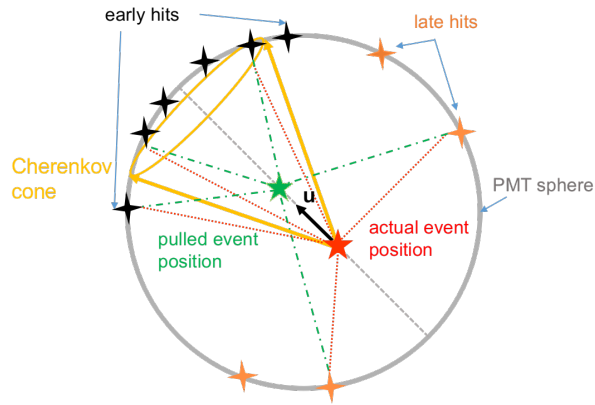


Figure 4.7: A cartoon shows fitter pull effect, modified from Fig. C.2 in [6] and Fig. 2,3,4 in [7].

A simple way to eliminate this “fitter pull” effect is to pull back the fitted event position against the event direction. This is called “drive correction”.

Once the MPW fitter obtains both of the fitted position and direction, the drive correction is applied on the fitted position by  $\vec{X}_{\text{corrected}} = p_0 \vec{X}_{\text{fit}} + p_1 \vec{u}_{\text{fit}}$ , where  $p_0$  and  $p_1$  are the correction parameters, as shown in Fig. 4.8.

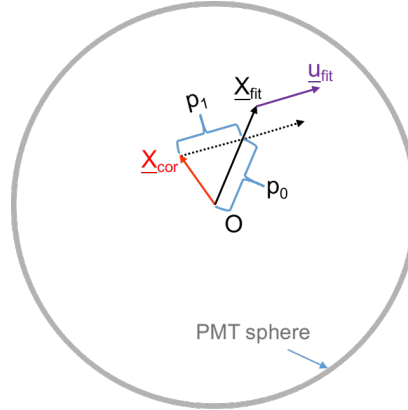


Figure 4.8: A diagram illustrates the drive correction.

To obtain the values of  $p_0$  and  $p_1$ , I generated electron events distributed isotropically inside the AV. The simulations of 2, 3, 4, ..., 10 MeV electrons are produced. Then the MPW fitter is applied on each simulations and returns the results of  $\vec{X}_{fit}$  and  $\vec{u}_{fit}$ . Take the Monte Carlo generated positions  $\vec{X}_{MC}$  as the true positions, for all the fitted events, a  $\chi^2$  function is calculated by:

$$\chi^2 = \sum_{i=1}^{N_{\text{events}}} [\vec{X}_{MC}^i - (p_0 \vec{X}_{fit}^i + p_1 \vec{u}_{fit}^i)]^2$$

The  $p_0$  and  $p_1$  are obtained by minimizing the  $\chi^2$  function. When calculating the  $\chi^2$ , the fitted events of  $|\vec{X}_{fit} - \vec{X}_{MC}| > 3$  m are thrown away to improve the  $\chi^2$  minimization results.

For the 2 to 10 MeV electrons simulations, the obtained values of  $p_0$  and  $p_1$  are energy or Nhit dependent. However, it does not improve the results if using the Nhit dependent functions  $p_0(Nhit)$  and  $p_1(Nhit)$  as drive corrections. Finally we take the average values from the 5 to 10 MeV electrons simulations and the drive correction is set as  $\vec{X}_{\text{corrected}} = 0.995765 \vec{X}_{fit} + -63.826 \vec{u}_{fit}$ .

It is important to note that since the drive correction parameters are obtained from the reconstructions of Monte Carlo, it depends on the Monte Carlo and the results of reconstruction. Therefore, the  $n_{water}$ , mode cut and time residue cut affecting the fitted results will also affect the drive correction parameters, but not significantly.

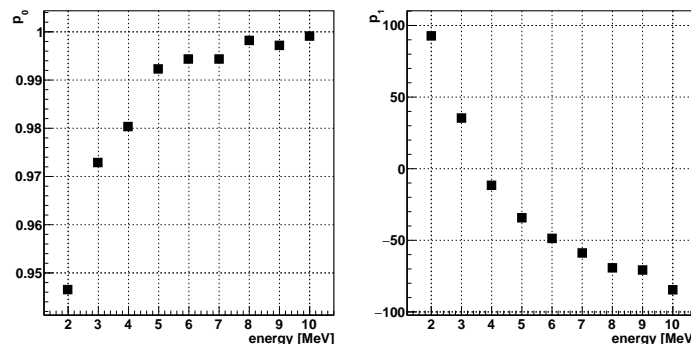


Figure 4.9: Drive correction parameter  $p_0$ ,  $p_1$  vs energy.

Electron events with various energies were generated at the detector center and their

momentum were along +x direction.

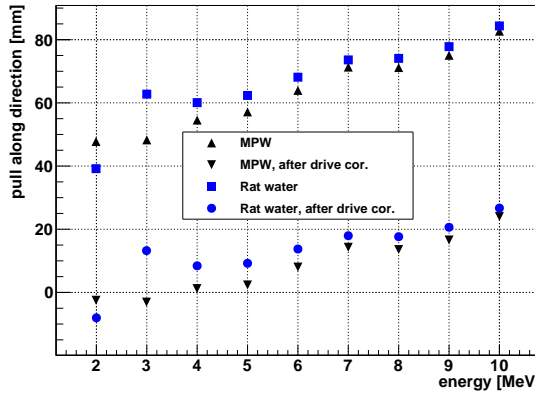


Figure 4.10: Radial biases of simulated electron events before and after the drive correction, as a function of energy.

By fitting the simulations of 5 MeV electrons generated at the detector center and travelling along +x direction, the drive effect of the MPW fitter causes a  $\sim 50$  mm biases from the detector center along +x axis. The drive correction reduces this drive bias down to  $\sim 0.2$  mm. For the reconstruction of  $^{16}\text{N}$  data, the drive correction can reduce the fitted position RMS by  $\sim 20$  mm.

#### 4.4.2 Multi-path Fitter Structure

The Multi-path fitter has already been implemented into the RAT software and being used in data processing and analyzing.

The MP fitter structure consists of:

- Fitter database

This database provides parameters used by the fitter, including the physics constants, detector geometry parameters, fit parameters and pdfs. The database is in a JSON format[85] and contains multiple tables tagged by indices to indicate different detection media or physics phases. In each table, there are fit parameters and pdfs optimized for the specific scintillator. For example, for the partial-fill phase with a PPO

concentration of 0.5 g/L, the fitter will look for the index of “labppo\_0p5\_scintillator” and extract the pdfs and fit parameters under that index.

The fit parameters includes the fitter tolerance and the maximum iterations which determine how the fitter converges,

Reflective index (water\_RI, or  $n_{water}$ ), used for effective group velocity ( $v_g = c/n_{water}$ ) calculation. air refractive index (air\_RI), PSUP radius ( $r_{PSUP} = 8390\ mm$ ). Offsets boundary settings

The MPW fitter currently uses one fixed number for  $n_{water}$ , rather than a function of wavelengths. The value of  $n_{water}$  can be tuned to give the lowest biases of the fitted positions to the Monte Carlo and to give the lowest RMS of fitted results as well. But the effect of  $n_{water}$  can also be corrected by the drive correction afterwards. Currently  $n_{water} = 1.38486$  is obtained by analyzing the time of flight from the  $^{16}\text{N}$  central run-100934 data reconstructed by the MPW fitter.

time offset, position offset, radius cut x, fitting bin-width and steps.

- PMT response time (timing) pdf for the position reconstruction, as shown in Fig. 4.2. The pdf shown in red line is modified from the measured PMT response time distribution from SNO time and the late light response is forced to be de-weighted (black).

The pdf is modified in [-100,-4] ns region to match the time residual spectrum obtained from  $^{16}\text{N}$  central run-100934 (blue).

- PMT angular response pdf for the direction reconstruction, as shown in Fig. 4.3. It is taken from the Monte Carlo simulation of 5 MeV electrons traverse in the AV with one direction.

- Likelihood Calculation Classes, Constructs likelihood functions, calculates likelihoods and their derivatives. For the MPW fitter, there are two classes: WaterPosition for position reconstruction and WaterDirection for direction reconstruction. The WaterPosition class tackles with 4 parameters (x,y,z,t) and the WaterDirection class tackles with 2 parameters ( $\theta, \phi$ ).

- Multi-path Fitter

Processes the MPW fitter and finds the best-fit of the likelihood function. It is a general processor and is shared with the fitters using the Multi-path Fitter, including the MPW fitter, air-water (AW) fitter, wavelength-shifter (WLS) fitter and scint-water fitter. It processes a certain fitter by being assigned the fitter name in macro. It processes the fitter event by event: for every triggered event, it first calls PMT selectors (ModeCut or StraightTimeResidualCut) and sends the information of the reduced PMTs to a certain Likelihood Calculation Class for likelihood calculations. The Likelihood Calculation Class sends back the values of likelihoods and their derivatives, so the Multi-path Fitter does not care about how the likelihood functions are constructed and how the likelihoods and derivatives are calculated. Using these values, it constructs an  $n \times n$  Hessian matrix ( $n$  is the number of fitting parameters defined in Likelihood Calculation Class) and uses the Levenberg-Marquardt (MRQ) method to maximize the likelihood and finds the best-fit values. For the MPW, if the likelihood maxima is found 5 times for any position and direction then values are returned as the fitted position and direction. For the MPW case, it calls the ModeCut and fits for the position and time; then it calls the StraightTimeResidualCut and fits for the directions.

- Dump Likelihood

This is a function inside the Multi-path Fitter. It stores the likelihood surfaces and derivatives with respect to arrays of trial vertices of the interested events which are designated by event GTIDs in the database. From the likelihood surfaces and derivatives of an interested event, people can evaluate the fit performance of that event by checking whether the fitter finds global or local maximum.

- SDecompQRH

This is a fit method class modified from ROOT TDecompQRH class[86]. It is used by the Multi-path fitter to invert the Hessian matrix through QR decomposition

method[?]. Compared to ROOT, `Solve()` for  $Ax=b$  is modified to zero the component of  $x$  for which the diagonal element in  $R$  is small. This allows a Levenberg-Marquardt optimization to continue in many cases when the matrix is singular. For the MPW case, it is used to invert a  $4\times 4$  matrix of the WaterPosition Class while the inversion of  $2\times 2$  matrix of the WaterDirection is calculated directly[87].

- PMT selectors

Detailed descriptions are shown in section 4.9.

## 4.5 Vertex and Direction Reconstruction for Water-based Wavelength-shifter

X. Dai et al.[88] made a proposal for adding wavelength shifters (WLS) into a water Cherenkov detector like SNO. Compared to the water Cherenkov detector, a water-based wavelength shifter (wbWLS) detector has a higher light yield (about threefold higher than SNO[88]) and thus lowers down the energy threshold and opens opportunity to detect low energy events. At the meantime, it will still keep the directionality from Cherenkov signals compared to a loss of the directionality for the liquid scintillator detector, which can be used to suppress the backgrounds when analyzing directional signals, such as solar neutrinos. This technology is being studied by future neutrino experiments, such as the Advanced Scintillation Detector Concept (ASDC)[89], WATCHMAN experiment[90] and Jinping experiment[52].

There was a proposal of adding wavelength shifter (WLS) into the SNO+ detector in the middle of the water phase. The specific wavelength shifter we considered is PPO, which is a well-studied ingredient of the liquid scintillator used in the SNO+ scintillator phase and Te-loaded phase. Although this proposal was not adopted due to the experiment schedule, it is still worthwhile for a conceptual study of a SNO+-like detector that uses water-based wavelength shifter (wbWLS) as detection medium.

Figure 4.11 shows the position distributions of triggered PMTs for MC simulated 5 MeV

electrons travelling along  $+x$  direction in the AV. The left panel shows the case when the detector is filled with pure water while the right panel is for water plus 0.1 ppm PPO. For the same electrons, the number of triggered PMTs ( $NHit$ ) in wbWLS is about 2.4 times greater than the pure water one. Although there is extra isotropic light emitted, the Cherenkov ring can still be seen clearly, allowing reconstruction of the directionality.

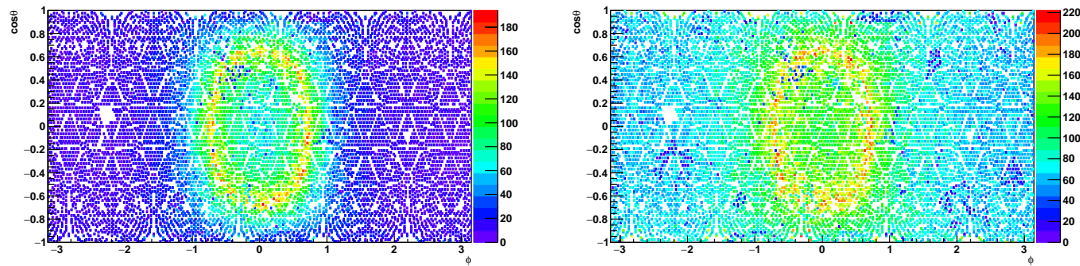


Figure 4.11: Position distributions of triggered PMTs (in zenith and azimuth angles) for 5 MeV electrons travelling along  $+x$  direction in the pure water (left) and the water plus 0.1 ppm PPO (right).

Figure 4.12 shows the energies of simulated electrons as a function of the mean value of the  $NHit$  distribution (mean nhits). In pure water, a 1 MeV electron simulation does not trigger any PMTs while in wbWLS case we have a mean nhits of 20.

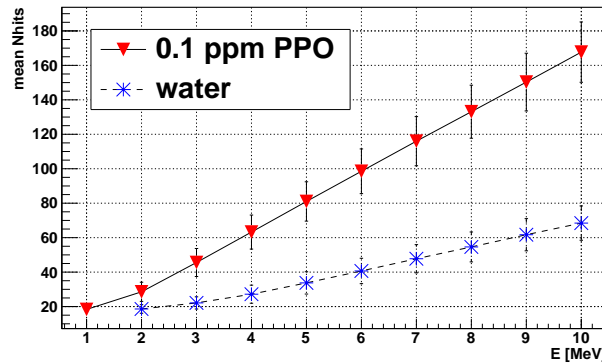


Figure 4.12: The energies of simulated electrons as a function of mean nhits. The values in the 0.1 ppm PPO (solid line with inverted triangle) are compared with the water (dashed line with star).

In the wbWLS case, since WLS absorbs and re-emits photons, the reconstruction men-

tioned in section ?? is slightly modified to build the MP WLS Fitter. According to the optical property of PPO, the prompt light emitted from an event has a probability of  $\sim 0.6$  to be absorbed by the WLS and then re-emitted at a shifted vertex along the particle direction  $\hat{n}$ . Then the fitter returns a shifted vertex,  $\vec{X}_{0,shifted} = \vec{X}_0 + \text{offset} \cdot \hat{n}$ . The offset we set in the fitter is 100 mm obtained from simulations. Figure 4.13 shows the timing pdf for the wbWLS, which is the PMT response time modified to photon propagation time in the wbWLS.

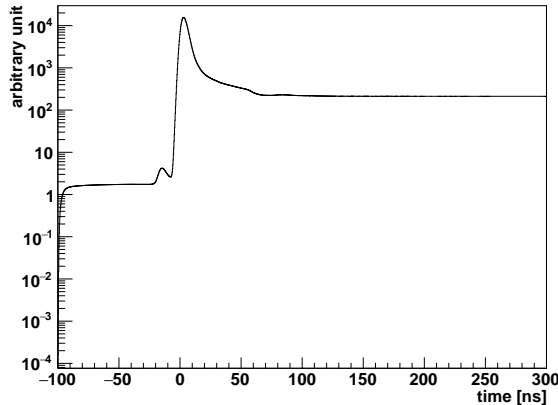


Figure 4.13: The timing pdf for the wbWLS.

To reconstruct the direction, besides the angular distribution of Cherenkov photons,  $\cos \theta_{Ch}$ , we also consider the fraction of the re-emitted and wavelength shifted photons that cause a flat angular distribution.

To test the performance of the MP WLS Fitter, 5 MeV electrons were simulated at the center of the AV filled with wbWLS and travelling along  $+x$  direction. As a comparison, the same simulation was done for the AV filled with pure water and the simulated events were reconstructed by the water fitter.

Figure 4.14 shows the performance of the WLS fitter reconstructed positions of the MC simulations compared to the pure water case. For the fit position distribution of 5 MeV electrons in the wbWLS, we get a root mean square (RMS) of 201 mm and a bias to the center (the mean of histogram) of 29 mm. Compared to the pure water case, the fit bias is

about 19 mm better and the RMS is 188 mm better.

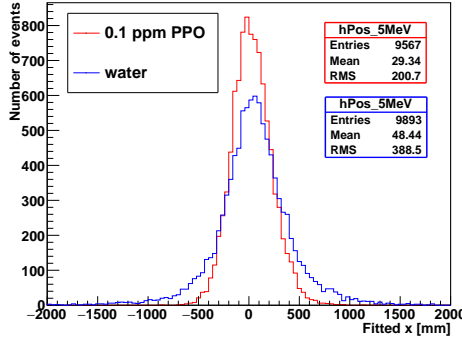


Figure 4.14: Fit position projected on x axis. The WLS fitter reconstructed  $x$  positions of the 5 MeV electron events in the wbWLS (red) are compared to the ones in the water (blue).

For a given Cherenkov event, the error in the reconstructed event direction is defined as[?]:  $\cos(\theta_e) = \vec{u}_{fit} \cdot \vec{u}_e$ , where  $\vec{u}_e$  is the simulated electron direction and  $\vec{u}_{fit}$  is the reconstructed direction. To quantify this error, we define a  $\cos \theta_a$  so that:

$$\frac{\int_{\cos \theta_a}^1 P(\cos \theta_e) d \cos \theta_e}{\int_0^1 P(\cos \theta_e) d \cos \theta_e} = a.$$

where  $P(\cos \theta_e)$  is the distribution of  $\cos \theta_e$  from MC data. The value of  $\cos \theta_a$  is found numerically to let  $\cos \theta_e$  contain  $a \cdot 100\%$  of the reconstructed data. A larger  $\cos \theta_a$  means better direction reconstruction.

Table 4.1 shows the results of  $\cos \theta_a$  for SNO heavy water data[?] and simulations for SNO+ pure water and wbWLS.

Table 4.1: A comparison of quantitative estimates for the angular resolution between the SNO heavy water, SNO+ wbWLS and the SNO+ pure water cases.

medium	$\cos \theta_{0.9}$	$\cos \theta_{0.8}$	$\cos \theta_{0.5}$
SNO heavy water	0.50	0.71	0.92
SNO+ water	0.53	0.76	0.93
wbWLS	0.37	0.63	0.90

Comparing a pure water SNO+ detector and the wbWLS one, using the MP WLS Fitter for physics events gives a better position resolution without a significant loss in the

performance of the direction reconstruction.

This fitter was tested for in [91].

## 4.6 Vertex Reconstruction for Partial-fill and Scintillator Phases

In the partial fill geometry, photons will travel with different speeds as they pass through two different media, water and scintillator. Assuming a straight light path, the MP Partial Fitter mainly calculates the total length of the light path ( $|\vec{l}_p| = |\vec{X}_{\text{PMT}} - \vec{X}_0|$ ) and separates the  $|\vec{l}_p|$  into the lengths in scintillator ( $d_{sp}$ ) and in water ( $|\vec{l}_p| - d_{sp}$ ).

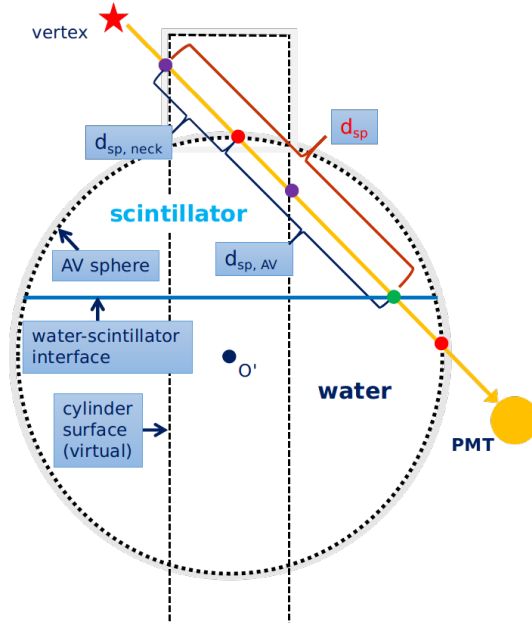


Figure 4.15: Light path calculation for the MP Partial Fitter. The light path intersects with the neck cylinder surface, the AV sphere as well as the water-scintillator interface. The total length of the path in the scintillator region (scintillator path, sp),  $d_{sp}$  is evaluated by intersection calculations.

In the partial-fill phase, the SNO+ detector can be considered as a geometry composed of the neck (cylinder), AV sphere and water-scintillator interface (plane). A ray connecting a position inside the PSUP to the PMT can intersect with these three geometries. As illustrated in Fig. 4.15, a detailed calculation of  $d_{sp}$  includes evaluations of (1) light path and neck (ray-cylinder) intersection; (2) light path and AV sphere (ray-sphere) intersection

and (3) light path and water-scintillator interface (ray-plane) intersection.  $d_{sp}$  is further separated into the path length in the neck ( $d_{sp,neck}$ ) and in the AV ( $d_{sp,AV}$ ).

For a trial position  $\vec{X}_0 = (x_0, y_0, z_0)$  and a triggered PMT position  $\vec{X}_{\text{pmt}} = (x_{\text{pmt}}, y_{\text{pmt}}, z_{\text{pmt}})$ , define a light ray (rather than a line without direction)  $\vec{l}_0 \equiv \vec{X}_0 + a \cdot \vec{u}$ , where  $a$  is the distance between vertex and intersection point and it is the parameter to be determined;  $\vec{u} = \frac{\vec{X}_{\text{pmt}} - \vec{X}_0}{|\vec{X}_{\text{pmt}} - \vec{X}_0|}$  is the direction of the light ray. It is a unit vector pointing from the  $\vec{X}_0$  to the  $\vec{X}_{\text{pmt}}$ .

In the ray-sphere intersection case (light ray passes through the AV sphere), the intersection points on the  $\vec{l}_0$  satisfy the sphere equation  $(\vec{X} - \vec{O}_{av})^2 = r_{av}^2$ , where  $\vec{O}_{av}$  is the origin of the AV sphere and  $\vec{O}_{av} = (0, 0, 108)$  mm in the PSUP coordinate. Thus the intersection equation is:  $(\vec{l}_0 - \vec{O}_{av})^2 = r_{av}^2$ .

Let  $\Delta \equiv [(\vec{X}_0 - \vec{O}_{av}) \cdot \vec{u}]^2 - (\vec{X}_0 - \vec{O}_{av})^2 + r_{av}^2$ , if  $\Delta > 0$ , solve the equation and get:

$$a_{+,-} = -(\vec{X}_0 - \vec{O}_{av}) \cdot \vec{u} \pm \sqrt{\Delta}, \text{ if } \Delta > 0.$$

In this case, both  $a_+$  and  $a_-$  exist and have different values. If  $a_+ > a_- > 0$ , the length of the path inside the sphere is  $a_+ - a_-$ , as illustrated in Fig. 4.16 (a). Due to this geometry, the event position should be outside the AV, the condition  $|\vec{X}_0| \geq r_{AV}$  is automatically met. If  $a_+ > 0 > a_-$ ,  $a_-$  determines the intersection point along the opposite direction of the light ray. Thus the light ray actually does not pass that point (different to the line intersection with no direction). Thus the length of the path inside the sphere is  $a_+$ , as illustrated in Fig. 4.16 (b). Also, the condition  $|\vec{X}_0| < r_{AV}$  is automatically met.

If  $\Delta \leq 0$ , there is no intersection point or only one intersection point at the AV, the light ray never passes through the AV sphere, as illustrated in Fig. 4.16 (c) and (d).

For the ray-plane intersection, the z components of the intersection points on  $\vec{l}_0$  satisfy the plane equation  $z = Z_{\text{split}}$ , where  $Z_{\text{split}}$  is the water level, i.e., the z position of the water-scintillator intersection. Thus the intersection equation is:  $l_{0,z} = Z_{\text{split}}$ , where  $l_{0,z} = z_0 + a \cdot u_z$ .

If  $u_z = z_{\text{pmt}} - z_0 = 0$ , the ray is parallel to the plane and never intersects the plane.

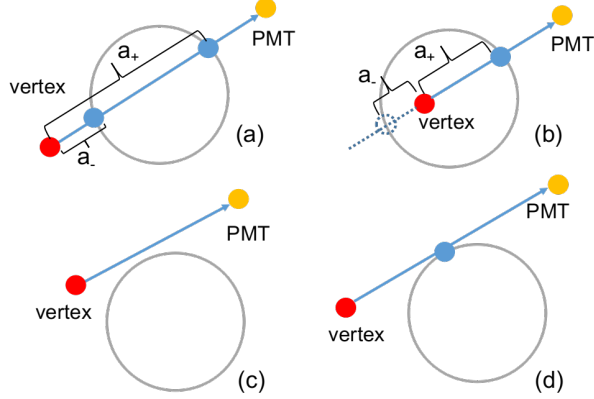


Figure 4.16: Line-sphere intersections. (a): the light ray intersects the sphere with 2 points; (b): the light ray intersects the sphere with 1 point; (c) and (d): the light ray never passes through the sphere.

If  $u_z \neq 0$ , solve the equation, we have:  $a = (Z_{\text{split}} - z_0)/u_z = (Z_{\text{split}} - z_0)$ . Let:

$$a_3 \equiv a = \frac{(Z_{\text{split}} - z_0)|\vec{X}_{\text{pmt}} - \vec{X}_0|}{z_{\text{pmt}} - z_0} \quad (\text{if } z_{\text{pmt}} - z_0 \neq 0).$$

Similar to the case of ray-sphere intersection, if  $a_3 < 0$ , the ray-plane intersection point is on the extended line along the opposite direction to the ray;  $a_3 \geq 0$  ensures the ray hits the interface. Note that here we consider the plane is infinitely large. Later we will combine with the calculations of the other geometries to cut it off.

For the ray-cylinder intersection, the x and y components of the intersection points on the  $\vec{l}_0$  satisfy the intersection equation:  $l_{0,x}^2 + l_{0,y}^2 = r_{\text{neck}}^2$ , where  $r_{\text{neck}}$  is the radius of the neck cylinder ( $r_{\text{neck}} = 785 \text{ mm}$ ).

To solve the equation, let:

$$\Delta' \equiv [x_0 \cdot (x_{\text{PMT}} - x_0) + y_0 \cdot (y_{\text{PMT}} - y_0)]^2 - (x_0^2 + y_0^2 - r_{\text{neck}}^2) \cdot [(x_{\text{PMT}} - x_0)^2 + (y_{\text{PMT}} - y_0)^2],$$

and we get:

$$a'_\pm = |\vec{X}_{\text{PMT}} - \vec{X}_0| \cdot \frac{-[x_0 \cdot (x_{\text{PMT}} - x_0) + y_0 \cdot (y_{\text{PMT}} - y_0)] \pm \sqrt{\Delta'}}{(x_{\text{PMT}} - x_0)^2 + (y_{\text{PMT}} - y_0)^2}, \quad \text{if } \Delta' > 0,$$

Similar to the ray-sphere case, if  $a'_+ > a'_- > 0$ , the length of the path inside the cylinder is  $a'_+ - a'_-$ . Due to this geometry, the event position should be outside the cylinder, the condition  $(x_0^2 + y_0^2 \geq r_{\text{neck}}^2)$  is automatically met. If  $a'_+ > 0 > a'_-$ , the event position should

be inside the cylinder and the ray-vector intersects the cylinder with one point (while the other point is along the opposite direction). Thus the length of the path inside the cylinder is  $a'_+$ . If  $\Delta' \leq 0$ , the light ray never passes through the neck cylinder. Also note that here we consider the cylinder is infinitely long. This will also be cut off by the combined calculations of the other geometries. In addition, since only the neck region inside the PSUP is valid for the fitter, we should also ensure  $z < 8390 \text{ mm}$  (in PSUP coordination).

To evaluate the length of the light ray (light path) in the scintillator region ( $d_{sp}$ ), the above three geometries needs to be combined carefully. The following two procedures go through all the possible situations. First combine the evaluations of the ray-sphere and the ray-plane intersections to calculate the light path in the AV scintillator region ( $d_{sp,AV}$ ). The following algorithm shows the detailed evaluation. Each check steps are marked by number and if-conditions are marked by a, b or c.

First check the ray-sphere intersection:

If  $\Delta > 0$ ,

(step. 1a) if  $|\vec{x}_0| < r_{AV}$  (and  $a_+ > 0 > a_-$ ), check the ray-plane intersection:

(2a-a) if  $a_3 > 0$ , the ray-vector hits the interface plane:

(3a-a-a) if  $z_0 < Z_{split}$  and  $a_3 < a_+$ :  $d_{sp,AV} = a_+ - a_3$ , see Fig. 4.17 (a).

(3a-a-b) if  $z_0 \geq Z_{split}$ :

(4a-a-b-a) if  $a_3 < a_+$ :  $d_{sp,AV} = a_3$ , see Fig. 4.17 (b).

(4a-a-b-b) if  $a_3 \geq a_+$ :  $d_{sp,AV} = a_+$ , see Fig. 4.17 (c).

(2a-b) if  $a_3 \leq 0$ :

(3a-b) if  $z_0 > Z_{split}$ :  $d_{sp,AV} = a_+$ , see Fig. 4.17 (d).

(step. 1b) if  $|\vec{x}_0| \geq r_{AV}$  (and  $a_+ > a_- > 0$ ), calculate the z position of the intersection point:  $z_{\pm} = z_0 + a_{\pm} \cdot (z_{PMT} - z_0) / |\vec{X}_{PMT} - \vec{X}_0|$ :

(1-b-a) if  $z_- \geq Z_{split}$  and  $z_+ \geq Z_{split}$ :  $d_{sp,AV} = a_+ - a_-$ , see Fig. 4.17 (e).

(1-b-b) if  $z_- < Z_{split}$  and  $z_+ > Z_{split}$  and  $a_3 > 0$ :  $d_{sp,AV} = a_+ - a_3$ , see Fig. 4.17 (f).

(1-b-c) if  $z_- > Z_{split}$  and  $z_+ < Z_{split}$  and  $a_3 > 0$ :  $d_{sp,AV} = a_3 - a_-$ , see Fig. 4.17 (g).

---

Then combine the evaluations of the ray-sphere and the ray-cylinder intersections to calculate the light path in the neck scintillator region ( $d_{sp,neck}$ ) as the following:

Since the valid fit requires the events inside the PSUP sphere, only the neck region inside the PSUP (with  $6108 < z_{neck} < 8390 \text{ mm}$ ) needs to be considered. the neck path calculation is allowed to be turned off.

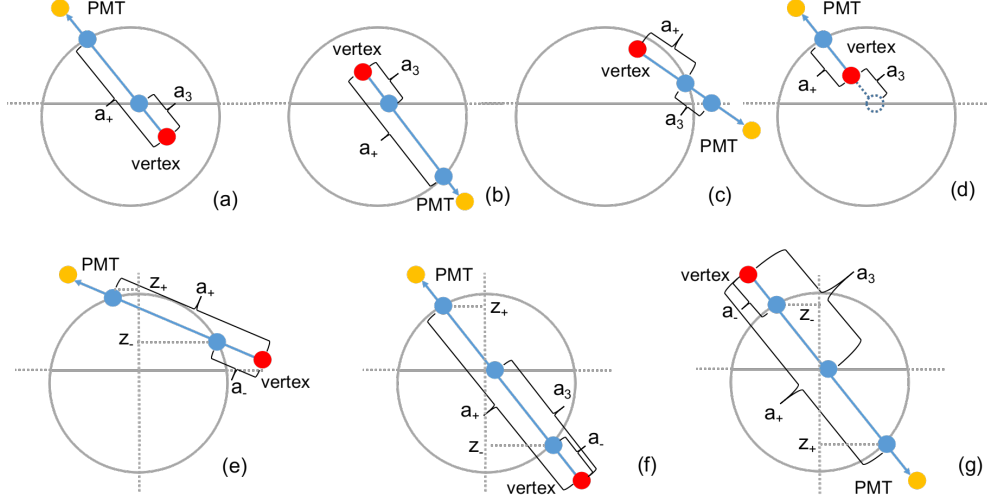


Figure 4.17: Layouts for the scintillator light paths inside the AV sphere.

---

First check the ray-cylinder intersection:

If  $\Delta_{neck} > 0$ ,

(step. 1a) if  $a'_+ a'_- < 0$  (event position is inside the cylinder), check the z position of the intersection point on neck,  $z_+ = z_0 + a'_+ u_z$ :

(2a-a) if  $6108 < z_+ < 8390$  mm (in the valid neck region), then check the AV sphere:

(3a-a-a) if  $|\vec{X}_0| \geq r_{AV}$ :  $d_{sp,neck} = a'_+$ , see Fig. 4.18 (a).

(3a-a-b) if  $|\vec{X}_0| < r_{AV}$  and  $a_+ a_- < 0$ :  $d_{sp,neck} = a'_+ - a_+$ , the light ray first hits the sphere inside the cylinder and then hits the cylinder, see Fig. 4.18 (b).

(2a-b) if  $z_+ < 6108$  mm:

(3a-b) if  $|\vec{X}_0| \geq r_{AV}$  and  $6108 < z_0 < 8390$  mm:

(4a-b) if  $a_+ > a_- > 0$ :  $d_{sp,neck} = a_-$ , see Fig. 4.18 (c).

(step. 1b) if  $a'_+ > a'_- > 0$  (event position is outside the cylinder), check the z position of the intersection point on neck,  $z'_\pm = z_0 + a'_\pm \cdot u_z$ :

(2b-a) if  $6108 < z'_\pm < 8390$  mm, check the AV intersection:

(3b-a-a) if  $a_\pm$  do not exit (never passes through AV),  $d_{sp,neck} = a'_+ - a'_-$ , see Fig. 4.18 (d).

(3b-a-b) if  $a_+ > a_- > 0$ , evaluate the z positions of the ray-sphere intersection points  $z_\pm = z_0 + a_\pm \cdot u_z$ :

(4b-a-a) if  $z_\pm \geq 6108$  mm:  $d_{sp,neck} = a'_+ - a'_- - (a_+ - a_-)$ , see Fig. 4.18 (e). The path inside the sphere is subtracted to avoid duplicated calculation.

(4b-a-b) if  $z_+ < 6108$  and  $6108 < z_- < 8390$  mm:

(5b-a-b-a) if  $a_+ > a_- > 0$ :  $d_{sp,neck} = a_- - a'_-$ , see Fig. 4.18 (f).

(5b-a-b-b) if  $z_- < 6108$  and  $6108 < z_+ < 8390$  mm:

in this case, either the event position is inside the sphere ( $a_+ a_- < 0$ ), shown in Fig. 4.18 (g), or outside the sphere ( $a_+ a_- < 0$ ), shown in Fig. 4.18 (h)), the path in neck is same:  $d_{sp,neck} = a'_+ - a_+$ .

---

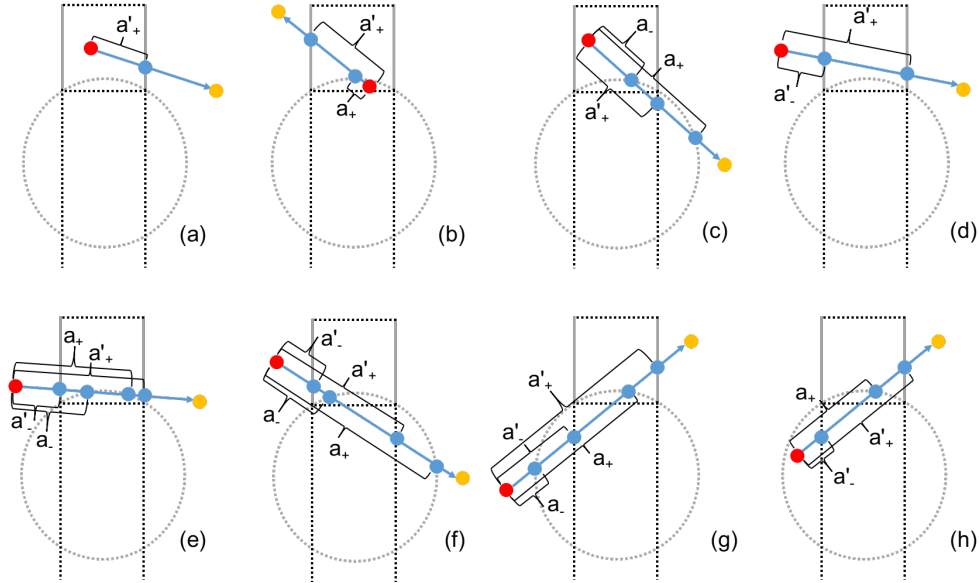


Figure 4.18: Layouts of the scintillator light paths inside the neck cylinder.

$$t_{transit} = (a_+ - a_3)/v_{gr,scint} + [|\vec{X}_{pmt} - \vec{X}_0| - (a_+ - a_3)]/v_{gr,water}$$

Once the lengths of the light path in the scintillator region or the water region are calculated, the time of flight,  $t_{transit}$  is obtained by:

$$t_{transit} = \frac{|\vec{l}_p| - d_{sp}}{v_{gr,water}} + \frac{d_{sp}}{v_{gr,scint}}, \quad (4.3)$$

and thus the time residual,  $t_{res}$  is calculated.

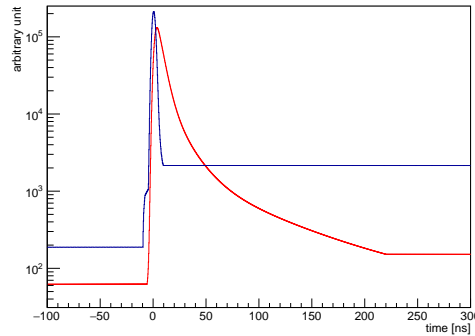


Figure 4.19: The timing pdfs used by the MP Partial Fitter. Blue: the timing pdf used by the MP Water Fitter; red: the scintillator timing pdf.

If  $d_{sp} = 0$ , the light path is always in the water. In this case, the fitter is the same as the MP Water Fitter. The fitter fits with the MP Water Fitter pdf. Once the light path passes through the scintillator region, the fitter fits with a scintillator timing pdf, the PMT time response modified to photon propagation time in scintillator, as shown in Fig. 4.19.

$$\frac{\partial L}{\partial \text{split}Z} = \frac{\partial L}{\partial \text{tof}} \cdot \frac{\partial \text{tof}}{\partial \text{split}Z} = \frac{\partial L}{\partial \text{tof}} \cdot \frac{\partial a_3}{\partial \text{split}Z}$$

$$\frac{\partial L}{\partial \text{split}Z} = 0$$

$a_1$ ,  $a_2$  and  $a_3$

The performance of the fitter was studied with MC simulations. In a partial fill geometry with water level at 4.435 m, 2.5 MeV electrons are simulated inside the AV in the scintillator region only, the water region only and the whole AV region.

Fig. 4.20 and Fig. 4.21 show the MP Partial Fitter reconstructed results for these simulations. Fig. 4.20 shows the biases between the fit positions and MC positions, projected on the x axis. The distributions of position biases are fit with Gaussian functions. The values of Gaussian mean and sigma quantify the fit biases and resolutions. Table 4.2 lists these values.

Table 4.2: Reconstructed position biases and resolutions for simulated events in partial fill.

regions of simulated events	bias (mm)	resolution (mm)
scintillator region	-1.0	73.9
water region	-10.7	385.1
full region	6.9	331.72

For the events in water, the fit bias and resolution is comparable to the water phase results in Table 5.1. The events in the scintillator region have smaller fit bias and better resolution due to more triggered PMTs in the reconstruction.

Fig. 4.21 shows the fitted  $\sqrt{x^2 + y^2}$  vs. fitted  $z$  positions. It shows that the fitter can distinguish different events in the water or scintillator region. The fitter gives reasonable results of the three different MC simulations.

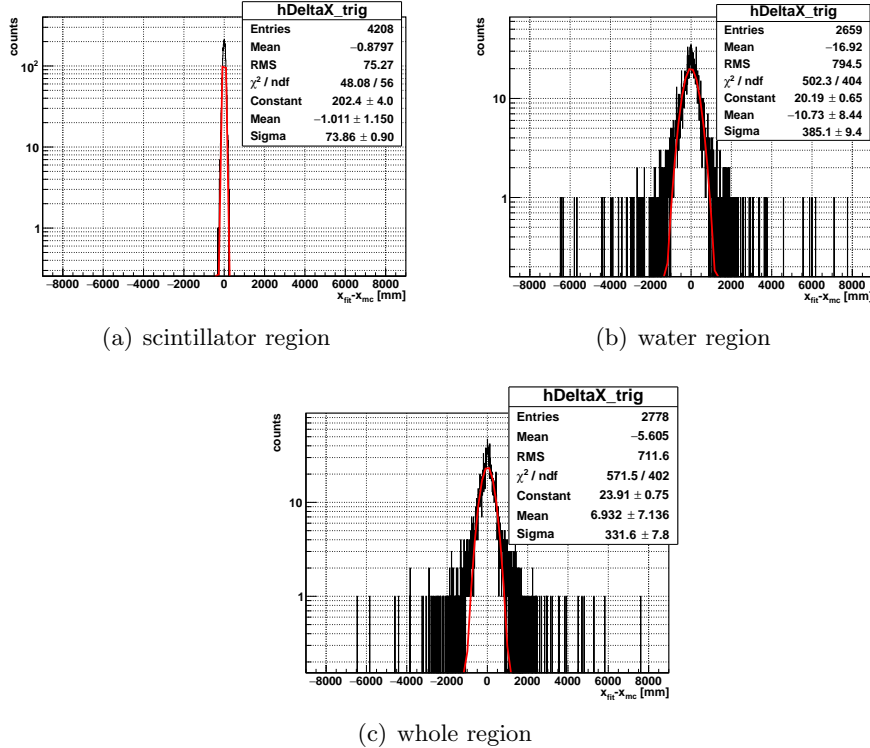


Figure 4.20: Distributions of fit position bias projected on x axis ( $x_{fit} - x_{MC}$ ).

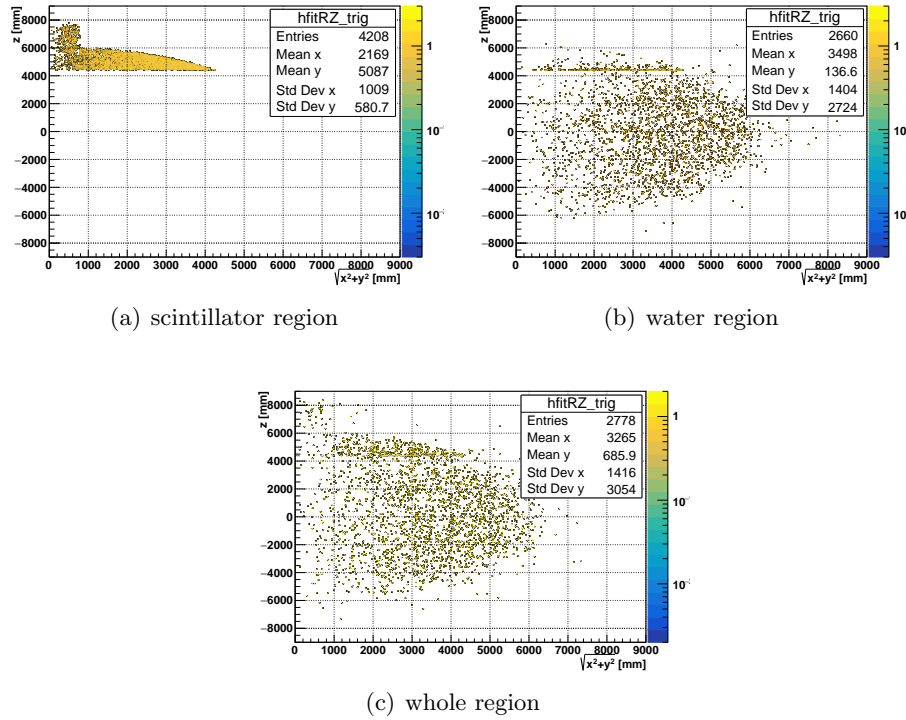


Figure 4.21: Fit results:  $\rho_{fit} = \sqrt{x_{fit}^2 + y_{fit}^2}$  vs.  $z_{fit}$ .

the optical response of the liquid scintillator empirical model. This model consists  $n$  ( $n = 3$  or 4) exponential decays with a common rise time [92].

timing profile

scintillator timing

$$\sum_{i=1}^n A_i \cdot \frac{e^{-\frac{t}{\tau_i}} - e^{-\frac{t}{\tau_{rise}}}}{\tau_i - \tau_{rise}}$$

$$\left\{ \sum_{i=1}^n A_i \cdot \frac{e^{-\frac{t}{\tau_i}} - e^{-\frac{t}{\tau_{rise}}}}{\tau_i - \tau_{rise}} * f_{PMT}(t - t') \right\} * Gaus(t, 0)$$

from bench top measurement, while the rise time,  $t_{rise} = 0.8$  ns the timing parameters  $t_i$ , amplitude  $a_i$  are determined by the benchtop measurements [].

Table 4.3: scintillator  $\alpha/\beta$  timing parameters[67, 68, 93].

scintillator particles	timing [ns]				amplitudes			
	$t_1$	$t_2$	$t_3$	$t_4$	$a_1$	$a_2$	$a_3$	$a_4$
LAB + 2g/L PPO (default scintillator)								
$e^-$	4.88	15.4	66.0	400	0.665	0.218	0.083	0.0346
$\alpha$	4.79	18.4	92.0	900	0.427	0.313	0.157	0.1027
LAB + 0.5g/L PPO (partial-fill phase)								
$e^-$	7.19	24.81	269.87	—	0.553	0.331	0.116	—
$\alpha$	6.56	23.82	224.19	—	0.574	0.311	0.115	—
LAB + 2g/L PPO + 0.5% molar concentrations DDA								
$e^-$	5.0	12.1	33.3	499.0	0.68	0.21	0.07	0.04
$\alpha$	3.8	11.3	65.3	758.0	0.48	0.32	0.14	0.06
LAB + 2g/L PPO + 0.5% molar concentrations Te+0.5% molar DDA								
$e^-$	3.7	10.0	52.0	500.0	0.72	0.23	0.02	0.03
$\alpha$	3.69	15.5	79.3	489.0	0.63	0.23	0.07	0.07

pdfs for all timing

Radial bias is defined as the difference between the fitted and true position, projected along the radial component (unit vector) of the true position [84].

$$(\vec{X}_{fit} - \vec{X}_{true}) \cdot \hat{X}_{true}$$

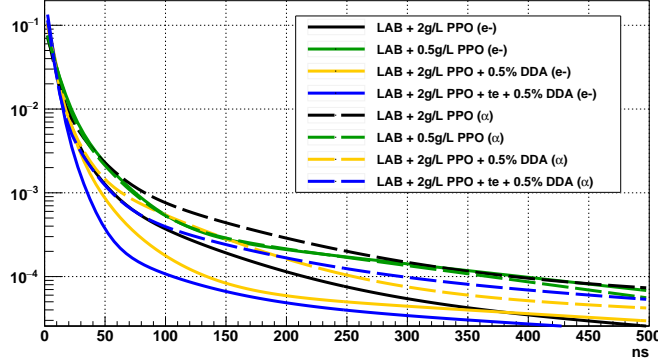


Figure 4.22: Timing profiles for liquid scintillators in different SNO+ phases.

The value of the mean radial bias is taken by fitting the histogram of the distributions of radial biases with a Gaussian profile and then get the mean of the fitted Gaussian profile.

Appendix: Levenberg-Marquardt method for fitter minimization (ref: press2007numerical)  
for M unknown parameters:  $a_0, a_1, \dots, a_{M-1}$  (for example, the 4 parameters of an event vertex:  $(x, y, z, t)$ )

The pdf can be expanded and fit with Chebyshev polynomials to obtain an analytic approximation function[1]. This analytical function can give proper analytical derivatives

The partial fitter is invulnerable to the change of pdfs caused by different PPO concentrations.

## 4.7 Energy Reconstruction

The previous sections mainly focus on vertex and direction reconstruction. For the energy reconstruction in the water phase

energy response processor, or the energy RSP fitter, is derived from SNO [94, 95].

It uses the fitted position and direction of an event as inputs and then calculates an effective

estimated  $N_\gamma$ ,

detailed detector effects are taken into account.

the asymmetric geometry of the detector, for example the neck cylinder on the top of the AV sphere; the actual number of online PMTs in a realistic physics run.

$^{16}\text{N}$  calibration scans at certain detector points.

Energy lookup table built from the simulation data set.

energy look up[96].

(energyRSP)

In the partial-fill phase, there is no proper energy fitter works. In [97], to scale  $N\text{Hits}$  based on several sets of simulations.

## 4.8 Machine Learning Algorithm

artificial neural network (ANN) Position ANN,

[98]

## 4.9 PMT Selectors for the Fitter

Several PMT selectors are used to select or remove PMTs from all the recorded PMTs triggered by an event and send the proper PMTs to the fitter for reconstruction. They are developed for optimizing the fitter or boosting up the fit speed:

- Straight Light Path Time Residual Cut Selector

This selector is used for the direction reconstruction for the SNO+ water phase. In the selector, the value of time residual ( $t_{res}$ ) is calculated for each triggered PMTs from an event and the PMT with a  $t_{res}$  value in a prompt time window of  $[-10.0, 120.0] \text{ ns}$  is selected for the fitter. The selector calculates  $t_{res}$  by using straight line light path, which is the same to the MultiPath water fitter. This can remove the PMTs triggered by photons with late timing, such as the photons reflected off the detector elements (late light) and keep the possible Cherenkov ring hit pattern clear for the direction fitter to fit. Also, dropping the irrelevant PMTs can potentially boost up the fit speed.

- Mode Cut Selector

This selector checks the hit time ( $t_{\text{PMT}}$ ) distributions of all the triggered PMTs and finds a mode value of the hit time ( $t_{\text{mode}}$ ). If  $t_{\text{mode}}$  fails to be found, it calculates a median value ( $t_{\text{median}}$ ) instead[99]. Then it selects the PMT with  $t_{\text{PMT}} \in [t_{\text{mode}} + t_{\text{low}}, t_{\text{mode}} + t_{\text{high}}] \text{ ns}$ . This selector is used to remove the PMTs triggered by noise and light from reflection. The values of  $t_{\text{low}}$ ,  $t_{\text{high}}$  are optimized for different scintillators. For the MPW fitter, the optimized window is  $[t_{\text{mode}} - 50, t_{\text{mode}} + 100] \text{ ns}$  by checking with the fit biases and resolutions for the  $^{16}\text{N}$  central run data in the water phase, while for the MP scint-water fitter the optimized window is  $[t_{\text{mode}} - 100, t_{\text{mode}} + 100] \text{ ns}$  based on checking with the simulations.

- Uniform PMT Selector

This selector is mainly designed for the partial-fill phase and the scintillator phase when a single event can trigger a large amount of PMTs. It reduces the number of the triggered PMTs to a designated number ( $n_{\text{select}}$ ) in order to boost up the fit speed. When an event triggers  $N$  calibrated PMTs, the selector goes through these recorded PMTs and uniformly picks up one PMT by an interval of  $\lceil N/n_{\text{select}} \rceil$ . If  $N \leq n_{\text{select}}$ , the selector does nothing. By doing this, the selector uniformly reduces the number of the PMTs for the fitter without an obvious bias.

- Earliest Hit PMT Selector

Similar to the uniform PMT selector, this selector reduces the number of the triggered PMTs to boost up the fit speed. It first groups the PMTs by their positions in the PMT support sphere. Take the centre of the sphere as coordinate origin, the sphere is divided by the azimuth angle  $\phi$  (as longitude) and zenith angle  $\theta$  (as latitude). In the sphere, the positions of the PMTs in  $\phi$ , ranging in  $[-\pi, \pi]$ , is uniformly divided into  $n$  intervals while the positions of the PMTs in  $\cos \theta$ , ranging in  $[-1, 1]$ , is also divided into  $n$  intervals. Thus, the PMTs are grouped into  $n \times n$  panels, see Fig. 4.23.

For each panel, the selector first drops the PMTs triggered too early ( $t_{\text{PMT}} < 100 \text{ ns}$ ,

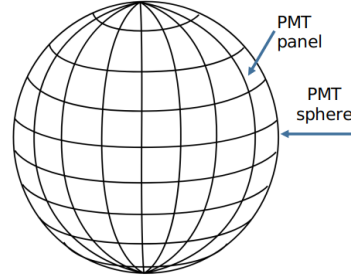


Figure 4.23: Group the PMTs by dividing the PMT sphere with latitudes and longitudes.

where  $100\text{ ns}$  is set as a default threshold). These PMTs could be triggered by noises, such as pre-pulsing. In the rest of the PMTs, the selector picks up one PMT with the earliest  $t_{\text{PMT}}$  in each panel. Thus the number of the PMTs is reduced to  $n \times n$  for the fitter, i.e.,  $n_{\text{select}} = n \times n$ . If  $N \leq n_{\text{select}}$ , the selector does nothing.

We can also use the other timing parameter, such as the  $t_{\text{mode}}$  or the  $t_{\text{median}}$  for selecting the PMT in each panel. However, tests from the simulations for the scintillator phase show that using the earliest hit time gives less fit biases and better fit resolutions.

## Chapter 5

# SNO+ Water Phase Analysis

The SNO+ water data taking from May 2017 to September 2018. During the period from October 2018 to July 2019, LAB (without PPO) was filled into the detector and had been sit inside the neck.

### 5.1 Classifiers

A set of classifiers have been developed since the SNO analysis and been optimized for the SNO+ data [100].

- In time ratio (ITR) classifier

This classifier calculates the ratio of the number of hits in an optimized prompt time window ( $[-2.5, 5.0]$  ns for the water phase) to the total number of hits.

- $\beta_{14}$  isotropy classifier

This classifier uses Legendre polynomials to return the first ( $\beta_1$ ) and the fourth ( $\beta_4$ ) spherical harmonics of an event, where:

$$\beta_l = \frac{2}{N(N-1)} \sum_{i=1}^{N-1} \sum_{j=i+1}^N P_l(\cos \theta_{ij})$$

and  $P_l(\cos \theta_{ij})$  are Legendre polynomials.

The combination of these two polynomials returned by the classifier was practically chosen by the SNO collaboration to be:  $\beta_{14} = \beta_1 + 4\beta_4$  as this gives something that looks kinda gaussian-like for Cerenkov events. Essentially any deviation from zero suggests some polarity (i.e. the event is not isotropic).

- $\theta_{ij}$  isotropy classifier

describes the angle subtended at an event vertex by PMT #i and PMT #j.

$$\cos \theta_{ij} = \frac{(\vec{X}_{PMT\#i} - \vec{X}_{event}) \cdot (\vec{X}_{PMT\#j} - \vec{X}_{event})}{|\vec{X}_{PMT\#i} - \vec{X}_{event}| |\vec{X}_{PMT\#j} - \vec{X}_{event}|}$$

## 5.2 $^{16}\text{N}$ Calibration Scans in the Water Phase

During the water phase, an Nitrogen-16 ( $^{16}\text{N}$ ) calibration source was deployed for internal detector calibration scans in June and November, 2017 and external detector scans in March, 2018.

This source is inherit from SNO experiment[101, 8, 102],

A deuterium-tritium (DT) generator in SNOLAB can produce neutrons through:  $D + T \rightarrow n + ^4\text{He}$ , flow  $CO_2$  gas stream through pipe lines the  $^{16}\text{N}$  isotopes are created by the process:  $n + ^{16}\text{O} \rightarrow ^{16}\text{N} + p$ ,

The  $^{16}\text{N}$  isotope mainly decays through  $\beta$ -decay process:  $^{16}\text{N} \rightarrow ^{16}\text{O} + e^- + \bar{\nu}_e$ . It has a 66.2% chance to emit an electron with an end-point energy of 4.29 MeV and 22.8% chance to 10.42 MeV

[103]

a simplified decay scheme is shown in Fig. 5.1.

6.13 MeV  $\gamma$  rays.

Fig. 5.2 shows the geometry of the  $^{16}\text{N}$  source chamber. The chamber is a stainless steel cylinder mainly containing a small PMT and a gas decay chamber. The chamber was designed to confine the electrons from  $^{16}\text{N}$  decay within the chamber and let them be detected by the PMT inside;

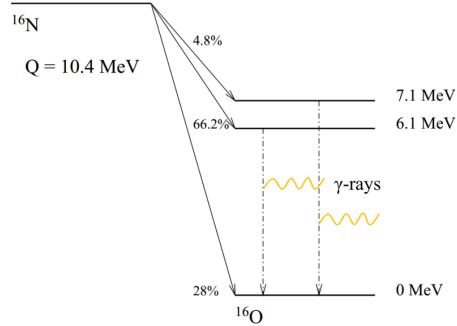


Figure 5.1:  $^{16}\text{N}$  main decay scheme, modified from [8].

to ensure a high fraction of the  $\gamma$ -rays lighthouse where the liquid in the scintillator volume (for example, pure water in the water phase) is free to enter. tagged by a small PMT inside A polyethelene bumper cone is at the bottom of the source. gas capillary tube [101].

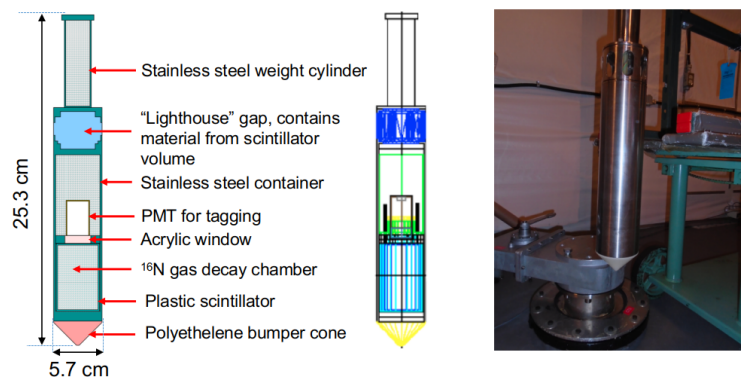


Figure 5.2:  $^{16}\text{N}$  calibration source geometry. Left: a detailed diagram of  $^{16}\text{N}$  source geometry, modified from [9, 10]; middle: source geometry implemented in RAT, modified from [11]; right: a picture of the  $^{16}\text{N}$  source, taken from [12].

The  $^{16}\text{N}$  calibration runs provide an ideal test of fitter performance. From a comparison of reconstructions for data and MC, we can also extract the resolution and bias of the fitter. The  $\gamma$ -rays emitted from the  $^{16}\text{N}$  source interact with the water in the detector mainly

via Compton scattering. Figure 5.3 shows the spatial distributions of the first  $\gamma$ -ray interaction positions projected on the  $x$  axis (called spatial distribution  $S(x)$ ) obtained from MC simulation. The  $^{16}\text{N}$  source is considered as an electron source with a known spatial distribution[94]. For simplicity, in the following we always discuss the  $x$  component of the position vector  $\vec{X}$ .

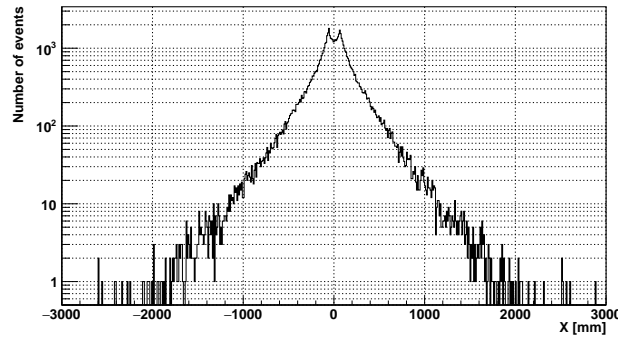


Figure 5.3: Spatial distributions of  $^{16}\text{N}$  first  $\gamma$ -rays interaction position projected on  $x$  axis, obtained from RAT simulations. The double-peak structure is due to the wall of the stainless steel container of the  $^{16}\text{N}$  source.

A position resolution function is defined for the reconstructed electron position distribution[94]:

$$R(x) = \frac{1 - \alpha_e}{\sqrt{2\pi}\sigma_p} \exp\left[-\frac{1}{2}\left(\frac{x - \mu_p}{\sigma_p}\right)^2\right] + \frac{\alpha_e}{2\tau_p} \exp\left[\frac{-|x - \mu_p|}{\tau_p}\right],$$

where  $\alpha_e$  is the fractional exponential component,  $\sigma_p$  is the Gaussian width (corresponding to the position resolution),  $\mu_p$  is the Gaussian shift (corresponding to the position bias) and  $\tau_p$  is the exponential slope (corresponding to the position distributions in tails).

For electrons from the  $^{16}\text{N}$  calibration source, their spatial distribution function  $N_R(x)$  can be described by the position resolution function smeared by the convolution of  $S(x)$  as[94]:

$$N_R(x) = \int_{-\infty}^{+\infty} S(x)R(x_{fit} - x)dx.$$

Since the  $S(x)$  and  $N_R(x)$  are histograms obtained from the data and MC, we calculate by the bin value  $x_i$ :

$$N_R(x_i) = \sum_{x_i=-\infty}^{+\infty} S(x_i)R(x_{fit}^i - x_i).$$

The  $\chi^2$  is calculated by:

$$\chi^2 = \sum_{i=0}^{N_{bins}} \left[ \frac{N_R(x_{fit}^i) - N_R^{fit}(x_{fit}^i)}{\sigma_i} \right]^2,$$

where  $N_R^{fit}$  is a trial fit to the  $N_R$  by tuning the  $\{\alpha_e, \mu_p, \sigma_p, \tau_p\}$  and  $\sigma_i$  is taken as the bin width of the histograms.

By minimizing the  $\chi^2$ , the parameters of the resolution function,  $\{\alpha_e, \mu_p, \sigma_p, \tau_p\}$  and a best  $N_R^{fit}$  are obtained.

Figure ?? shows a comparison of the reconstructed x position of  $^{16}\text{N}$  events between data and MC. The reconstructed position distributions are fitted with  $N_R^{fit}$ .

Table 5.1 summarizes the values of position resolution parameters obtained from data and MC of  $^{16}\text{N}$  calibration runs at the detector center.

Table 5.1: Position resolution parameters for the MP Water Filter.

MPW fitter	$\alpha_e$	$\sigma_P$ (mm)	$\tau_P$ (mm)	$\mu_P$ (mm)
data	$0.58 \pm 0.04$	$175.8 \pm 3.8$	$288.0 \pm 5.7$	$-28.8 \pm 1.0$
MC	$0.51 \pm 0.05$	$195.2 \pm 3.3$	$298.4 \pm 6.1$	$-10.9 \pm 1.0$

Vertex likelihood surface for an typical  $^{16}\text{N}$  event (calibration run-100934\_s000\_p001, event GTID = 61836), projected on X-Y, X-Z and Y-Z planes. A clean global maxima gives the reconstructed vertex: the fitted position is at (-211.958, 503.399, 275.990) mm and the fitted time at 217.03885 ns. This is shown in Fig. 5.4.

emit  $\gamma$ -rays. These  $\gamma$ -rays will Compton scatter off electrons and the electrons will emit Cherenkov light to be detected by the PMTs.

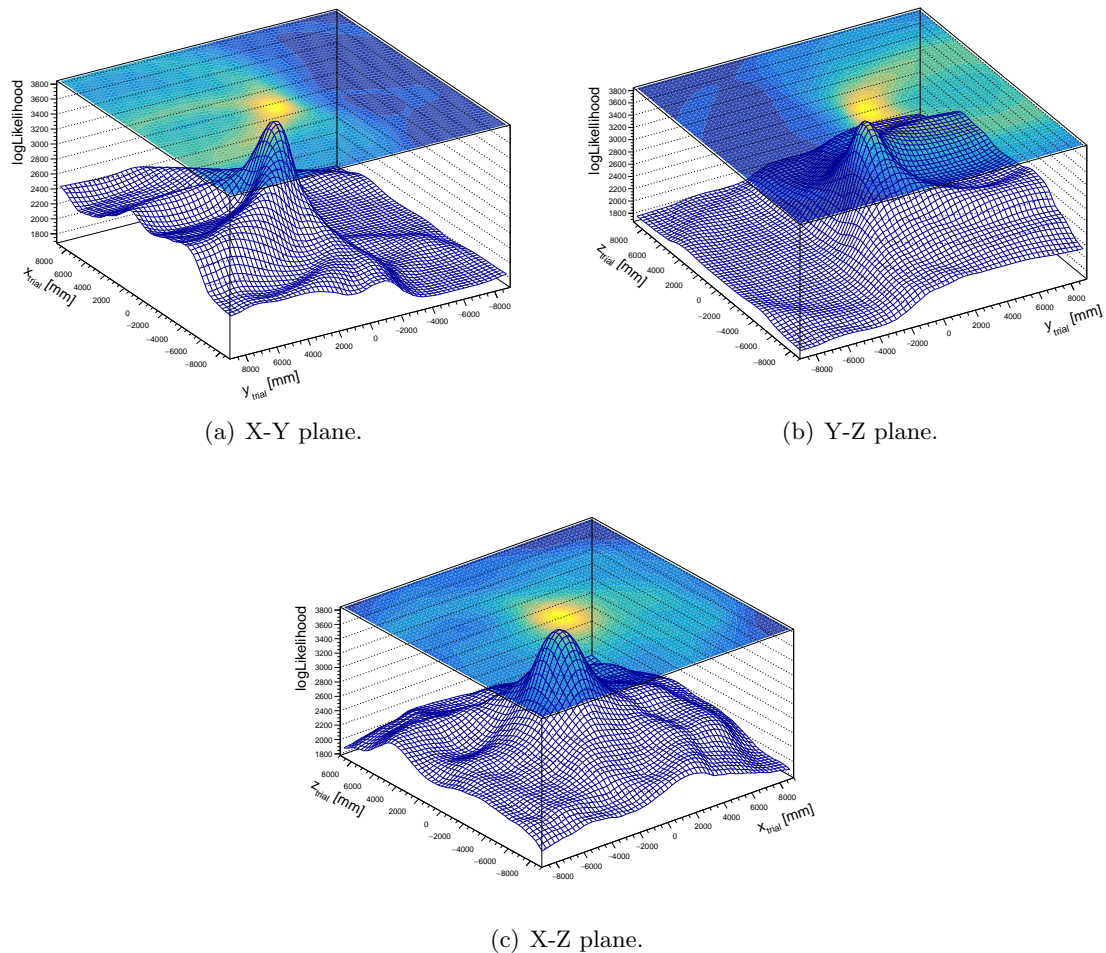


Figure 5.4: Likelihood surface of an  $^{16}\text{N}$  event projected on X-Y, Y-Z, X-Z planes. A clear global maxima is reached for the fitted vertex.

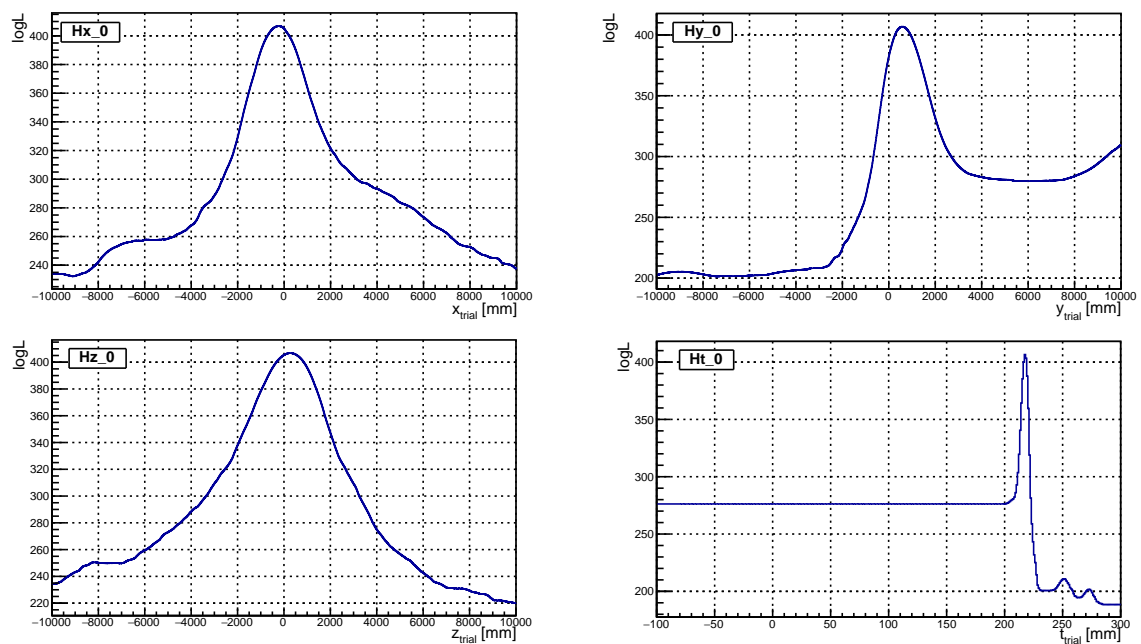


Figure 5.5: Likelihood surface of an  $^{16}\text{N}$  event projected on x, y, z, t axes.

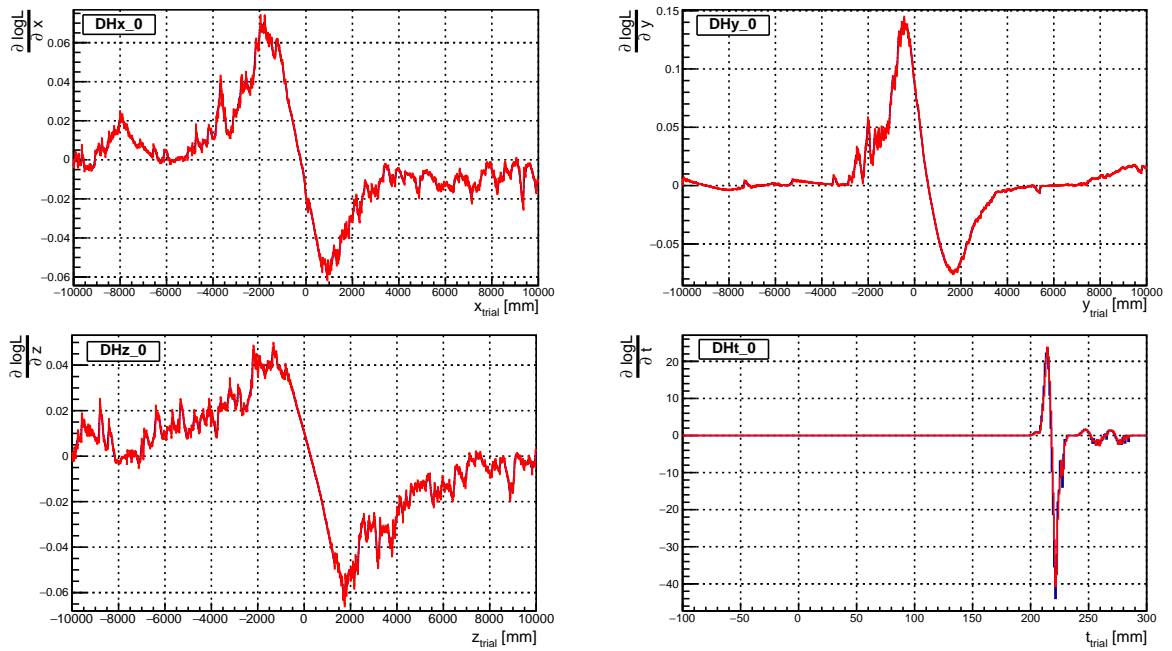


Figure 5.6: Derivatives of  $\log \text{Likelihood}$  of an  $^{16}\text{N}$  event projected on  $x$ ,  $y$ ,  $z$ ,  $t$  axes. The analytical derivatives (blue) are overlaid with numerical derivatives (red). They are well-matched.

# Chapter 6

## Towards the SNO+ Future Phases

### 6.1 Partial-fill Phase Analysis

During the August to October 2019, the PPO is added into the LAB when the water level was at 5100 mm (in PSUP coordinate). This is one of the stages of the partial-fill phase.

As mentioned in Chapter 3, the main purpose of the partial-fill phase is to identify the background level of the liquid scintillator.  $^{16}\text{N}$  and  $\text{AmBe}$  calibration sources were also deployed in the external water to test the response of the detector.

During the filling, the LAB was first filled into the AV to replace the water. PPO was later mixed with LAB and added into the AV. At some stage, the PPO concentration was kept at 0.53 g/L, which was lower than the nominal 2 g/L. At the lower PPO concentration, the liquid scintillator has a slower timing profile. This also brings an opportunity to extract the Cherenkov signals from the liquid scintillator with low PPO concentration.

#### 6.1.1 Sky-shine Classifier

During the partial-fill phase, a Sky-shine classifier was suggested by Mark Chen and developed by Jeff Tseng to discriminate the noise events coming from the top of the detector, the so-called “sky shine” events, from other backgrounds events in the AV detection region[13]. These sky shine events are mostly the backgrounds from radioactive decays happening in

the neck region.

For an event happens in the neck region, it can trigger more PMTs in the bottom (or the lower hemisphere) of the PSUP sphere than in the higher hemisphere, as illustrated in Fig. 6.1. The classifier counts the number of the triggered PMTs with  $z_{PMT} < -1000$  mm (in PSUP coordinate) as  $nSignal$  and the number of the ones with  $-1000 < z_{PMT} < 8000$  mm as  $nSide$ . The ratio  $skyShine = nSide/nSignal$  is the output value of the classifier. Meanwhile, the classifier also saves the counts of the triggered neck PMTs ( $nNeck$ ) as well as the triggered outward looking (OWL) PMTs in high z positions with  $z_{OWL} > 8000$  mm ( $nOWL$ ).

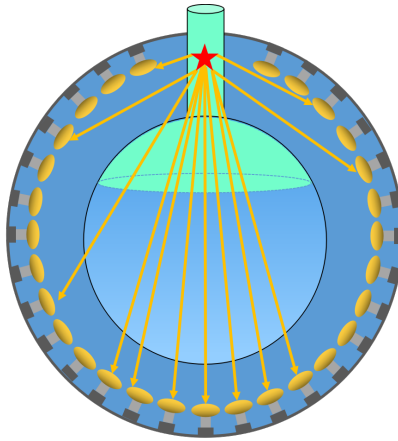


Figure 6.1: An illustration for the Sky-shine classifier, modified from [13].

In the following, I studied the performance of the Sky-shine classifier and attempted to obtain an optimized cut on the value of  $skyShine$  based on the MC simulations.

### Performance of the Sky-shine Classifier

The MC simulations of the  $^{208}\text{Tl}$  decay events were produced in a partial-fill geometry with the water level set at 4435 mm (in AV coordination) and 2 g/L PPO concentration. The  $^{208}\text{Tl}$  decay events were distributed uniformly in the scintillator region. 4067 events of  $^{208}\text{Tl}$  decays were simulated (about 16 times the expected number of events per year based on the SNO+ background evaluations[104]) and 3784 events were triggered. RAT version 6.16.9

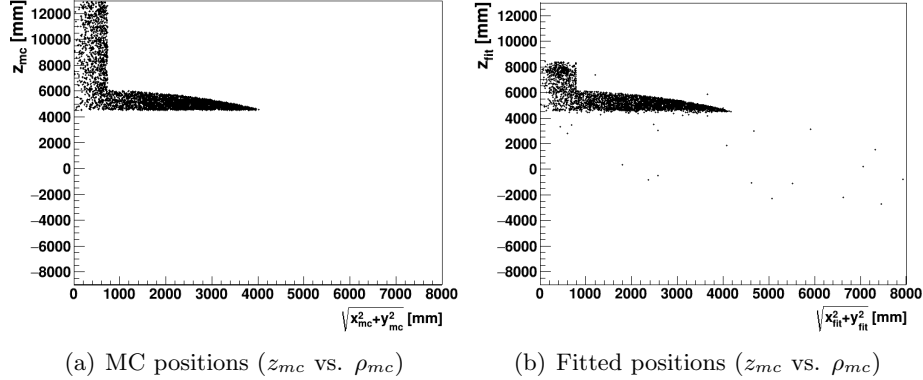


Figure 6.2: MC (left) and fitted positions (right) of  $^{208}\text{Tl}$  simulations.

was used.

Fig. 6.2 shows the positions of the simulated events and the fitted events. In the MC simulations, events are distributed in the AV as well as the whole region of the neck. Recall that the neck of the detector is 8-m tall, the MC simulated neck events from  $z_{neck, bottom} = 6108 \text{ mm}$  up to about  $z_{neck, top} = 13000 \text{ mm}$  in the PSUP coordinate. The valid reconstruction region is inside the PSUP sphere, thus only a small fraction of the neck events in the volume of the neck cylinder inside the PSUP sphere can be fitted or even be triggered.

The plots shows events with small values of Sky-shine calculations can be tagged as neck events.

By checking the MC events positions (“true” event positions), for all the triggered events, 16.8% of them are outside the AV. Apply skyShine<sub>>1.7</sub> can remove 98.6% of the events outside the AV (mostly in the neck) with a sacrifice of 0.2% of the events inside the AV.

### Optimize the Sky-shine Cuts

Since the Sky-shine classifier removes neck events (most of them are outside the PSUP) which are not properly fitted, a skyShine cut can reduce the fit biases and improve the fit resolution.

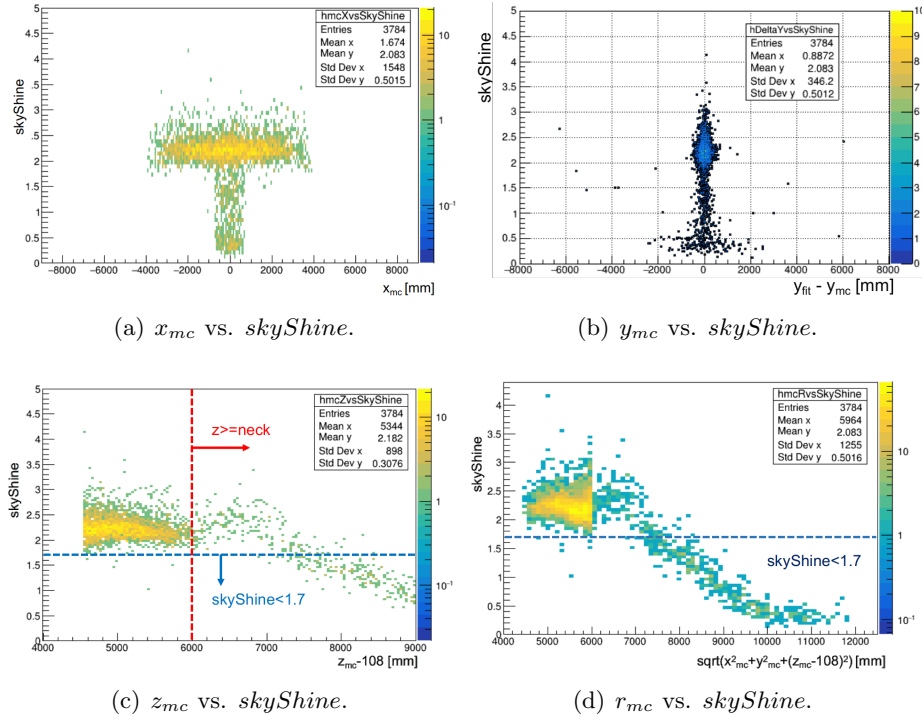


Figure 6.3: MC positions vs. skyShine values for simulated  $^{208}\text{Tl}$  events.

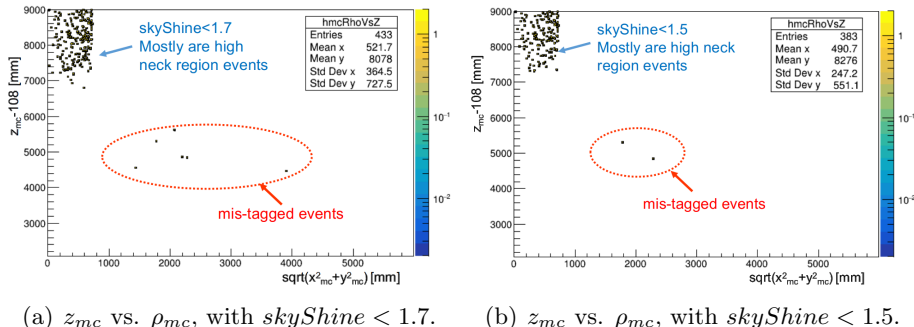


Figure 6.4: MC positions after Sky-shine cuts ( $skyShine < 1.7$  and  $skyShine < 1.5$ ) for simulated  $^{208}\text{Tl}$  events. It shows that most of the events with small  $skyShine$  values are located in the neck region while very few events in the FV region can be mis-tagged.

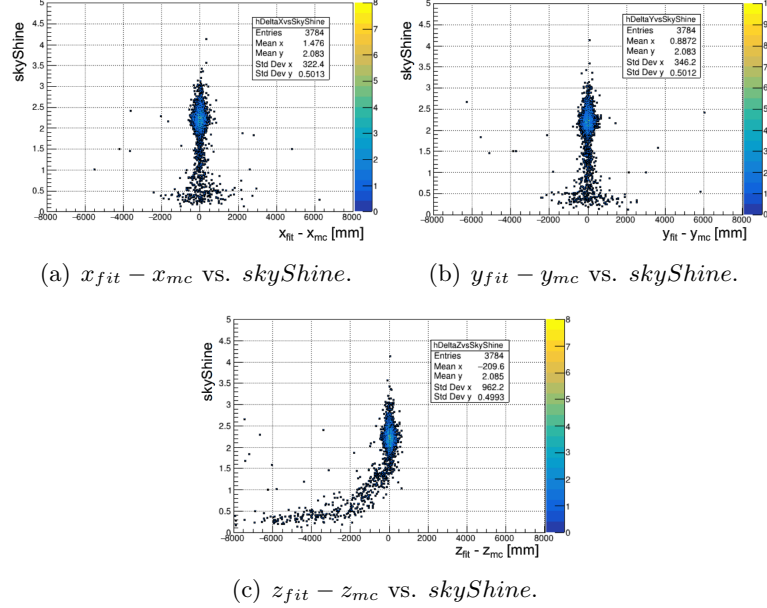


Figure 6.5: Fit biases vs.  $skyShine$  values for simulated  $^{208}\text{Tl}$  events.

$skyShine$  vs. fit biases ( $^{208}\text{Tl}$ )

An improvement of  $\sim 18$  mm in z resolution.

Apply different cuts of  $skyShine$ :  $skyShine > 1, 1.01, 2.0$ , begins from 1.0 with a 0.01 step until 2.0. Plot the x bias  $x_{fit} - x_{mc}$  versus the  $skyShine$  cut values.

Fit a gaussian to  $x_{fit} - x_{mc}$  and get  $\sigma_x$ , Do the same thing to the  $y_{fit} - y_{mc}$ ,  $z_{fit} - z_{mc}$  and obtain  $\sigma_x, \sigma_y, \sigma_z$  Fill a 1D histogram of Sky-shine cut and  $\Delta R = \sqrt{\sigma_x^2 + \sigma_y^2 + \sigma_z^2}$

Compare to the number of MC events inside the scintillator  $\text{sqrt}(x^2 + y^2 + (z - 108)^2) < 6005 \text{ mm} \& z - 108 < 6000 \text{ mm}$ , number of MC events/number fitted events after cut:  $skyShine > 1.6$ : 3149/3376  $skyShine > 1.7$ : 3149/3351 Can check with more productions/higher statistics.

### 6.1.2 Different PPO Concentrations during the Filling

Oxford group in the SNO+ collaboration has done a few bench-top measurements for the time constants and relative light yields of LAB mixed with different concentrations of PPO[14].

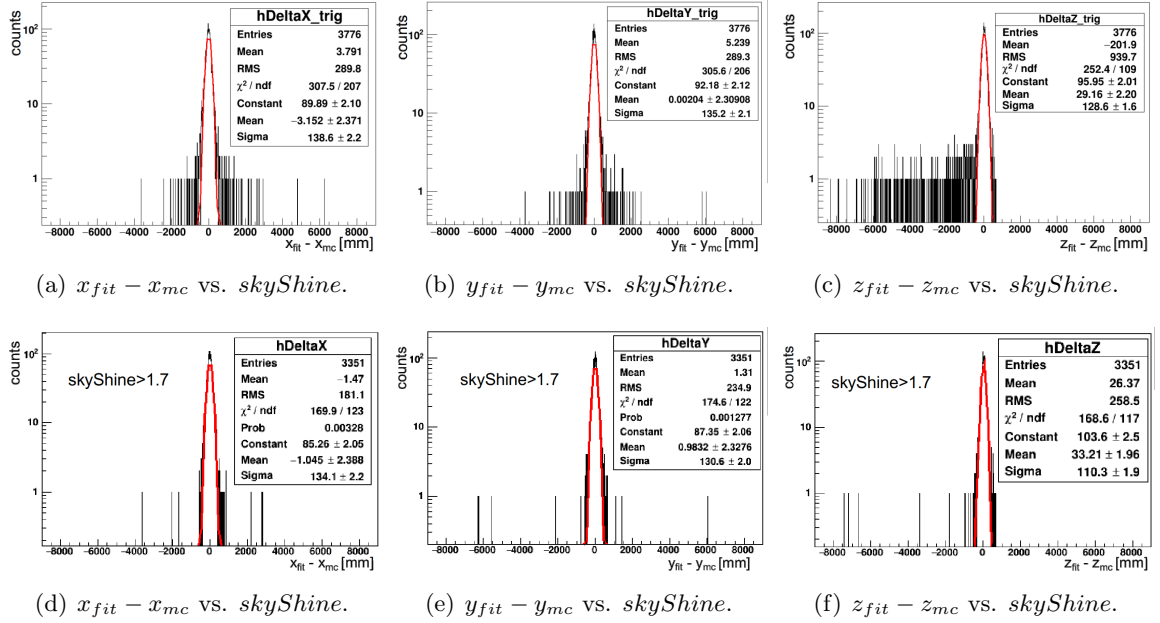


Figure 6.6: Fit biases vs. skyShine values for simulated  $^{208}\text{Tl}$  events.

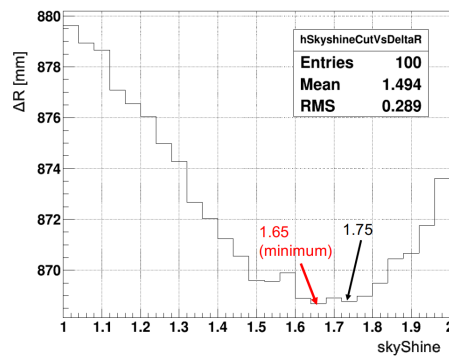


Figure 6.7: Radial resolutions with different skyShine cuts.

The emission time profiles and relative light yields of PPO dissolved in LAB at the following concentrations: 0.25, 0.5, 1.0, 2.0 and 6.0 g/l.

The partial fitter is re-coordinated according to these measurements.

Table 6.1: time constants and amplitudes measured by Oxford group [14].

PPO [g/L]	$\tau_{rise}$ [ns]	$\tau_1$ [ns]	$\tau_2$ [ns]	$\tau_3$ [ns]	$A_1$ [%]	$A_2$ [%]	$A_3$ [%]	$A'$ [%]
0.25	1.25	8.1	25.0	68.2	29.2	53.1	13.9	3.8
0.5	1.12	7.2	18.7	49.1	43.5	40.4	12.6	3.5
1.0	1.18	5.5	13.3	40.9	45.6	37.5	13.3	3.6
2.0	1.06	4.2	11.7	48.9	57.9	27.8	8.9	5.4
6.0	0.94	2.5	9.3	46.0	63.7	17.0	8.6	10.7

$$\sum_{i=1}^3 \left( A_i \frac{e^{-\frac{t}{\tau_i}} - e^{-\frac{t}{\tau_{rise}}}}{\tau_i - \tau_{rise}} \right) + A' \frac{e^{-\frac{t}{\tau_{rise}}}}{\tau_{rise}}$$

based on these measured parameters, pdfs were built.

relative light yield (2g/L = 11900)

Table 6.2: Relative light yield measured by [14].

PPO [g/L]	RLY
0.25	0.57
0.5	0.65
1.0	0.9
2.0	1.0
6.0	0.93

The partial fitter is robust with changes of time profile pdfs.

radial biases

Table 6.3: Tuned effective group velocities for different PPO concentrations.

PPO [g/L]	$V_{gr,scint}$ [mm/ns]	$n_{scint}$	$V_{gr,water}$ [mm/ns]	$n_{water,tuned}$
0.25	$184.068 \pm 5.153$	1.629	$211.871 \pm 5.731$	1.415
0.5	$183.467 \pm 5.159$	1.634	$211.587 \pm 5.773$	1.417
1.0	$182.93 \pm 5.193$	1.639	$211.393 \pm 5.805$	1.418
2.0	$183.045 \pm 5.184$	1.638	$211.629 \pm 5.767$	1.417
6.0	$184.218 \pm 5.135$	1.627	$211.173 \pm 5.843$	1.420

Simulate 5000 events for 3 MeV  $e^-$ ,

$$\Delta x = x_{fit} - x_{mc}$$

Table 6.4: Fit speeds and biases for various PPO concentrations.

PPO [g/L]	fit speed [s/event]	$\Delta x$ [mm]	$\Delta y$ [mm]	$\Delta z$ [mm]	radial bias [mm]
0.25	0.190	6.65	2.64	-18.24	-7.22
0.5	0.144	-0.73	-1.69	-8.14	3.30
1.0	0.190	1.42	0.57	-5.65	10.67
2.0	0.194	0.34	1.78	-4.01	13.37
6.0	0.145	-0.11	-0.12	-25.97	-10.97

$z_{fit}$  resolution [mm]

fit with wrong PPO concentrations:

Table 6.5: Fit speeds and biases for various PPO concentrations.

PPO [g/L]	$\Delta x$ [mm]	$\Delta y$ [mm]	$\Delta z$ [mm]	radial bias [mm]			
0.25	6.80	2.90	-14.61	121.6	-4.82	120.3	93.70%
0.5	5.15	2.82	-12.85	120.2	1.34	123.0	93.46%
1.0	2.32	1.95	-13.22	120.3	0.344	121.9	93.78%
2.0	5.76	3.03	-9.61	119.3	7.264	125.1	93.26%

PPO in Fitter configuration

### 6.1.3 Bi-Po Analysis

### 6.1.4 Partial-fill Phase Calibration

water level was at 5100 mm from the center of the AV (in AV coordination). LAB with a PPO concentration of 0.53 g/L

Effect of the water level.

The  $^{16}\text{N}$  source was deployed in the external water region during the partial-fill phase. run 251748 2019/09/19 and

Source position was at  $(-1120.8, 1041.4, 6172.5)$  mm for a 30-minute duration and at  $(-1120.8, 1041.4, 6108.0)$  mm for a 7-hour duration (separated into 7 runs).

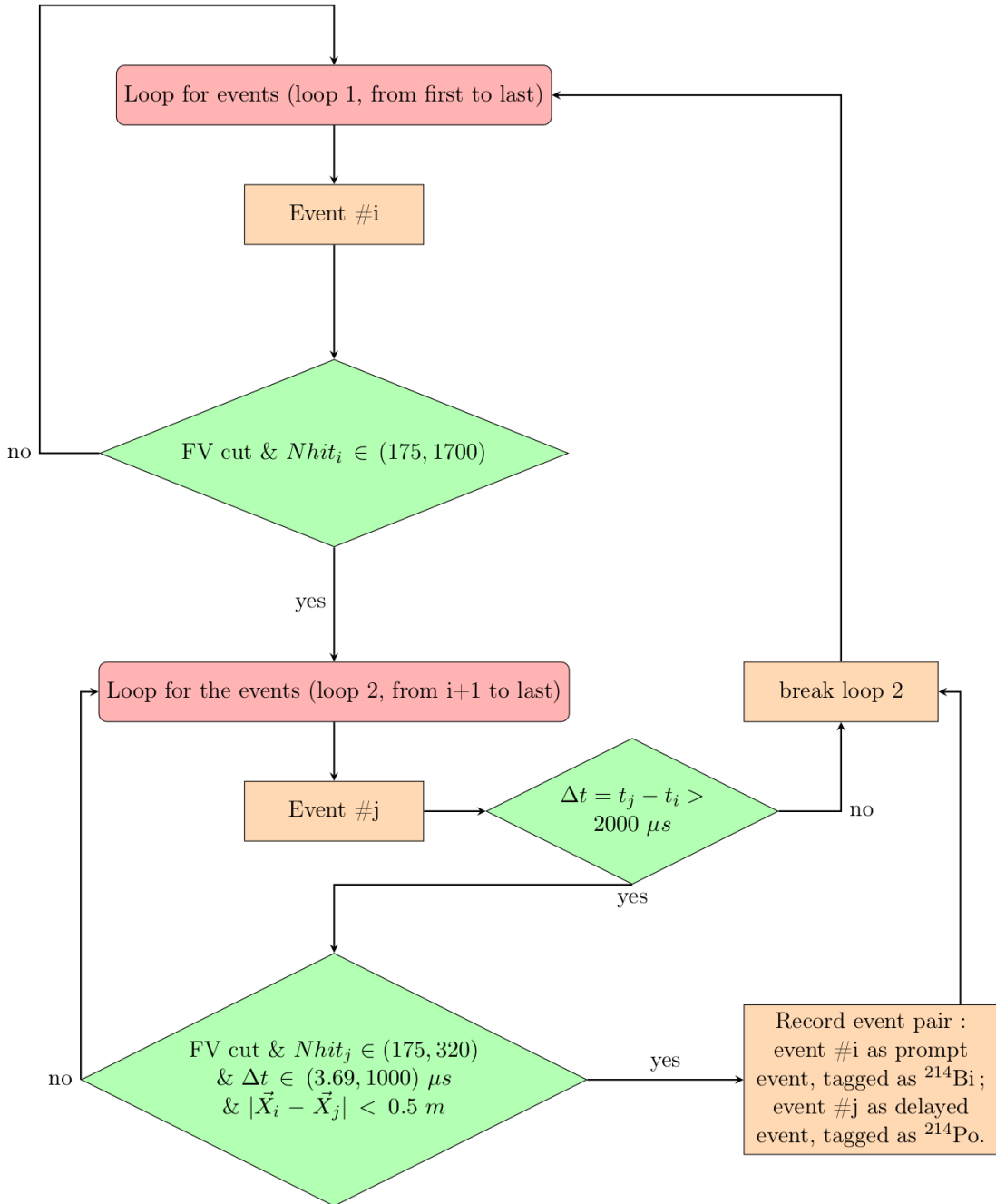


Figure 6.8: A flow chart for Bi-Po tagging.

### 6.1.5 Extract Cherenkov Signals in Partial-fill Phase

For an event happens in liquid scintillator, the number of Cherenkov photons it created is only  $\sim 5\%$  of the total photon numbers, which is a very small fraction compared to the number of scintillation photons. This causes the directional Cherenkov signals are submerged in the isotropic lights.

a time cut window on the time residual was optimized for the searching based on MC simulations in pure scintillator phase.

Hough transformation is a pattern recognition algorithm used in image analysis and computer vision[105]. This algorithm was first invent to extract patterns in bubble chamber[106], is used by Super-K[107].

The Hough transformation algorithm was suggested by Eugene W. Beier for the reconstruction of event direction in the SNO+ scintillator phase.[108]

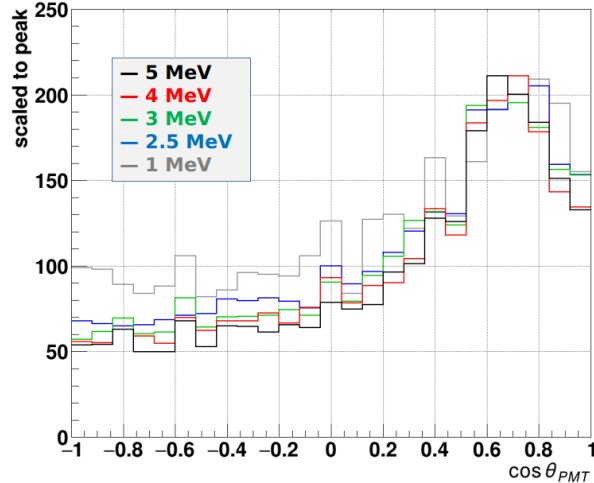


Figure 6.9: Distributions of  $\cos \theta_{PMT}$  after the prompt time cut for various  $e^-$  energies simulations.

In the case that  $e^-$  are generated uniformly and isotropically in the detector, to enhance the Cherenkov ring pattern, a transformation is applied as following:

$$\phi = \hat{\vec{v}}_e \cdot \hat{\vec{v}}_{assume}$$

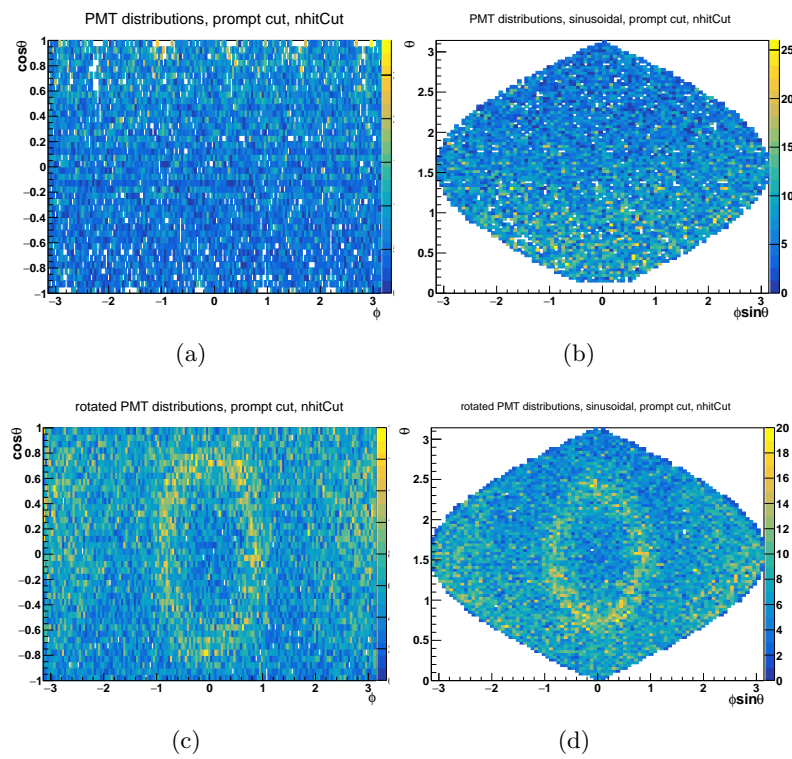


Figure 6.10: PMT hit patterns after the prompt time cut and NHit cut.

$$\vec{n} = \hat{\vec{v}}_e \times \hat{\vec{v}}_{assume}$$

$$R = \begin{bmatrix} n_x^2(1 - \cos \phi) + \cos \phi & n_x n_y(1 - \cos \phi) - n_z \sin \phi & n_x n_z(1 - \cos \phi) + n_y \sin \phi \\ n_x n_y(1 - \cos \phi) + n_z \sin \phi & n_y^2(1 - \cos \phi) + \cos \phi & n_y n_z(1 - \cos \phi) - n_x \sin \phi \\ n_x n_z(1 - \cos \phi) - n_y \sin \phi & n_y n_z(1 - \cos \phi) + n_x \sin \phi & n_z^2(1 - \cos \phi) + \cos \phi \end{bmatrix}$$

$$\vec{v}'_e = R\vec{v}_e$$

$$\vec{X}'_{evt} = R\vec{X}_{evt}$$

Move  $\vec{X}'_{evt}$  to the origin,

$$\vec{X}'_{pmt} = R\vec{X}_{pmt} - \vec{X}'_{evt}$$

Breit-Wigner function

$$p(x) = \frac{c_0}{\pi} \frac{\frac{1}{2}\Gamma}{(x - m)^2 + (\frac{1}{2}\Gamma)^2} + c_1$$

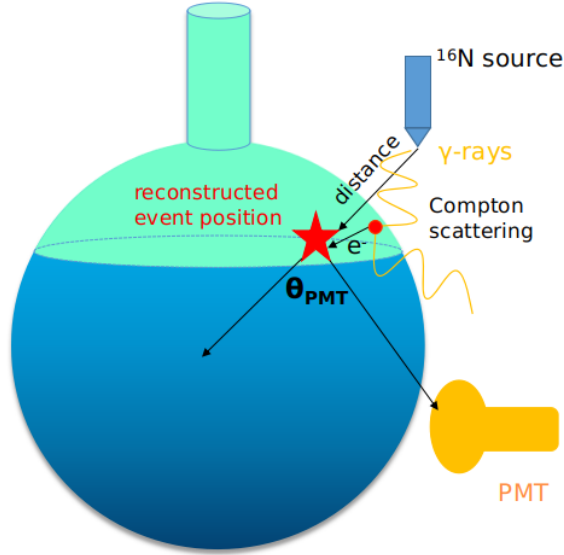


Figure 6.11:  $^{16}\text{N}$  source calibration in external water during the partial-fill phase.

### AmBe Source Analysis

The *AmBe* source

## 6.2 Relative Light Yield Measurements of the Te-loaded Liquid Scintillators

As described in Chapter 3, the energies of charged particles are converted into photons by the scintillator medium. By measuring the amount of the light, the energy of the particle from a certain process can be inferred. To measure the summed energy spectrum of the two electrons is the major task for a particle physics experiment searching for the possible  $0\nu\beta\beta$ -decay signal.

For the  $^{130}\text{Te}$   $0\nu\beta\beta$ -decay process, the signature energy peak is at  $2.5 \text{ MeV}$ [53]. This peak is relatively small and can be immersed in the ubiquitous radioactive decays from natural sources, such as the natural Uranium and thorium decay chains existing in the materials [cite whitepaper]. Therefore, the  $0$ -decay experiments require a very high energy resolution to distinguish the signal from the backgrounds. For the liquid scintillator, it is expected to create as large amount of light caused by a particle interaction as possible. A quantity of light yield, defined as the number of photons for per MeV energy deposit (photons/MeV) by a particle interaction, is used for describing the detection property of the liquid scintillator.

Here we measured the light yield of 0.5% Tellurium loaded LAB (TeLS) samples relative to the LAB-PPO scintillator (relative light yield, RLT). With tellurium loading into the LAB, the light yield of the liquid scintillator will go down since the tellurium atoms can block the photon transmissions to the photosensors. The light yield of the TeLS is crucial for the  $0\nu\beta\beta$ -decay experiments since it determines the energy resolution. It is also crucial for the experiments that are aimed to develop high light yield Tellurium-loaded scintillators [109].

### 6.2.1 Measurement Setup and Data Acquisition

We first prepared LAB+2 g/L PPO by dissolving PPO into the pure LAB. The LAB-PPO mixture was distilled by heating and flowing with liquid nitrogen to remove humidity and

oxygen, which can affect the light yield, for 48 hours. The distilled LAB-PPO was added into the original 16.5% weight Te-butanediol samples to dilute into the 0.5% TeLS samples. Te-butanediol samples from both of the DDA and SOP synthesis procedures are prepared and are referred as TeDDA and TeSOP samples respectively. These samples are further transferred into scintillation vials for the measurement. These vials have PTFE caps sealed on the top of the glass cylinders. To avoid air bubbles created by squeezing the vial cap into the liquid, the liquid level for each sample is kept at 30 mm. The dimensions of the vial is shown in the left picture of Fig. 6.12.

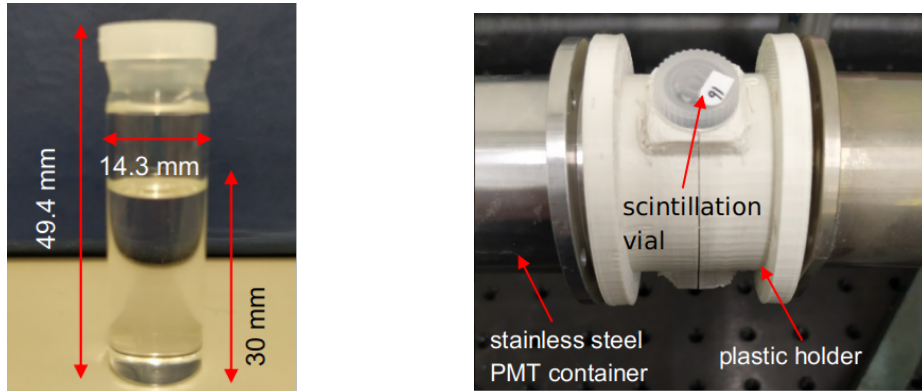


Figure 6.12: Test sample (left) and setup (right). Left: The samples were filled into scintillation vials. The dimensions are shown in the picture. Right: two PMTs are aligned to face to the scintillation vial from each side.

Two Hamamatsu R580 PMTs [cite PMT] were used for detecting the light. The diameter of the PMT round surface is 38.71 mm. These PMTs were housed in stainless steel cylinders (PMT holders), set face to face, looking at the scintillation vial from each side. The PMTs and the vial were aligned by a plastic piece, as shown in the right picture in Fig. 12. The plastic piece is in a cylindrical shape with a hole on the top to plug in the scintillation vial and a slot at the bottom to attach a radioactive source. Inside the cylinder, there is a button-shaped groove at the bottom to fix the vial plugged in and keep the vial upright. Also, a 2-mm-diameter hole was drilled at the bottom of the piece to allow the radiation rays to go inside from the bottom. The surface inside was polished to reduce the absorption of the material to the photons. The piece is made of plant-based and biodegradable PLA

filament and was machined by 3D-printing facility. The pictures of the piece are shown in Fig. 13.

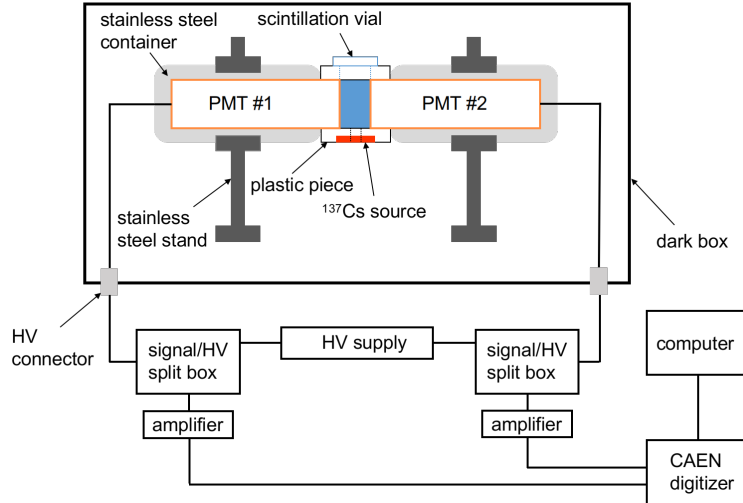


Figure 6.13: A diagram shows the light yield measurement setup. See the text for details.

Fig. 6.13 shows a diagram of the whole measurement setup. The plastic piece held the radioactive source and the scintillation vial. It also aligned two PMTs to face to the scintillation vial from each side. The piece can shield lights from outside as well. These setups were placed in a dark box to prevent the lights from lab. Two RG59/U type high voltage (HV) cables connected the PMTs to an HV supply outside the dark box. The HV cables were connected to two signal/HV split boxes to separate the HV current and electrical signals. Due to the resistor of the split box, the HV supply was set to 2200 Volts (V) for the PMT operation while the operation voltage suggested by the Hamamatsu is 1800 V.

The signal cables from the split box were connected to a two-channel Hewlett Packard (HP) amplifier. This amplifier inverted the signals and amplified them by 26 dB. The amplified signals were then input into a two-channel digitizer. The digitizer records the data and sent them to a desktop computer.

To obtain and analyze the data, we used a desktop Waveform Digitizer, the DT5751 module provided by the Costruzioni Apparecchiature Elettroniche Nucleari S.p.A (CAEN).

Running at a digital pulse processing mode, the module records the digitized PMT waveforms with a data-taking rate of 1 GHz for each channel [cite CAEN].

This module is controlled by the CoMPASS software, which is provided by CAEN. The software sets up the threshold and trigger parameters. For each triggered event which passes the threshold, the software records event time, trigger flag and waveform histograms from the two channels. By integrating the waveforms, it can also calculate the energy of a triggered event [cite compass].

Each channel recorded the signals from each PMT individually. With the two-PMT setup, we applied coincidence time mode measurements. In the coincidence mode, a coincidence time window between two channels were set to 48 ns. For a certain event, the CoMPASS software compares the event time difference between two channels and only records it if the event time differences is less than 48 ns. A smaller window of 10 ns was further applied for analysis.

Fig. 12: Test sample (left) and setup (right). Left: The samples were filled into scintillation vials. The dimensions are shown in the picture. Right: Two PMTs are aligned to face to the scintillation vial from each side.

Fig. 13. The plastic piece holds the radiation source and the scintillation vial. It also aligns the PMTs to face the vial from two sides. Fig. 14: Diagram for the light yield measurement setup. See the text for details.

#### Measurement

The liquid scintillator samples we have measured are: LAB-PPO, TeDDA, TeSOP. The unloaded LAB-PPO sample served as a standard candle.

A Cesium-137 ( $^{137}\text{Cs}$ ) radioactive source was always placed at the bottom of the scintillation vials. The source was made by Radiochemical Centre Amersham. The radioactivity measured on 1st April 1974 was 11.09 *microcurie*( $\mu\text{Ci}$ ), with an accuracy of 3.7%. The activity was expected to be in this thesis, considering a half-life of 30.08 years for the  $^{137}\text{Cs}$ [103].

has a 85.10% chance to emit 0.661 MeV  $\gamma$ -rays[103]. These  $\gamma$ -rays can travel into the

liquid scintillator samples in the vial, interact with the samples and create scintillation photon.

For each sample, measurements were taken for one-minute time duration. Waveforms from the PMT photo-current signals were digitized in a 252 ns time window. Shown in Fig. 6.14 is a typical waveform caused by  $\gamma$  rays interacted with the LAB-PPO sample. The p.e. signals triggered PMT pulses and the pulses were digitized as waveforms. For each waveform, the digitizer firmware dynamically calculated the baseline as the mean value of 256 data points inside a moving time window of 252 ns. A threshold was set as 100 units above the baseline. The data point on the 90% leading edge of the pulse was taken as the trigger time tag. From this trigger time tag, in the following 80 ns window the digitizer did not calculate another trigger to avoid introducing another pulse (trigger hold-off). Also from the trigger time tag, a pre-gate of 8 ns was set. The waveform was integrated in the time gate of [trigger time - 8, trigger time + 72] ns. This gives the integrated charge, which was calculated as a A/D converter (ADC) channel number. If the measurement system can be calibrated, the ADC channel number can be exactly converted into the energy of the particle interaction. Since here we only interested in the photon numbers, we simply used ADC channel as the energy. Once the pulse in the waveform passed the threshold and a triggered time tag can be found, the digitizer considered it as a triggered event. A time flow started when the measurement began. Time stamps were recorded as event time when the triggered event hapfpened. The waveform was recorded and the ADC channel number (energy) of this event was calculated.

In a coincidence time measurement, the event times of the events recorded by each of the two PMTs were compared. If the event time differences between two events from each PMTs were too long, these two events were considered as random noises rather than the physics events and were not recorded. We optimized a coincidence time cut as 40 ns and set that cut during the digitizer data-taking.

Fig. 6.15 shows the measured LAB-PPO energy spectrum with and without coincidence time cut (10 ns) on the ADC channel 0. Without the coincidence time cut, there exists a

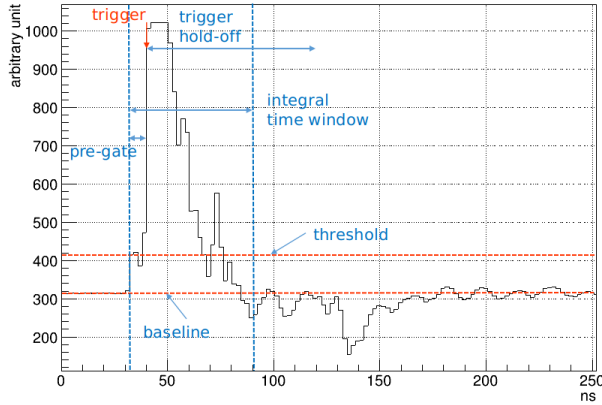


Figure 6.14: A typical waveform triggered by scintillation photons from  $^{137}\text{Cs}$   $\gamma$ -rays interaction with LAB-PPO sample.

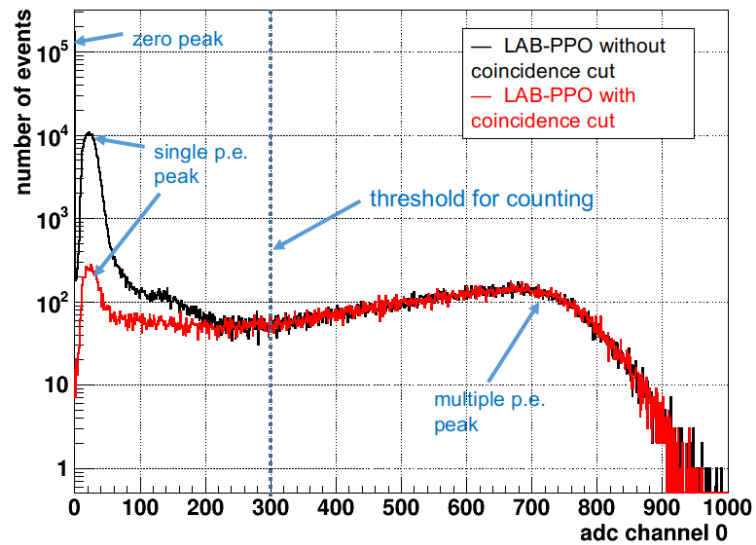


Figure 6.15: Measured LAB-PPO energy spectrum with and without coincidence cut on the ADC channel 0. A threshold for counting is set by comparing the two spectrum.

zero peak, which is caused by the pulses from random electronic noises or fluctuations of the digitized waveforms. The peak on the left is the single p.e. peak. It is mainly caused by some light sources which are weak enough that the photons only strike out at most one single p.e. inside the PMT [cite leo]. The peak on the right is the multiple p.e. peak, in our case is mainly caused by a number of scintillation photons produced by the -ray interacting with the LAB-PPO. In the coincidence time measurement mode, it only records the photons detected by the two PMTs almost simultaneously. Therefore, the zero peak is removed while the single p.e. peak is suppressed. The multiple p.e. peak is consistent with the non-coincidence measurement. A threshold in energy can be set to count only the scintillation photons emitted from LAB-PPO.

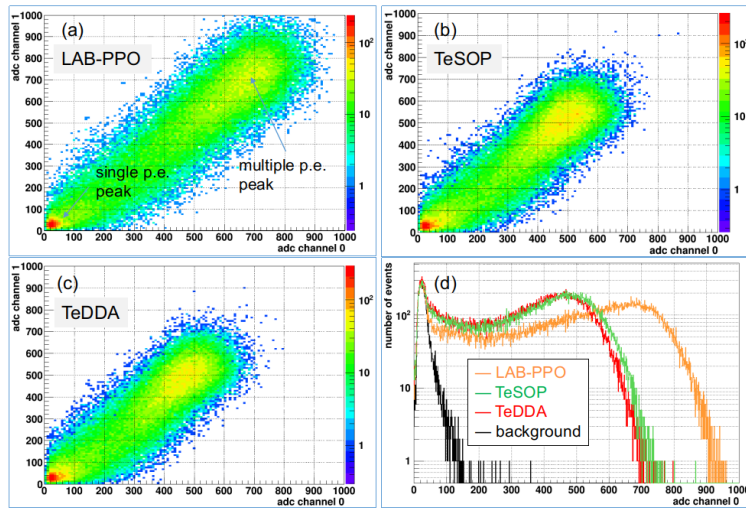


Figure 6.16: 2D energy spectrum of the counting measurements of LAB-PPO (a), TeSOP (b), and TeDDA (c) samples, projected the 2D plots into one channel (d). The single photo-electron (p.e.) peak is mainly caused by backgrounds while the multiple p.e. peak is from scintillation photons.

Fig. 6.16 shows the result of one-minute measurement for the LAB-PPO sample. The data points in the 2D plot represent the triggered event fall in certain ADC channel numbers in each channel. A 10 ns coincidence window cut was applied to cut down noise, single p.e. and background events. The events in the 0 ADC channel, which represent noises, were totally cut off after applying the coincidence. Fig. 18 shows the results of the TeSOP and

TeDDA samples. Compared to the LAB-PPO sample, a shift of the multiple p.e. peak due to the different light yields between the samples can be observed clearly.

In Fig. 18, the 2D plots in Fig. 6.16 are projected onto a single channel. We used an empty vial and let  $\gamma$ -rays from  $^{137}\text{Cs}$  source pass through it for a background run (without the coincidence cut). This is to verify the single p.e. peak and noise region, shown as the black background spectrum.

From this plot, the single p.e. peaks for all the samples as well as the background match together. The multiple p.e. peaks indicate the different light yields of the scintillator samples. Here we can clearly see the multiple p.e. peak of the LAB-PPO occupies the largest ADC channel number, while the channels of TeSOP is slightly larger than the TeDDA.

To quantify the light yield differences between different samples, an analysis method of charge weighted photon number has been applied as the following:

First, from the spectrum, fit the single p.e. peak with an asymmetric Gaussian function, as shown in Fig. 19. The mean value of the asymmetric Gaussian represents the ADC channel number corresponding to the single p.e. peak.

$$\xi = -\frac{\alpha(x-\mu)}{\sqrt{2}\sigma}, f_{asym} = c \cdot e^{-\frac{1}{2}(\frac{x-\mu}{\sigma})^2} \cdot \text{Erfc}(\xi)$$

$$p_0 = \mu, p_1 = \sigma, p_2 = \alpha, p_3 = c$$

Then for the multiple p.e. region, weighting (dividing) the counts of the event in each channel with the single p.e. ADC channel number to calculate the total number of the photons.

Fig. 19. Fit the single p.e. peak with an asymmetric Gaussian function (fasym) to obtain the adc channel for weighting. The mean value of  $p_0$  is used as the adc channel relative to a single p.e. peak.

To define the multiple p.e. region for the counting, the spectrum projected on each channel with and without coincidence cut are compared to define a threshold of the ADC channel for counting. By integrating from this threshold, the total numbers of events between two spectrum are close to each other. From two channels, we get two thresholds and then define a box cut in the 2D coincidence plot. We weights the events in the box to

obtain the total number of photons. Fig. 16 and Fig. 19 show the case of the LAB-PPO sample.

Fig. ?? 2D LABPPO spectrum with coincidence cut. A box cut is defined for multiple PE counting.

Once the total number of the photons for a certain sample is counted, we can calculate its ratio to the LAB-PPO sample to obtain the relative light yield.

## Results

Table 6.6: Number of photons calculated by Charge weighted photon number method.

Sample	Number of photons ( $\times 10^6$ )	RLY
LAB-PPO	2.0811	1
TeDDA	1.2652	0.61
TeSOP	1.3976	0.67

Table. 6.6 shows the number of photons calculated by Charge weighted photon number method.

Here we quantify the relative light yields of our samples. The light yield of the 0.5% Te by SOP synthesis procedure (TeSOP) is 0.61 and the one of the 0.5% Te by DDA procedure is 0.67. The light yield of TeSOP is slightly larger than the TeDDA. In [cite billerTe], a relative light yield of 0.65 was reported.

# Chapter 7

## Conclusions

SNO+ experiment

## Appendix A

# Details for the MultiPath Fitter

### A.1 Create a Random Vertex

Four random seeds are generated from the uniform distribution function: *RandFlat* in Class Library for High Energy Physics (CLHEP) library.

One random seed is used for generating the time of the vertex:  $t$  is a random variable following a uniform distribution in a range of [100, 300] ns, say,  $t \sim U(100, 300)$ .

Three random seeds are used for generating the position of the trial vertex:  $ran0 \sim U(0, 1)$ ,  $ran1 \sim U(-1, 1)$  and  $ran2Pi \sim U(0, 2\pi)$ .

Let  $r = \sqrt[3]{ran0} * 10000$  mm,  $\phi = ran2Pi$ ,  $\cos \theta = ran1$  and  $\sin \theta = \sqrt{1 - \cos^2 \theta}$ , then the trial position can be built in Cartesian coordinate system:  $\vec{x}_{trial} = (r \sin \theta \cos \phi, r \sin \theta \sin \phi, r \cos \theta)$ . This procedure ensures that a proper random position is generated inside a sphere with a radius of 10 m.

### A.2 Levenberg-Marquardt (MRQ) Method for Minimization[1]

Levenberg-Marquardt method is a common routine for non-linear fitting. Let  $\mathbf{a} = [a_0, a_1, \dots, a_{M-1}]^T$  be an  $M$ -dimensional vector with  $M$  unknown parameters to be fit, for example,  $\mathbf{a}$  is an event vertex with 4 parameters:  $\mathbf{a} = [x, y, z, t]^T$ .

A  $\chi^2$  merit function with the unknown parameter vector  $\mathbf{a}$  can be built and by mini-

mizing the function, the best-fit  $\mathbf{a}$  can be found.

The  $\chi^2(\mathbf{a})$  can be approximately expanded into a quadratic form of Taylor-series:

$$\chi^2(\mathbf{a}) \simeq \gamma - \mathbf{d} \cdot \mathbf{a} + \frac{1}{2} \mathbf{a} \cdot \mathbf{D} \cdot \mathbf{a}, \quad (\text{A.1})$$

where  $\gamma$  is a  $M$ -dimension constant vector around  $\mathbf{a}$ ,  $\mathbf{d}$  is a  $M$ -dimension vector and  $\mathbf{D}$  is a  $M \times M$  Hessian matrix.

To find a  $\mathbf{a}_{min}$  so that a  $\min \chi^2(\mathbf{a}_{min})$  is reached, in computing science we usually use iteration steps:

$$\mathbf{a}_{min} = \mathbf{a}_{cur} + D^{-1}[-\nabla \chi^2(\mathbf{a}_{cur})], \quad (\text{A.2})$$

where  $\mathbf{a}_{cur}$  is the current trial value of  $\mathbf{a}$  and we assume matrix  $\mathbf{D}$  is invertible. The  $\mathbf{a}_{cur}$  thus jumps onto  $\mathbf{a}_{min}$ .

According to the definition of a  $\chi^2$  merit function, it can be written out explicitly as:  $\chi^2(\mathbf{a}) = \sum_{i=0}^{N-1} [\frac{y_i - y(x_i|\mathbf{a})}{\sigma_i}]^2$ , with the same Taylor expansion, the quadratic form is written as:

$$\chi^2(\mathbf{a}) \approx \chi^2(\mathbf{a}_{cur}) + \sum_k \frac{\partial \chi^2(\mathbf{a}_{cur})}{\partial a_k} \delta a_k + \frac{1}{2} \sum_{kl} \frac{\partial^2 \chi^2(\mathbf{a}_{cur})}{\partial a_k \partial a_l} \delta a_k \delta a_l, \quad (\text{A.3})$$

where the first derivatives are:

$$\frac{\partial \chi^2}{\partial a_k} = -2 \sum_{i=0}^{N-1} [\frac{y_i - y(x_i|\mathbf{a})}{\sigma_i}] \frac{\partial y(x_i|\mathbf{a})}{\partial a_k}, k = 0, 1, \dots, M-1, \quad (\text{A.4})$$

and the second derivatives are:

$$\frac{\partial^2 \chi^2}{\partial a_k \partial a_l} = 2 \sum_{i=0}^{N-1} \left\{ \frac{\partial y(x_i|\mathbf{a})}{\partial a_k} \frac{\partial y(x_i|\mathbf{a})}{\partial a_l} - [y_i - y(x_i|\mathbf{a})] \frac{\partial^2 y(x_i|\mathbf{a})}{\partial a_k \partial a_l} \right\}, k = 0, 1, \dots, M-1. \quad (\text{A.5})$$

Let  $\beta_k \equiv -\frac{1}{2} \frac{\partial \chi^2}{\partial a_k}$ ,  $\alpha_{kl} \equiv \frac{1}{2} \frac{\partial^2 \chi^2}{\partial a_k \partial a_l}$ , then the factor of 2 is removed. The  $\alpha_{kl}$  is defined as the curvature matrix and  $\alpha = \frac{1}{2} \mathbf{D}$ , which implies that it is the half of the Hessian matrix.

From A.2, we have:  $D(\mathbf{a}_{min} - \mathbf{a}_{cur}) = [-\nabla \chi^2(\mathbf{a}_{cur})] \implies 2\alpha \delta \mathbf{a} = 2\beta$ . The A.2 is now transformed into a systems of linear equations:

$$\sum_{l=0}^{M-1} \alpha_{kl} \delta a_l = \beta_k, \quad (\text{A.6})$$

where  $\delta a_l$  is a varying amount added to the current value of parameter for the next iteration.

The main task now is to calculate  $\alpha_{kl}$  and  $\beta_k$  and then solve for  $\delta a_l$  in A.6. Once  $\delta a_l$  is solved, we can vary the current trial or approximate values of  $\mathbf{a}_{cur}$  and let it go close to or reach the  $\mathbf{a}_{min}$ .

If we consider the method of steepest descent:  $\mathbf{a}_{next} = \mathbf{a}_{cur} - \text{const} \cdot \nabla \chi^2(\mathbf{a}_{cur})$ , where const is a constant, then the  $\delta a_l$  is solved by

$$\delta a_l = \text{const} \cdot \beta_l, \quad (\text{A.7})$$

where no Hessian matrix is needed.

In the Levenberg-Marquardt method, in order to solve for  $\delta a_l$ , the detailed calculation of  $\mathbf{D}^{-1}$  in A.2 and the simplified calculation of steepest descent in A.7 are combined and a smooth transition between A.2 and A.7 is considered.

In A.7, the const describes the distance or magnitude of how far the parameter should go along the gradient  $\beta_l$ . From dimensional analysis, since  $\beta_k \equiv -\frac{1}{2} \frac{\partial \chi^2}{\partial a_k}$  and  $\chi^2$  is a non-dimensional number,  $[\beta_l] = [1/a_l]$ . Then from A.7,  $[\text{const}] = [a_l^2]$ . The const has the same dimension to the term  $1/\alpha_{ll} = 1/(\frac{1}{2} \frac{\partial^2 \chi^2}{\partial a_l \partial a_l})$ , i.e., the diagonal elements in the curvature matrix. A bridge between A.2 and A.7 is thus built. The diagonal elements in the curvature matrix can control the magnitude of the const, tells how far the parameter should go along the gradient.

Then A.7 can be written as:

$$\delta a_l = \frac{1}{\lambda \alpha_{ll}} \beta_l \text{ or } \lambda \alpha_{ll} \delta a_l = \beta_l, \quad (\text{A.8})$$

where  $\alpha_{ll}$  is written in a form of  $\alpha_{ll} = \sum_{i=0}^{N-1} \frac{1}{\sigma_i^2} \left[ \frac{\partial y(x_i | \mathbf{a})}{\partial a_l} \frac{\partial y(x_i | \mathbf{a})}{\partial a_l} \right]$  to ensure that  $\alpha_{ll}$  is always positive; a fudge factor  $\lambda$  can be set to  $\lambda \gg 1$  to avoid the case when the value of const is taken too large.

Compare A.6 and A.8, if define a new curvature matrix  $\alpha'$  as  $\alpha'_{jj} \equiv (1 + \lambda) \alpha_{jj}$  (for diagonal elements) and  $\alpha'_{jk} \equiv \alpha_{jk}$  ( $j \neq k$ ) (for non-diagonal elements), these two equations can be combined into one:

$$\sum_{l=0}^{M-1} \alpha'_{kl} \delta a_l = \beta_k \quad (\text{A.9})$$

From the definition of  $\alpha'$ , if  $\lambda$  takes a large value,  $\alpha'$  is dominated by diagonal elements, then A.9 is close to A.8; while if  $\lambda \rightarrow 0$ , A.9 is close to A.6.

The algorithm of Levenberg-Marquardt method requires a reasonable start value (first guess) of the fitting parameter  $\mathbf{a}$  and a reasonable preset value of  $\lambda$  (usually take  $\lambda = 0.001$ ). The iteration loop of the algorithm is: calculate the value of  $\chi^2(\mathbf{a})$ , solve for  $\delta\mathbf{a}$  from A.9 and then calculate  $\chi^2(\mathbf{a} + \delta\mathbf{a})$ . During this loop, the algorithm checks whether  $\chi^2(\mathbf{a} + \delta\mathbf{a}) \geq \chi^2(\mathbf{a})$ , if it is,  $\lambda$  is increased by  $\lambda = 10 \cdot \lambda$ ; if not,  $\lambda$  is decreased by  $\lambda = 0.1 \cdot \lambda$ .

The iteration loop is terminated when the change amount of the  $\chi^2$  is negligible: if the loop calculates several  $\chi^2$  values which are close to each other (for example,  $|\chi^2_{current} - \chi^2_{previous}| < 0.001$ ), the algorithm will consider the  $\chi^2$  is minimized with a set of best-fit parameters. Here the termination condition of iterating the  $\chi^2$  value to convergence to machine accuracy or to the roundoff limit is not used, since  $\chi^2$  is a statistical quantity rather than a solution of an equation. It is not statistical meaningful to vary the value of  $\mathbf{a}$  to vary  $\chi^2$  by a small amount  $\ll 1$ .

Once the minimum is reached, set  $\lambda = 0$  and then the estimated covariance matrix of the standard errors in the fitted  $\mathbf{a}$  can be calculated as:  $C \equiv \alpha^{-1}$ .

# References

- [1] W. H. Press, S. A. Teukolsky, W. T. Vetterling, and B. P. Flannery, *Numerical recipes 3rd edition: The art of scientific computing*. Cambridge university press, 2007.
- [2] P. G. Jones, *Background rejection for the neutrinoless double beta decay experiment SNO+*. PhD thesis, University of Oxford, 2011.
- [3] J. Birks and F. Firk, “The theory and practice of scintillation counting,” *Physics Today*, vol. 18, p. 60, 1965.
- [4] G. F. Knoll, *Radiation Detection and Measurement*. John Wiley & Sons, 2010.
- [5] E. Turner, “A water scattering scaling factor for rat,” *SNO+ Internal Document, docDB-5864-v2*.
- [6] S. J. Brice, *Monte Carlo and Analysis Techniques for the Sudbury Neutrino Observatory*. PhD thesis, 1996.
- [7] P. Skensved and B. Robertson, “Miscellaneous effects,” *SNO Technical Report, SNO-STR-90-28*.
- [8] M. Dragowsky, A. Hamer, Y. Chan, R. Deal, E. Earle, W. Frati, E. Gaudette, A. Hallin, C. Hearns, J. Hewett, *et al.*, “The  $^{16}\text{N}$  calibration source for the sudbury neutrino observatory,” *Nuclear Instruments and Methods in Physics Research Section A: Accelerators, Spectrometers, Detectors and Associated Equipment*, vol. 481, no. 1-3, pp. 284–296, 2002.

- [9] R. F. MacLellan, *The energy calibration for the solar neutrino analysis of all three phases of the Sudbury Neutrino Observatory*. PhD thesis, 2009.
- [10] M. Mottram, “N16 source update,” *SNO+ Internal Document, docDB-1769-v1*.
- [11] Z. Barnard, “Update to N16 geometry,” *SNO+ Internal Document, docDB-4414-v1*.
- [12] R. Bayes, “Analysis of N16 scan,” *SNO+ Internal Document, docDB-4482-v2*.
- [13] J. Tseng, “Skyshine classifier,” *SNO+ Internal Document, docDB-5341-v1*.
- [14] E. Leming, “Oxford LAB + PPO timing and light yield measurements,” *SNO+ Internal Document, docDB-6179-v1*.
- [15] J. Leite-Lopes, “Weak interaction physics: from its origin to the electroweak model,” tech. rep., SCAN-9607019, 1996.
- [16] H. Bethe and R. Peierls, “The “neutrino”,” *Nature*, vol. 133, no. 3362, pp. 532–532, 1934.
- [17] F. Reines, C. Cowan Jr, F. Harrison, A. McGuire, and H. Kruse, “Detection of the free antineutrino,” *Physical Review*, vol. 117, no. 1, p. 159, 1960.
- [18] H. A. Bethe, “Energy production in stars,” *Physical Review*, vol. 55, no. 5, p. 434, 1939.
- [19] C. Giunti and C. W. Kim, *Fundamentals of neutrino physics and astrophysics*. Oxford university press, 2007.
- [20] W. C. Haxton, R. Hamish Robertson, and A. M. Serenelli, “Solar neutrinos: status and prospects,” *Annual Review of Astronomy and Astrophysics*, vol. 51, pp. 21–61, 2013.
- [21] J. N. Bahcall, A. M. Serenelli, and S. Basu, “New solar opacities, abundances, helioseismology, and neutrino fluxes,” *The Astrophysical Journal Letters*, vol. 621, no. 1, p. L85, 2005.

- [22] R. Becker-Szendy, C. Bratton, D. Casper, S. Dye, W. Gajewski, M. Goldhaber, T. Haines, P. Halverson, D. Kielczewska, W. Kropp, *et al.*, “Electron-and muon-neutrino content of the atmospheric flux,” *Physical Review D*, vol. 46, no. 9, p. 3720, 1992.
- [23] W. Allison, G. Alner, D. Ayres, W. Barrett, C. Bode, P. Border, C. Brooks, J. Cobb, D. Cockerill, R. Cotton, *et al.*, “Measurement of the atmospheric neutrino flavour composition in soudan 2,” *Physics Letters B*, vol. 391, no. 3-4, pp. 491–500, 1997.
- [24] T. Kajita, “Atmospheric neutrinos,” *Advances in High Energy Physics*, vol. 2012, 2012.
- [25] E. Akhmedov, “Quantum mechanics aspects and subtleties of neutrino oscillations,” *arXiv preprint arXiv:1901.05232*, 2019.
- [26] Y. Fukuda, T. Hayakawa, E. Ichihara, K. Inoue, K. Ishihara, H. Ishino, Y. Itow, T. Kajita, J. Kameda, S. Kasuga, *et al.*, “Evidence for oscillation of atmospheric neutrinos,” *Physical Review Letters*, vol. 81, no. 8, p. 1562, 1998.
- [27] M. Tanabashi, K. Hagiwara, K. Hikasa, K. Nakamura, Y. Sumino, F. Takahashi, J. Tanaka, K. Agashe, G. Aielli, C. Amsler, *et al.*, “Review of particle physics,” *Physical Review D*, vol. 98, no. 3, p. 030001, 2018.
- [28] wikipedia, *CP violation*, 2020 (accessed Mar 15, 2020). <https://en.wikipedia.org/wiki/CPViolation>.
- [29] I. J. Aitchison and A. J. Hey, *Gauge theories in particle physics: A practical introduction, Volume 2: Non-Abelian Gauge theories: QCD and the electroweak theory*, vol. 2. CRC Press, 2012.
- [30] S. Abe, T. Ebihara, S. Enomoto, K. Furuno, Y. Gando, K. Ichimura, H. Ikeda, K. Inoue, Y. Kibe, Y. Kishimoto, *et al.*, “Precision measurement of neutrino oscillation parameters with kamland,” *Physical Review Letters*, vol. 100, no. 22, p. 221803, 2008.

- [31] K. Abe, C. Bronner, Y. Haga, Y. Hayato, M. Ikeda, K. Iyogi, J. Kameda, Y. Kato, Y. Kishimoto, L. Marti, *et al.*, “Atmospheric neutrino oscillation analysis with external constraints in super-kamiokande i-iv,” *Physical Review D*, vol. 97, no. 7, p. 072001, 2018.
- [32] F. P. An, A. Balantekin, H. Band, M. Bishai, S. Blyth, D. Cao, G. Cao, J. Cao, W. Cen, Y. Chan, *et al.*, “Measurement of electron antineutrino oscillation based on 1230 days of operation of the daya bay experiment,” *Physical Review D*, vol. 95, no. 7, p. 072006, 2017.
- [33] X. Qian and J.-C. Peng, “Physics with reactor neutrinos,” *Reports on Progress in Physics*, vol. 82, no. 3, p. 036201, 2019.
- [34] K. Abe, J. Amey, C. Andreopoulos, M. Antonova, S. Aoki, A. Ariga, Y. Ashida, S. Ban, M. Barbi, G. Barker, *et al.*, “Measurement of neutrino and antineutrino oscillations by the t2k experiment including a new additional sample of  $\nu e$  interactions at the far detector,” *Physical Review D*, vol. 96, no. 9, p. 092006, 2017.
- [35] K. Abe, R. Akutsu, A. Ali, C. Alt, C. Andreopoulos, L. Anthony, M. Antonova, S. Aoki, A. Ariga, Y. Asada, *et al.*, “Constraint on the matter-antimatter symmetry-violating phase in neutrinooscillations,” *arXiv preprint arXiv:1910.03887*, 2019.
- [36] K. Kimura, A. Takamura, and H. Yokomakura, “Exact formula of probability and cp violation for neutrino oscillations in matter,” *Physics Letters B*, vol. 537, no. 1-2, pp. 86–94, 2002.
- [37] A. Y. Smirnov, “Solar neutrinos: Oscillations or no-oscillations?,” *arXiv preprint arXiv:1609.02386*, 2016.
- [38] A. Y. Smirnov, “The msw effect and matter effects in neutrino oscillations,” *Physica Scripta*, vol. 2005, no. T121, p. 57, 2005.
- [39] Z. Xing and S. Zhou, *Neutrinos in particle physics, astronomy and cosmology*. Springer Science & Business Media, 2011.

- [40] M. Fukugita and T. Yanagida, *Physics of Neutrinos: and Application to Astrophysics*. Springer Science & Business Media, 2013.
- [41] A. Giaz, “Status and perspectives of the JUNO experiment,” *arXiv preprint arXiv:1804.03575*, 2018.
- [42] K. Zuber, *Neutrino physics*. CRC press, 2011.
- [43] M. J. Dolinski, A. W. Poon, and W. Rodejohann, “Neutrinoless double-beta decay: status and prospects,” *Annual Review of Nuclear and Particle Science*, vol. 69, pp. 219–251, 2019.
- [44] O. Cremonesi and M. Pavan, “Challenges in double beta decay,” *Advances in High Energy Physics*, vol. 2014, 2014.
- [45] I. Shimizu and M. Chen, “Double beta decay experiments with loaded liquid scintillator,” *Frontiers in Physics*, vol. 7, p. 33, 2019.
- [46] M. Agostini, M. Allardt, A. Bakalyarov, M. Balata, I. Barabanov, L. Baudis, C. Bauer, N. Becerici-Schmidt, E. Bellotti, S. Belogurov, *et al.*, “Search of neutrinoless double beta decay with the gerda experiment,” *Nuclear and particle physics proceedings*, vol. 273, pp. 1876–1882, 2016.
- [47] M. Agostini, A. Bakalyarov, M. Balata, I. Barabanov, L. Baudis, C. Bauer, E. Bellotti, S. Belogurov, A. Bettini, L. Bezrukov, *et al.*, “Probing majorana neutrinos with double- $\beta$  decay,” *Science*, vol. 365, no. 6460, pp. 1445–1448, 2019.
- [48] J. Albert, G. Anton, I. Arnquist, I. Badhrees, P. Barbeau, D. Beck, V. Belov, F. Bourque, J. Brodsky, E. Brown, *et al.*, “Sensitivity and discovery potential of the proposed nexo experiment to neutrinoless double- $\beta$  decay,” *Physical Review C*, vol. 97, no. 6, p. 065503, 2018.
- [49] C. Alduino, F. Alessandria, K. Alfonso, E. Andreotti, C. Arnaboldi, F. Avignone III, O. Azzolini, M. Balata, I. Bandac, T. Banks, *et al.*, “First results from cuore: A

- search for lepton number violation via  $0\nu\beta\beta$  decay of te-130,” *Physical review letters*, vol. 120, no. 13, p. 132501, 2018.
- [50] G. Piperno, “Dark matter search with the cuore-0 experiment,” 2015.
- [51] “Muons.” [https://cosmic.lbl.gov/SKliewer/Cosmic\\_Rays/Muons.htm](https://cosmic.lbl.gov/SKliewer/Cosmic_Rays/Muons.htm), 2001. [Online; accessed 19-July-2019].
- [52] J. F. Beacom, S. Chen, J. Cheng, S. N. Dousttimotagh, Y. Gao, G. Gong, H. Gong, L. Guo, R. Han, H.-J. He, *et al.*, “Physics prospects of the jinping neutrino experiment,” *Chinese physics C*, vol. 41, no. 2, p. 023002, 2017.
- [53] S. Andringa, E. Arushanova, S. Asahi, M. Askins, D. Auty, A. Back, Z. Barnard, N. Barros, E. Beier, A. Bialek, *et al.*, “Current status and future prospects of the sno+,” *Advances in High Energy Physics*, vol. 2016, 2016.
- [54] M. Anderson, S. Andringa, E. Arushanova, S. Asahi, M. Askins, D. Auty, A. Back, Z. Barnard, N. Barros, D. Bartlett, *et al.*, “Search for invisible modes of nucleon decay in water with the SNO+ detector,” *Physical Review D*, vol. 99, no. 3, p. 032008, 2019.
- [55] J. Paton, “Neutrinoless Double Beta Decay in the SNO+ Experiment,” in *Prospects in Neutrino Physics (NuPhys2018) London, United Kingdom, December 19-21, 2018*, 2019.
- [56] J. D. Jackson, *Classical Electrodynamics*. John Wiley & Sons, 2007.
- [57] L. D. Landau, J. Bell, M. Kearsley, L. Pitaevskii, E. Lifshitz, and J. Sykes, *Electrodynamics of Continuous Media*, vol. 8. elsevier, 2013.
- [58] H. W. C. Tseung and N. Tolich, “Ellipsometric measurements of the refractive indices of linear alkylbenzene and ej-301 scintillators from 210 to 1000 nm,” *Physica Scripta*, vol. 84, no. 3, p. 035701, 2011.
- [59] W. R. Leo, *Techniques for Nuclear and Particle Physics Experiments: a How-to Approach*. Springer Science & Business Media, 2012.

- [60] B. Von Krosigk, *Measurement of Proton and  $\alpha$  Particle Quenching in LAB Based Scintillators and Determination of Spectral Sensitivities to Supernova Neutrinos in the SNO+ Detector*. PhD thesis, 2015.
- [61] A. Sørensen, *Temperature quenching in LAB based liquid scintillator and muon-induced backgrounds in the SNO+ experiment*. PhD thesis, 2016.
- [62] J. Dunger, *Topological and time based event classification for neutrinoless double beta decay in liquid scintillator*. PhD thesis, University of Oxford, 2018.
- [63] D. A. McQuarrie and J. D. Simon, *Physical chemistry: a molecular approach*, vol. 1. University science books Sausalito, CA, 1997.
- [64] S. Collaboration, “Development and characterisation of a linear alkylbenzene-based scintillator for the SNO+ experiment (draft),” *Not submitted yet*.
- [65] J. B. Birks, “Scintillations from organic crystals: specific fluorescence and relative response to different radiations,” *Proceedings of the Physical Society. Section A*, vol. 64, no. 10, p. 874, 1951.
- [66] S. W. Wunderly and J. M. Kauffman, “New quench-resistant fluors for liquid scintillation counting,” *International Journal of Radiation Applications and Instrumentation. Part A. Applied Radiation and Isotopes*, vol. 41, no. 9, pp. 809–815, 1990.
- [67] T. Kaptanoglu, “Measurements of light yield and timing of 0.5 g/l lab+ppo,” *SNO+ Internal Document, docDB-5997-v1*.
- [68] J.-S. Wang, “Bipo analysis using partial fill data,” *SNO+ Internal Document, docDB-5950-v3*.
- [69] J. Boger, R. Hahn, J. Rowley, A. Carter, B. Hollebone, D. Kessler, I. Blevis, F. Dalnoki-Veress, A. DeKok, J. Farine, *et al.*, “The sudbury neutrino observatory,” *Nuclear Instruments and Methods in Physics Research Section A: Accelerators, Spectrometers, Detectors and Associated Equipment*, vol. 449, no. 1-2, pp. 172–207, 2000.

- [70] K. Hamamatsu Photonics, “Photomultiplier tubes: Basics and applications, 2007,” 2018.
- [71] G. O. Gann, “Dealing with time in rat,” *SNO+ Internal Document, docDB-480-v1*.
- [72] R. Bonventre, *Neutron multiplicity in atmospheric neutrino events at the Sudbury Neutrino Observatory*. PhD thesis, 2014.
- [73] A. M. Richie Bonventre, “Everything a detector operator ever wanted to know about electronics and much more you didnt want to know,” *SNO+ Internal Document, docDB-1316-v1*.
- [74] *RAT Overview*, 2020 (accessed Mar 15, 2020). <https://rat.readthedocs.io/en/latest/overview.html>.
- [75] “Overview - rat 1.0 documentation.” <https://rat.readthedocs.io/en/latest/overview.html#goals>, 2014. [Online; accessed 20-Dec-2019].
- [76] A. Hallin, “Fitting partial fill data from december 2014,” *SNO+ Internal Document, docDB-2888-v3*.
- [77] D. Auty and A. Hallin, “Partial water fitter,” *SNO+ Internal Document, docDB-2965-v2*.
- [78] K. Singh, “Wavelength shifter: Carbostyryl 124,” *SNO+ Internal Document, docDB-3351-v2*.
- [79] K. Singh, “Wavelength shifter in water phase of sno+,” *SNO+ Internal Document, docDB-3869-v2*.
- [80] K. Singh, “Multipath fitter processor,” *SNO+ Internal Document, docDB-3849-v1*.
- [81] J. Hu and J. Tseng, “Updates on the multipath water fitter 2018,” *SNO+ Internal Document, docDB-4936-v2*.

- [82] P. Gregory, *Bayesian Logical Data Analysis for the Physical Sciences: A Comparative Approach with Mathematica® Support*. Cambridge University Press, 2005.
- [83] F. Barao and J. Maneira, “Group velocity measurement, plot for approval,” *SNO+ Internal Document, docDB-5071-v1*.
- [84] I. T. Coulter, *Modelling and Reconstruction of Events in SNO+ related to Future Searches for Lepton and Baryon Number Violation*. PhD thesis, Ph. D. thesis, University of Oxford, 2013.
- [85] wikipedia, *JSON*, 2020 (accessed Mar 15, 2020). <https://en.wikipedia.org/wiki/JSON>.
- [86] ROOT, *TDecompQRH Class Reference*, 2020 (accessed Mar 15, 2020). <https://root.cern.ch/doc/master/classTDecompQRH.html>.
- [87] W. P. Group, “Water physics unidoc,” *SNO+ Internal Document*.
- [88] X. Dai, E. Rollin, A. Bellerive, C. Hargrove, D. Sinclair, C. Mifflin, and F. Zhang, “Wavelength shifters for water cherenkov detectors,” *Nuclear Instruments and Methods in Physics Research Section A: Accelerators, Spectrometers, Detectors and Associated Equipment*, vol. 589, no. 2, pp. 290–295, 2008.
- [89] J. Alonso, N. Barros, M. Bergevin, A. Bernstein, L. Bignell, E. Blucher, F. Calaprice, J. Conrad, F. Descamps, M. Diwan, *et al.*, “Advanced scintillator detector concept (asdc): a concept paper on the physics potential of water-based liquid scintillator,” *arXiv preprint arXiv:1409.5864*, 2014.
- [90] M. Askins, M. Bergevin, A. Bernstein, S. Dazeley, S. Dye, T. Handler, A. Hatzikoutelis, D. Hellfeld, P. Jaffke, Y. Kamyshkov, *et al.*, “The physics and nuclear non-proliferation goals of watchman: A water cherenkov monitor for antineutrinos,” *arXiv preprint arXiv:1502.01132*, 2015.

- [91] P. Mekarski, *Electron Antineutrinos in the Water Phase of the SNO+ Experiment.* PhD thesis, 2018.
- [92] S. D. Biller, E. J. Leming, and J. L. Paton, “Slow fluors for highly effective separation of cherenkov light in liquid scintillators,” *arXiv preprint arXiv:2001.10825*, 2020.
- [93] A. LaTorre, “New measurements for the timing spectrum of electrons and alphas in lab+ppo,” *SNO+ Internal Document, docDB-4081-v1*.
- [94] M. G. Boulay, “Direct evidence for weak flavour mixing with the sudbury neutrino observatory.,” 2004.
- [95] B. A. Moffat, *The optical calibration of the Sudbury Neutrino Observatory.* PhD thesis, Ph. D. thesis, Queens University, 2001.
- [96] M. Mottram, “Note on RSP fitter,” *SNO+ Internal Document, docDB-3939-v1*.
- [97] M. Mottram, “Energy reconstruction in partial scintillator fill,” *SNO+ Internal Document, docDB-3133-v1*.
- [98] M. Anderson, “Neural network fitter updates,” *SNO+ Internal Document, docDB-6298-v1*.
- [99] L. Lebanowski, “Improved mode cut,” *SNO+ Internal Document, docDB-5488-v1*.
- [100] J. Klein, “Leta high level cuts (including qpdt and itr),” *SNO+ Internal Document, docDB-2512-v1*.
- [101] M. R. Dragowsky, *Sudbury Neutrino Observatory energy calibration using gamma-ray sources.* PhD thesis, 1999.
- [102] A. S. Hamer, *Energy calibration of SNO for measurement of the charged-current neutrino reaction.* PhD thesis, 2001.
- [103] National Nuclear Data Center, 2019 (accessed Oct 30, 2019). <https://www.nndc.bnl.gov/>.

- [104] M. C. Helen O'Keeffe, Valentina Lozza, "Lab backgrounds expected numbers," *SNO+ Internal Document, docDB-507-v42*.
- [105] E. Davies, "Machine vision: Theory, algorithms, practicalities. academic press., 2-nd edition," 1997.
- [106] wikipedia, *Hough Transform*, 2019 (accessed Nov 3, 2019). [https://en.wikipedia.org/wiki/Hough\\_transform](https://en.wikipedia.org/wiki/Hough_transform).
- [107] M. Shiozawa, "Reconstruction algorithms in the super-kamiokande large water cherenkov detector," *Nuclear Instruments and Methods in Physics Research Section A: Accelerators, Spectrometers, Detectors and Associated Equipment*, vol. 433, no. 1-2, pp. 240–246, 1999.
- [108] G. Beier, "Study of direction reconstruction in scintillator," *SNO+ Internal Document, docDB-3503-v4*.
- [109] S. Biller, S. Manecki, S. collaboration, *et al.*, "A new technique to load 130te in liquid scintillator for neutrinoless double beta decay experiments," in *Journal of Physics: Conference Series*, vol. 888, p. 012084, IOP Publishing, 2017.
- [110] J. Bramante, B. Broerman, J. Kumar, R. F. Lang, M. Pospelov, and N. Raj, "Foraging for dark matter in large volume liquid scintillator neutrino detectors with multiscatter events," *Physical Review D*, vol. 99, no. 8, p. 083010, 2019.
- [111] H. H. Chen, "Direct approach to resolve the solar-neutrino problem," *Physical Review Letters*, vol. 55, no. 14, p. 1534, 1985.
- [112] Q. R. Ahmad, R. Allen, T. Andersen, J. Anglin, J. Barton, E. Beier, M. Bercovitch, J. Bigu, S. Biller, R. Black, *et al.*, "Direct evidence for neutrino flavor transformation from neutral-current interactions in the sudbury neutrino observatory," *Physical review letters*, vol. 89, no. 1, p. 011301, 2002.

- [113] B. Aharmim, S. Ahmed, A. Anthony, N. Barros, E. Beier, A. Bellerive, B. Beltran, M. Bergevin, S. Biller, K. Boudjemline, *et al.*, “Combined analysis of all three phases of solar neutrino data from the sudbury neutrino observatory,” *Physical Review C*, vol. 88, no. 2, p. 025501, 2013.
- [114] H. W. Zaglauer and K. H. Schwarzer, “The mixing angles in matter for three generations of neutrinos and the msw mechanism,” *Zeitschrift für Physik C Particles and Fields*, vol. 40, no. 2, pp. 273–282, 1988.
- [115] P. B. Denton, S. J. Parke, and X. Zhang, “Eigenvalues: The rosetta stone for neutrino oscillations in matter,” *arXiv preprint arXiv:1907.02534*, 2019.
- [116] M. Agostini, M. Allardt, A. Bakalyarov, M. Balata, I. Barabanov, L. Baudis, C. Bauer, E. Bellotti, S. Belogurov, S. Belyaev, *et al.*, “Background-free search for neutrinoless double- $\beta$  decay of  $^{76}\text{Ge}$  with gerda,” *Nature*, vol. 544, no. 7648, pp. 47–52, 2017.
- [117] M. Agostini, A. Bakalyarov, M. Balata, I. Barabanov, L. Baudis, C. Bauer, E. Bellotti, S. Belogurov, A. Bettini, L. Bezrukov, *et al.*, “Improved limit on neutrinoless double- $\beta$  decay of  $^{76}\text{Ge}$  from gerda phase ii,” *Physical review letters*, vol. 120, no. 13, p. 132503, 2018.
- [118] I. Esteban, M. Gonzalez-Garcia, A. Hernandez-Cabezudo, M. Maltoni, and T. Schwetz, “Global analysis of three-flavour neutrino oscillations: synergies and tensions in the determination of  $\theta_{23}$ ,  $\delta_{CP}$ , and the mass ordering,” *Journal of High Energy Physics*, vol. 2019, no. 1, p. 106, 2019.
- [119] K. Zuber, “On the physics of massive neutrinos,” *Physics Reports*, vol. 305, no. 6, pp. 295–364, 1998.
- [120] C. Weinheimer, “Neutrino mass from triton decay,” *Progress in Particle and Nuclear Physics*, vol. 57, no. 1, pp. 22–37, 2006.

- [121] Y. Xing-Chen, Y. Bo-Xiang, Z. Xiang, Z. Li, D. Ya-Yun, L. Meng-Chao, D. Xue-Feng, Z. Xuan, J. Quan-Lin, Z. Li, *et al.*, “Preliminary study of light yield dependence on lab liquid scintillator composition,” *Chinese Physics C*, vol. 39, no. 9, p. 096003, 2015.
- [122] T. Kaptanoglu, “Characterization of the hamamatsu 8 r5912-mod photomultiplier tube,” *Nuclear Instruments and Methods in Physics Research Section A: Accelerators, Spectrometers, Detectors and Associated Equipment*, vol. 889, pp. 69–77, 2018.
- [123] Y. Zhang, “Performance of qenergy based on q,” *SNO+ Internal Document, docDB-6065-v1*.
- [124] M. Anderson, S. Andringa, S. Asahi, M. Askins, D. Auty, N. Barros, D. Bartlett, F. Barão, R. Bayes, E. Beier, *et al.*, “Measurement of the  ${}^8\text{B}$  solar neutrino flux in SNO+ with very low backgrounds,” *Physical Review D*, vol. 99, no. 1, p. 012012, 2019.
- [125] R. Brun, F. Rademakers, P. Canal, *et al.*, “Root: An object oriented data analysis framework, 2007,” *See Also <http://root.cern.ch>*.
- [126] S. Agostinelli, J. Allison, K. a. Amako, J. Apostolakis, H. Araujo, P. Arce, M. Asai, D. Axen, S. Banerjee, G. . Barrand, *et al.*, “Geant4a simulation toolkit,” *Nuclear instruments and methods in physics research section A: Accelerators, Spectrometers, Detectors and Associated Equipment*, vol. 506, no. 3, pp. 250–303, 2003.
- [127] G. Horton-Smith *et al.*, “Introduction to glg4sim,” 2006.
- [128] M. Dunford, *Measurement of the  ${}^8\text{B}$  solar neutrino energy spectrum at the Sudbury Neutrino Observatory*. PhD thesis, 2006.